

ALMA MATER STUDIORUM · UNIVERSITÀ DI BOLOGNA

Scuola di Scienze
Dipartimento di Fisica e Astronomia
Corso di Laurea Magistrale in Fisica

**Investigation of indium tin oxide-titanium
dioxide interconnection layers for
perovskite-silicon tandem solar cells**

Relatore:
Prof. Daniela Cavalcoli

Presentata da:
Jacopo Gasparetto

Correlatore:
**Dott. Jan Christoph
Goldschmidt**
Dott. Armin Richter
M.Sc. Alexander Bett

Anno Accademico 2016/2017

Abstract

In questo lavoro è stato studiato ed investigato in dettaglio una nuova tipologia di stack di layer per interconnettere una cella solare a perovskite (PSC) e una cella solare eterogiunzione al silicio (SHJ) con lo scopo di realizzare in futuro una cella tandem monolitica a due terminali, ove la PSC veste il ruolo di top-cell mentre la cella SHJ quello di bottom-cell.

Lo stack consiste in un layer di 20 nm di indium tin oxide (ITO), depositato tramite sputtering, e un film sottile di titanium dioxide (TiO_2) depositato tramite differenti tecniche. In una cella SHJ, il layer di ITO costituisce il contatto frontale (top contact) e nel caso di una cella tandem completa svolge la funzione di *recombination layer* per i portatori di carica generati dalla due singole celle. Il layer di TiO_2 è invece il contatto posteriore della PSC e svolge la funzione di *electron transport layer* (ETL), andando a migliorare l'estrazione degli elettroni foto-generati e quindi l'efficienza della stessa.

La presente tesi si focalizza sullo studio di un sandwich ITO/ TiO_2 /ITO, dove il film di TiO_2 è stato depositato tramite Thermal Atomic Layer Deposition (T-ALD), Plasma Enhanced Atomic Layer Deposition (PE-ALD) ed Electron Beam Physical Vapour Deposition (EBPVD). Per ogni tecnica di deposizione, è stata misurata la resistenza di serie dello stack – in particolare la resistività del TiO_2 bulk e la resistenza di contatto all'interfaccia TiO_2 e ITO – in funzione dello spessore del film di TiO_2 . Si è misurata una resistenza di serie superiore a $15 \Omega \text{ cm}^2$ per i campioni con 20 nm di TiO_2 preparato tramite PE-ALD e una resistenza di serie attorno ai $0.2 \Omega \text{ cm}^2$ e $0.4 \Omega \text{ cm}^2$ per campioni con 20 nm di TiO_2 preparati tramite T-ALD e EBPVD. È stato studiato l'effetto di annealing termico sui campioni e si è osservato, in genere, un calo complessivo della resistenza per tutti i campioni processati con le differenti tecniche. In particolare, i campioni processati tramite PE-ALD hanno mostrato un calo significativo della resistenza, fino a valori inferiori a $0.1 \Omega \text{ cm}^2$ quando soggetti ad annealing a temperature di 225°C per un tempo di 15 min.

I film di TiO_2 sono poi stati analizzati tramite X-ray Photoelectron Spectroscopy (XPS) e X-ray Diffraction (XRD) per sondare la composizione chimica-stechiometrica e la struttura cristallina. Per tutti i campioni è risultato un rapporto della concentrazione atomica O:Ti di circa 2.2 con una fase amorfa, indipendentemente dalla tecnica di deposizione del TiO_2 utilizzata. Solamente dopo un annealing a 450°C per 15 min, le fasi

cristalline del TiO_2 rutile e anatase sono state osservate.

Il lavoro si è concluso con un test preliminare su celle perovskite realizzate con 20 nm di TiO_2 , depositato tramite le tre tecniche annunciate, su un layer di ITO di 20 nm di spessore. La cella migliore processata tramite EBPVD ha mostrato un'efficienza pari al 13.4% e 16.8% in scansione diretta e inversa, rispettivamente, mentre la cella migliore processata tramite PE-ALD ha mostrato un'efficienza del 13.7% e 13.4% in scansione diretta e inversa. A causa di problemi durante la deposizione del TiO_2 tramite T-ALD, risultante in una deposizione parziale del film, non si è riusciti a dare una stima accurata delle efficienze delle PSC realizzate tramite questa tecnica.

I valori della resistenza di serie dello stack ITO/ TiO_2 /ITO risultano essere compatibili con la realizzazione di celle tandem perovskite-silicio, in particolare per quanto riguarda i campioni con layer di TiO_2 depositato tramite T-ALD ed EBPVD e campioni con TiO_2 depositato tramite PE-ALD trattati tramite annealing termico a 225 °C per un tempo di 15 min. I valori di efficienze ottenute per le celle solari perovskite realizzate con un layer di TiO_2 depositato tramite T-ALD ed EBPVD su di un layer di ITO risultano essere confrontabili con lo stato dell'arte. Questi risultati comprovano la fattibilità di celle tandem perovskite-silicio monolitiche dove il layer inferiore in TiO_2 della PSC è depositato direttamente sul layer superiore di ITO di una cella al silicio a etero-giunzione.

In this work, a new kind of layer stack to interconnect a perovskite solar cell (PSC) and a silicon heterojunction (SHJ) solar cell has been studied and investigated in detail, with the aim to build a two-terminal monolithic solar tandem cell in the next future, where the PSC is the top-cell and the SHJ is the bottom-cell.

The stack consists in a 20 nm thick indium tin oxide (ITO) layer, deposited via sputtering, and a titanium dioxide (TiO_2) thin film deposited through three different deposition techniques. In a SHJ cell, the ITO layer is the frontal contact and in a monolithic tandem device plays also the role of *recombination layer* for the free charge carriers generated by the two cells. The TiO_2 layer is, instead, the rear contact of the PSC and covers the function of *electron transport layer* (ETL) which improves the extraction of the photo-generated electrons and thus, the efficiency of cell.

The focus of this thesis is the study of the sandwich ITO/ TiO_2 /ITO, where the TiO_2 film has been deposited via Thermal Atomic Layer Deposition (T-ALD), Plasma Enhanced Atomic Layer Deposition (PE-ALD) and Electron Beam Physical Vapour Deposition (EBPVD). For each deposition technique, the series resistance of the stack – in particular the TiO_2 bulk resistivity and the contact resistance at the interface between TiO_2 and ITO – was measured as function of the TiO_2 film thickness. A series resistance above $15 \Omega \text{ cm}^2$ was measured for samples prepared with 20 nm thick PE-ALD TiO_2 and a series resistance around $0.2 \Omega \text{ cm}^2$ and $0.4 \Omega \text{ cm}^2$ was measured for samples with 20 nm thick TiO_2 prepared via T-ALD and EBPVD. The effect of thermal annealing on the samples has been investigated and a general lowering of the resistance of all the samples differently processed was observed. In particular, the samples prepared via PE-ALD, when subjected to temperatures of 225°C for 15 min, showed a significant drop of the resistance down to values below $0.1 \Omega \text{ cm}^2$.

The TiO_2 films have been analysed via X-ray Photoelectron Spectroscopy (XPS) and X-ray Diffraction (XRD) to identify the chemical composition (and stoichiometry) and an eventual crystalline phase. All the samples resulted with an atomic concentration ratio O:Ti of around 2.2 and they were amorphous, independently of the TiO_2 deposition technique. The crystalline phases of TiO_2 , rutile and anatase, were observed only after annealing at 450°C for 15 min.

The work ended with a preliminary test on perovskite cells fabricated with 20 nm thick TiO_2 layer deposited through the three mentioned deposition techniques on a 20 nm thick ITO layer. The best cell processed via EBPVD exhibited a power conversion efficiency (PCE) of 13.4% and 16.8% in forward and reverse scan, respectively, while the best cell processed with PE-ALD exhibited a PCE of 13.7% and 13.4% in forward and reverse scan, respectively. Because of problems occurred during the deposition of the TiO_2 layer through T-ALD, resulted in a partial deposition, an accurate estimation of the efficiency of PSC fabricated with this technique, has been not possible.

The series resistance values measured for the ITO/ TiO_2 /ITO stack, in particular for samples prepared with TiO_2 deposited through T-ALD and EBPVD, resulted to be compatible with the fabrication of perovskite-silicon tandem solar cells. Also samples

prepared with PE-ALD TiO_2 resulted compatible with tandem applications but after a thermal annealing at 225°C for 15 min. The power conversion efficiencies obtained from the perovskite solar cells fabricated with a TiO_2 layer deposited via T-ALD or EBPVD on ITO resulted to be comparable with the state of art. These results confirm the viability of perovskite-silicon solar tandem cell where the bottom TiO_2 layer of the PSC is directly deposited on the top ITO layer of the silicon heterojunction cell.

Acknowledgments

All the experimental work and the writing of this thesis were entirely conducted at Fraunhofer Institute for Solar Energy Systems (ISE) in Freiburg im Breisgau, Germany.

The completion of this work could not have been possible without the assistance of my supervisors Jan Christoph, Alexander and Armin who helped me during the development of this thesis and taught me what *doing science* means.

To all the awesome people of the Novel Team for your support, help and moments spent together, to Karin, for the precious teachings in the lab, thank you. A special thanks to Patricia, for your help with this work but especially for making my stay in Freiburg unforgettable.

Thanks to my classmates and friends from the University, and to my mother, who always encouraged and supported me during my studies.

Jacopo

Contents

1	Introduction	1
1.1	Motivation	1
1.2	Scope of this work	4
1.3	Outline of this work	6
2	Theory	7
2.1	Semiconductor Junction Theory	7
2.1.1	Heterojunction Theory	8
2.1.2	Metal – Semiconductor Junction	11
2.2	Electronic transport in Perovskite-silicon Tandem Solar Cells	13
2.2.1	Perovskite solar cell (PSC)	14
2.2.2	Tandem device	17
2.2.3	Interconnection ITO – TiO ₂ stack	20
3	Experimental Methods	23
3.1	Film preparation	23
3.1.1	Atomic Layer Deposition (ALD)	23
3.1.2	Electron Beam Physical Vapour Deposition (EBPVD)	30
3.2	Sample preparation	31
3.2.1	Dicing methods	34
3.3	Perovskite solar cell preparation	34
3.4	Characterisation	35
3.4.1	Resistance measurements	35
3.4.2	Spectroscopic Ellipsometry	36
3.4.3	X-ray diffraction (XRD)	37
3.4.4	X-ray Photoelectron Spectroscopy (XPS)	38
3.4.5	Dark Lock-In Thermography (DLIT)	39
4	Experimental Results	41
4.1	General Structure Analysis	41
4.1.1	Overview Resistance Investigation	41

4.1.2	Analysis of shunt at the edges	44
4.2	Resistance results	46
4.2.1	Plasma Enhanced ALD	46
4.2.2	Thermal ALD	54
4.2.3	Electron Beam Physical Vapour Deposition	59
4.2.4	General resistance comparison	62
4.3	X-ray Photoelectron Spectroscopy (XPS)	63
4.4	X-ray Diffraction (XRD)	66
4.5	Dark Lock-in Thermography (DLIT)	68
4.6	Perovskite Solar Cells Results	74
5	Conclusion and outlook	79

List of Figures

1.1	(a) sketch of the light absorption mechanism in a traditional silicon solar cell: photons with energy higher than the silicon band gap are collected by the cell producing a electron-hole pair with consequent energy losses due to the thermalisation, while photons with energy lower than the band gap are not absorbed but transmitted; (b) solar spectrum absorbed by a traditional silicon solar cell.	2
1.2	(a) sketch of the light absorption mechanism of the two sub-cells, where the top is a perovskite solar cell and the bottom cell is silicon heterojunction solar cell; (b) solar spectrum absorbed by the two sub-cells.	3
1.3	Effect of series resistance on the $J-V$ characteristic of a solar cell calculated with one-diode model.	4
1.4	Sketch of a typical perovskite-silicon tandem solar cell, with the perovskite cell is the top cell and the silicon cell is the bottom cell. TCO stands for transparent conductive oxide.	5
2.1	$n-p$ heterojunction (a) before and (b) after contact.	8
2.2	Two metal – semiconductor junctions with different doping: n -type and p -type semiconductors. If the semiconductor is n -type (a), the Schottky barrier φ_B hinders electrons coming from the metal towards the semiconductor. If it is p -type (b) the barrier affects holes flowing in the same direction. In both cases a smaller barrier qV_{bi} exists for carriers flowing from the semiconductor to the metal.	11
2.3	Energy bands of some of most common perovskite absorber materials [30, 31]. In blue are shown ETLs, purple perovskite absorbers, in red HTLs.	14
2.4	Schematic band diagram to illustrating the charge production and extraction by ETL and HTL in a Perovskite Solar Cell (picture not in scale).	15
2.5	Examples of perovskite solar cells with (a) regular planar structure, (b) regular structure with mesoporous scaffold and (c) inverted planar structure. TCO refers to <i>Transparent Conductive Oxide</i>	16

2.6	Examples of perovskite solar cells with (a) planar structure with mesoporous TiO ₂ scaffold and (b) planar inverted structure realised at Fraunhofer ISE.	17
2.7	Scheme of a monolithic two-terminal (a) and mechanically stacked four-terminal (b) tandem devices. Shorter wavelength light is absorbed by the top perovskite cell and longer wavelengths by the silicon bottom cell as illustrated.	17
2.8	Electrical equivalent circuit of two solar cells in series with single diode model.	18
2.9	Monolithic two-terminal Perovskite-silicon tandem solar cell under production at Fraunhofer ISE.	20
3.1	A complete ALD cycle: during the first half of cycle (a) and (b) the first precursor, as for instance titanium tetraisopropoxide (TTIP), reacts with the substrate and the reaction stops when the whole surface is covered. In the second half (c) and (d) the oxidiser is pumped into the chamber completing the reaction. When all sites are oxidised the first layer is deposited and another cycle is repeated.	24
3.2	Scheme of a ALD reactor featuring a RF coil for PE-ALD deposition. During a PE-ALD deposition, in the first half of the cycle the precursor is introduced in the chamber. In the second half of cycle, an inductively induced plasma of ionised O ₂ is generated through the RF coil, bombarding the substrate and completing the deposited layer. In a T-ALD deposition, the first half of cycle is substantially the same as for PE-ALD while, in the second half, the oxidiser is introduced as water vapour.	26
3.3	Time evolution of a complete ALD cycle of (a) TiO ₂ T-ALD, (b) TiO ₂ PE-ALD and (c) Al ₂ O ₃ PE-ALD. With different colours are depicted the gases in the chamber. The drawing is not in scale.	27
3.4	Measured thickness of TiO ₂ films deposited on silicon deposited by (a) T-ALD and (b) PE-ALD in function of number of cycles used during the ALD processes. The growth per cycle (GPC) is calculated as the slope of the linear fit.	29
3.5	Schematic sketch of an electron beam evaporation system.	30
3.6	Structures analysed to investigate the resistance of the ITO/TiO ₂ /ITO stack: (a) reference samples without TiO ₂ layer; (b) samples for resistance measurements. ETL represents TiO ₂ deposited with different techniques. For some samples ETL is replaced with insulating Al ₂ O ₃ . (c) samples for DLIT images. The front metal contact is replaced with a metal grid. In this case ETL indicates only TiO ₂	31

3.7	Samples processing from the silicon substrates to the final structure. In red substrate preparation in clean room; in blue ITO/TiO ₂ /ITO stack deposition; in grey metal contact evaporation and dicing. (a) process chain for reference and resistance measurement samples shown in Figure 3.8a and (b) process chain of samples with metal grid for DLIT probe (Figure 3.8b).	32
3.8	Top view of the prepared 4-inch wafers: (a) 2 × 2 cm ² metal pads evaporated with shadow-mask for resistance measurements and (b) 2 × 2 cm ² metal grids for DLIT probes. The colour blue represents the top ITO layer. The dashed lines indicate the cutting lines.	33
3.9	Sketch of four-point probe resistance measurements setup and electrical connections for (a) regular pad samples and (b) samples with grid metal contact for DLIT. The blue and grey colours represent the metal-coated samples. The back vacuum chuck and the connection needles are coloured in yellow.	35
3.10	Sketch of the interference phenomenon for ellipsometry thickness measurement. The polarised light is reflected at the angle θ_0 at the surface, n_0 is the refractive index of the air, n_1 the refractive index of the film to analyse and n_2 is the refractive index of the substrate.	36
4.1	Sketch of the different types of sample dicing techniques used: (a) partial engraving by laser or dicing saw from the top metal-pad contact evaporated with a shadow-mask; (b) complete laser cut through the wafer from the top full-metal contact; (c) partial engraving with dicing saw from the bottom, with top full-area metal contact.	42
4.2	Resistance measurements results after different dicing methods of differently processed samples: TiO ₂ deposited via EBPVD and PE-ALD, Al ₂ O ₃ deposited via PE-ALD and reference samples without ETL. Two groups of samples with Al ₂ O ₃ were fabricated with a front full-area metal contact, all the others samples were fabricated with front metal-pad contacts evaporated using a shadow-mask.	43
4.3	DLIT investigation of three samples with different TiO ₂ films prepared with a top grid-metal contact as shown in Figure 3.6c. The voltage biases were chosen to generate roughly the same total current. For similar total current flowing through the sample, brighter areas indicate a higher local current flow due to low resistive paths.	44
4.4	Resistance results of samples provided with top grid-metal contact used for the DLIT investigation showed in Figure 4.24 and samples provided with top pad-metal contact. These samples were used as references for samples with metal-grid.	45

4.5	Electrical scheme of the series resistance R_{series} due to the TiO_2 film and the interfaces with ITO and the shunt resistance R_{shunt} due to the dicing connected in parallel.	45
4.6	Current–Voltage characteristic of samples with 20 nm thick TiO_2 film recorded with different voltage scans: (a) $0\text{ V} - 0.7\text{ V}$ (forward) and $0\text{ V} - -0.7\text{ V}$ (reverse) scans used to calculate the total series resistance; (b) scan from $-0.5\text{ V} - 0.5\text{ V}$ and from $0.5\text{ V} - -0.5\text{ V}$; (c) scan from $0\text{ V} - 2\text{ V}$, from $2\text{ V} - -2\text{ V}$ and from $-2\text{ V} - 0\text{ V}$; (d) scan from $-2\text{ V} - 2\text{ V}$ and $2\text{ V} - -2\text{ V}$. 47	47
4.7	Resistance results of samples with different TiO_2 thicknesses processed with PE–ALD calculated fitting the J – V curves recorded in forward (0 V to $+V$) and reverse (0 V to $-V$) directions. The voltage bias was adjusted for each samples to limit the current below 40 mA/cm^2 . For more accurate thickness values refer to Table 3.2.	48
4.8	Resistance of samples prepared with PE–ALD processed TiO_2 films vs the film thickness listed in Table 3.2. In red is indicated the linear fit used to calculate the resistivity of the TiO_2 and the contact resistance with ITO. 49	49
4.9	Thermal effect on the resistance of samples with TiO_2 films prepared by PE–ALD as function of temperature and annealing time. Two distinct groups were analysed: one set of samples with (a) the highest resistance values and one with (b) the lowest resistance values. The red is indicate the resistance of a reference samples without TiO_2 film.	50
4.10	Detailed thermal treatment investigation for several different nominal thicknesses of TiO_2 film deposited by PE–ALD: (a) 20 nm; (b) 15 nm; (c): 10 nm; (d) 5 nm; (e) 2 nm; (f) reference samples without TiO_2 . Two samples were used for each thickness and as reference.	52
4.11	Effect of the thermal treatment on the linearity of the resistance as function of the TiO_2 film thickness for (a) high resistive samples and (b) low resistive samples. The displayed data are the same values shown in Figure 4.9. 53	53
4.12	Resistance of samples with different TiO_2 thicknesses, grown via T–ALD. 54	54
4.13	Example of J – V characteristic of 20 nm thick TiO_2 film. The arrows indicate the direction of the voltage scans.	55
4.14	Thermal treatment effect on samples with different TiO_2 thicknesses films deposited with T–ALD: (a) 20 nm; (b) 15 nm; (c) 10 nm; (d) 5 nm; (e) 2 nm; (f) reference samples without TiO_2	57
4.15	(a) detailed analysis of the thermal treatment on 20 nm thick TiO_2 films deposited with T–ALD; (b) reference samples without TiO_2 film.	58

4.16	Resistance of samples with different TiO ₂ films thicknesses grown by EBPVD in two different batches. In the first batch only samples with 20 nm thick TiO ₂ film were prepared. The two batches showed completely different results without clear reason. Furthermore, three exemplary samples with 20 nm thick TiO ₂ film were annealed at 225 °C for 15 min showing a drastic reduction of the resistance.	59
4.17	J - V characteristics of two samples with 20 nm thick TiO ₂ films deposited with EBPVD in two distinct batches. The arrows indicate the direction of the voltage scans.	60
4.18	J - V hysteresis observed on samples with 20 nm thick TiO ₂ prepared in the batch n.4; The numbers and the arrows represent the order and the directions of the scans: $0V \rightarrow +V \rightarrow -V \rightarrow +V \rightarrow -V \rightarrow 0V$	60
4.19	Thermal treatment effect on the resistance of samples with 20 nm thick TiO ₂ films grown with EBPVD: (a) general overview of thermal effect on two samples; (b) reference samples without TiO ₂ ; (c) detailed investigation of the thermal effect on samples with fixed temperature and cumulative annealing time.	62
4.20	Resistance values of the samples with 20 nm thick TiO ₂ films deposited with electron beam physical vapour deposition (EBPVD), plasma enhanced ALD (PE-ALD) and thermal ALD (T-ALD). For each technique, samples were realised in two separate batches.	63
4.21	XPS investigation of 20 nm thick TiO ₂ film grown on ITO with PE-ALD: (a) and (b) overview and detailed spectra as-deposited; (c) and (d) overview and detailed spectra annealed in air; (e) and (f) overview and detailed spectra annealed in the glovebox (nitrogen). The overview scans were performed before (black) and after argon sputtering (red). The atomic concentrations were obtained from the detailed scans around the Ti _{2p} and O _{1s} peaks.	65
4.22	XPS investigation of 20 nm thick TiO ₂ film grown on ITO with EBPVD and T-ALD. (a) and (b) overview and detailed spectra of TiO ₂ grown with EBPVD respectively; (c) and (d) overview and detailed spectra of TiO ₂ grown with T-ALD, respectively. The overview scans were performed before (black) and after argon sputtering (red). The atomic concentrations were obtained from the detailed scans around the Ti _{2p} and O _{1s} peaks. . .	66

4.23 XRD spectra of: (a) 20 nm thick TiO ₂ films deposited on ITO through the three different deposition techniques used. Samples in light blue and grey have been prepared in a separate batch and they have an area of 2 × 2 cm ² , while the other samples consist of half 4-inch wafers; (b) TiO ₂ film prepared with PE-ALD after one annealing step at 225 °C for 15 min (green) and the same sample after an additional step at 450 °C for 15 min more (orange). Anatase and rutile TiO ₂ crystalline phases appeared after this second step as well as peaks coming from the ITO layer underneath. In blue, the XRD spectrum of pure ITO without TiO ₂ is shown. All the spectra are normalised.	67
4.24 DLIT images of TiO ₂ films grown by: (a), (b), (c) EBPVD 20 nm; (d), (e), (f) T-ALD 20 nm; (g), (h), (i) PE-ALD 2 nm; (j), (k), (l) PE-ALD 20 nm. Three identically processed samples are shown per each TiO ₂ deposition technique. The pictures have been rescaled as function of the input power of the samples.	71
4.25 Resistance measurements of samples with top metal-grid contact used for the DLIT investigation shown Figure 4.24.	72
4.26 Resistance measurements of samples with top metal-pad contact used as reference for the samples prepared with top metal-grid shown Figure 4.24 and Figure 4.25.	73
4.27 Perovskite solar cells (PSCs) with 20 nm thick TiO ₂ films acting as electron transport layer deposited on ITO through (b) EPBVD, (c) T-ALD and (d) PE-ALD. Two ITO layers were coated with different oxygen flow: 0.3 sccm to improve the lateral conductivity and 0.7 sccm for having the same contact before and like in a tandem cell. PSCs prepared with 20 nm thick TiO ₂ on FTO ((a)) were used as reference cells.	74
4.28 Comparison of perovskite solar cells with TiO ₂ films deposited on ITO trough EBPVD, T-ALD and PE-ALD. Some process problems occurred during the T-ALD deposition causing a wrong layer thickness. Cells with TiO ₂ deposited with EBPVD on FTO were used as reference.	75
4.29 (a) current-voltage characteristics of perovskite solar cells prepared with TiO ₂ film processed differently and (b) a zoom detail of the same characteristics around the open-circuit voltage points. The slopes represent the overall series resistance of the cells.	76
4.30 Series resistance of the analysed PSCs obtained from two-diodes model fits to the <i>IV</i> curves under illumination.	77

Chapter 1

Introduction

1.1 Motivation

In the last few decades, the climate change has become more and more a global tangible issue, especially regarding the energy production, which is still mainly based on fossil fuels. This did open a new challenge to produce energy coming from renewable and environmental friendly sources. Among these, clearly, photovoltaic energy covers a large portion thanks to its relative simplicity in modules installation and accessibility of the source, the sun. At present, most of photovoltaic modules are based on silicon cell technology due to its affordability and well consolidated knowledge, although the theoretical efficiency limit of a crystalline silicon solar cell is calculated to be 30% [1] due to radiative recombination losses. Taking into account also Auger recombination, this limit decreases to 29.43% for un-doped silicon cells [2]. At the time of writing, the efficiency record for a fully optimised silicon solar cell is 26.7% [3, 4].

The solar energy research community is moving more and more towards new photovoltaic technology concepts to overcome the efficiency limit of classic silicon cells, for example using different light absorber materials and complex structures such as tandem devices. In this kind of devices, two or more distinct solar cells work together to absorb a wider range of the solar spectrum or to reduce thermal losses of a silicon cell, with the aim to cross the efficiency limit of a single cell. In fact, a very limiting factor for traditional silicon solar cells is due to thermalisation losses that occur absorbing photons with energy higher than the silicon band gap (Figure 1.1).

Since the first appearance in late first decade of 2000s, Perovskite solar cells (PSCs) gained a lot of attention because of their extremely fast improvement in terms of efficiency [5], with efficiencies up to 22% [6], and potentially low production cost [5]. The wide and tunable band gap of PCEs is very suitable to absorb high energy photons, while the transmitted photons in the near infrared range can be absorbed by a traditional silicon cell or silicon heterojunction solar cell (SHJ). This makes them a very promising

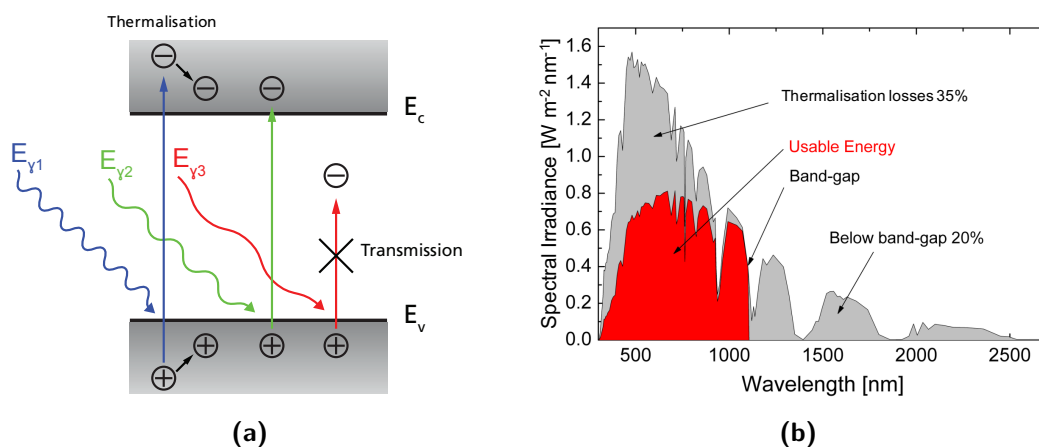


Figure 1.1: (a) sketch of the light absorption mechanism in a traditional silicon solar cell: photons with energy higher than the silicon band gap are collected by the cell producing an electron-hole pair with consequent energy losses due to the thermalisation, while photons with energy lower than the band gap are not absorbed but transmitted; (b) solar spectrum absorbed by a traditional silicon solar cell.

candidate as top cell in a tandem device. In a perovskite-silicon tandem solar cell, high energetic photons are absorbed by the top perovskite solar cell, leading to more efficient photon harvesting and thus, improving the general efficiency of the solar cell, as shown in Figure 1.2.

It is possible to identify three main architectures for PSC tandem devices: separated tandem cells connected in series, monolithic two terminal cells and mechanically stacked four terminal cells [7]. Nevertheless, the monolithic two-terminal structure is probably the most investigated one because it can be fabricated as sequential depositions of all films required to realise the complete device and, most importantly, its integration in solar modules is considered much simpler.

In addition to a high quality absorber film, also the interfaces of the device play a critical role in the charge collection and then in overall performance. When a photon is absorbed by the perovskite absorber, an electron-hole pair is produced and it needs to be extracted. Similarly to a traditional $p-n$ solar cell, where the two doped regions force the free carriers to move towards the external contact, a PSC needs a Hole Transport Layer (HTL) and an Electron Transport Layer (ETL) which role is to collect free carriers outside the absorber, creating indeed a $p-i-n$ solar cell. In this way, the research of materials suitable to act as HTL and ETL for PSCs is of primary importance. Common HTLs are organic poly(3,4-ethylenedioxythiophene) polystyrene sulfonate (PEDOT:PSS) and 2,2',7,7'-Tetrakis[N,N-di(4-methoxyphenyl)amino]-9,9'-spirobifluorene (spiro-MeOTAD) [8–10] or metal-oxides such as nickel oxide (NiO_x) [11]. Widely used ETL materials are tin dioxide (SnO_2) [12], Zinc Oxide (ZnO) [13] and especially titanium dioxide (TiO_2) [14–16]. Moreover, several studies have shown that a mesoporous TiO_2 layer can increase the

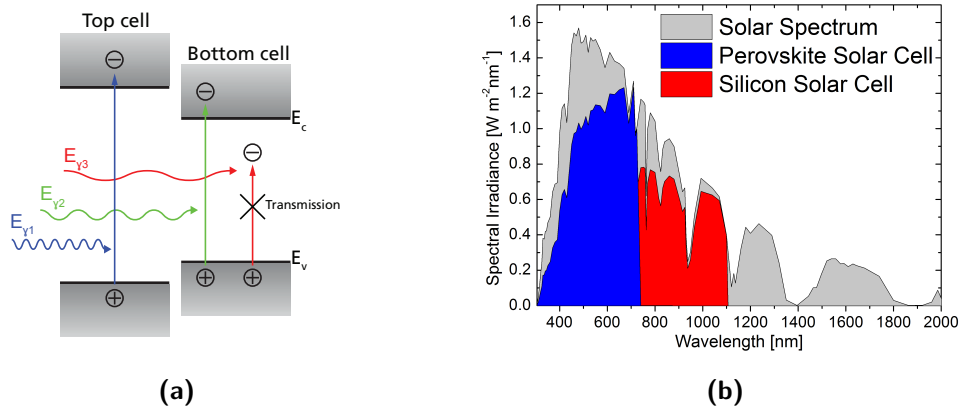


Figure 1.2: (a) sketch of the light absorption mechanism of the two sub-cells, where the top is a perovskite solar cell and the bottom cell is silicon heterojunction solar cell; (b) solar spectrum absorbed by the two sub-cells.

electron collection efficiency and thus improves the external quantum efficiency (EQE) [6, 17]. However, having good interfaces for charge collection and transport is not the only requirement in a monolithic stacked tandem device. Also the series connection of the two sub-cells requires an interface layer between the carrier transport materials (ETL or HTL) of the PSC and the opposite equivalent (p or n) side of the silicon cell. When the p region of the first sub-cell is joined to the n region of the second sub-cells, a p - n junction is formed. At this junction, the free holes coming from the p -side of the first sub-cell recombine with the electrons coming from the n -side of the second cell, creating a space charge region at the interface. Thus, the space charge region acts as a charge emitter for both the two sub-cell, providing free electrons and holes to the first and the second sub-cell, respectively. Two routes are possible to recombine the charges at the interface of the two sub-cells: heavy doping of the two contacting layers creating a n^{++}/p^{++} tunnel junction or interposing a transparent contact that acts as recombination layer between electrons and holes coming from the two sub-cells and working as an ohmic contact with very low series resistance. To achieve a highly efficient tandem solar cell, is then required to optimally tune the interconnection between the transport material (in this study the ETL) of the PSC and the top layer of the SHJ cell keeping the resistance of this interface as low as possible. In Figure 1.3 the effect of the series resistance in a solar cell is plotted. Starting with the ideal case of $R_s = 0$ and increasing its value it is clear how the performance degrades rapidly. In a tandem device, the resistance of the interconnection layer(s) adds to the two intrinsic series resistance of the sub-cells. It is therefore extremely important to find the best combination of layers to maximise their charge transport capabilities and reducing, at the same time, losses due to high bulk and interface resistance.

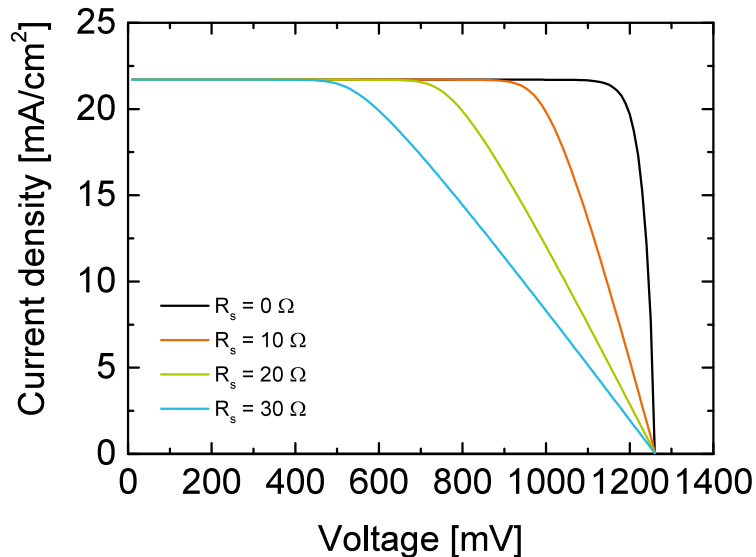


Figure 1.3: Effect of series resistance on the J - V characteristic of a solar cell calculated with one-diode model.

1.2 Scope of this work

The scope of this work is to study the interconnection layer of monolithic perovskite-silicon tandem solar cells, with the PSC on top and a silicon heterojunction solar cell (SHJ) as bottom cell. Typically, in SHJ the top layer is made of indium tin oxide (ITO) [18] on top of which the PSC is directly placed, creating a contact between ITO and the ETL.

Since it has been shown that PSCs exhibit higher efficiency when deposited on a mesoporous TiO_2 scaffold grown on compact TiO_2 [6, 15], in this work several TiO_2 thin film deposition techniques on ITO are investigated and compared with the aim to optimise the interface ETL-recombination layer with low series resistance in a monolithic perovskite-silicon tandem solar cell. Also in PSCs the back contact is typically made of ITO or, alternatively, fluorine-doped tin oxide (FTO); materials widely used in the optoelectronic and photovoltaic industry thanks to their very high transparency and conductivity [19] and usually named as transparent conductive oxides (TCOs). As shown in Figure 1.4, the ITO layer is then directly in contact with the ETL (TiO_2) acting as recombination layer with the silicon bottom cell [12, 20]. Indeed, the main structure analysed in this work is a sandwich structure composed by ITO/ TiO_2 /ITO realised on a silicon substrate.

The deposition techniques utilised are Atomic Layer Deposition (ALD), subdivided

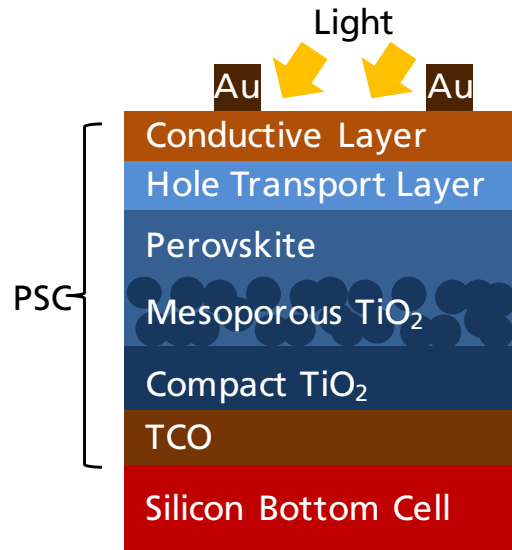


Figure 1.4: Sketch of a typical perovskite-silicon tandem solar cell, with the perovskite cell is the top cell and the silicon cell is the bottom cell. TCO stands for transparent conductive oxide.

in Plasma Enhanced ALD (PE-ALD) and Thermal ALD (T-ALD) and reactive Electron Beam Physical Vapour Deposition (EBPVD). The former ideally permits a very uniform and thickness controlled deposition through a sequential deposition of single atomic layers but requires quite long deposition time and medium-high temperature ($\sim 200^\circ\text{C}$) and furthermore higher associated costs, while the latter allows a very fast and low cost coating at room temperature. Thermal treatments (annealing) of films at different temperatures and exposure times are then performed to study the influence on carrier transport. The results show a strong dependency of the layer electrical resistance on the annealing parameters, generally with an increase of the conductivity after the exposure.

To perform the analysis, it has been necessary to design a test structure and to test different types of sample dicing methods of wafers as they can show shunts derived from the cut itself. To better understand the conduction properties of films also Dark Lock-In Tomography analysis has been performed to investigate the presence of pinholes in TiO_2 films and X-ray Diffraction (XRD) in parallel with X-ray Photoelectron Spectroscopy (XPS) were performed to investigate the crystalline and chemical structure before and after thermal annealing.

The tested ITO/ TiO_2 structures have been used to realise perovskite solar cells which power conversion efficiencies (PCEs) have been measured and compared with the series resistance of the cells and the series resistance of the studied layers. Perovskite-silicon tandem solar cells will be investigated later on, after this work.

1.3 Outline of this work

In Chapter 2, the theory of semiconductor junctions, which are the basis of solar cells, will be shown with particular attention to the heterojunction theory and their relative band structure. In Section 2.2 the description of a perovskite-silicon tandem solar cell will be presented, focusing on the charge selective layers and their role in the free carrier collection and extraction. Afterwards, a more detailed description of the electronic properties of ITO/TiO₂ stack will be given.

In Chapter 3, experimental methods employed in this thesis will be presented, starting with the detailed description of ALD and EBPVD techniques for TiO₂ film depositions. In Section 3.2 the entire sequence of the sample preparation process is presented and in Section 3.3 the of perovskite solar cells is briefly described. In Section 3.4, the used characterisation methods will be illustrated: i) the resistance measurement via a four probes setup, ii) a short description of XRD and XPS techniques to investigate the crystalline phase and chemical structure of the different TiO₂ films, iii) the Dark Lock-In Thermography (DLIT) method to investigate the possible presence of pinholes and shunts at the edges.

In Chapter 4 all the results for each characterisation technique will be presented and discussed separately. At first, results from the dicing experiment, using in addition reference samples without TiO₂ and samples where the TiO₂ layer is replaced with insulating aluminium oxide (Al₂O₃), are shown in parallel with the DLIT investigation to highlight the samples quality for current transport investigation. Then, the results of the resistance measurements for all the different deposition techniques before and after thermal annealing will be analysed. Finally, XRD and XPS results will be discussed to study any possible correlation between the crystalline and chemical structure with the electrical properties. The presented results are compared to results reported in the present literature. The chapter ends with solar cell results.

This work will be concluded with a brief outlook on all the resulted reported during the experimental work conducted.

Chapter 2

Theory

In this chapter, the principles of semiconductor heterojunction theory are illustrated as collection of concepts of the most accepted and modern literature. Nevertheless, an exhaustive derivation of all aspects behind the semiconductor transport theory, recombination processes and homojunction is beyond the scopes of this work and their knowledges are assumed. The following sections about heterojunction and metal – semiconductor theories are based on the works of A. G. Milnes and D. L. Feucht [21], S. M. Sze and Kwok K. Ng [22] and M. Grundmann [23].

2.1 Semiconductor Junction Theory

Even though tandem devices are complex structures, with several layers stacked together, and perovskite solar cells are composed of multiple layers of different materials, each interface can be still represented as a heterojunction between two different materials with unaligned Fermi levels, different work functions and band structures [24]. The same principles can be applied on the ITO/TiO₂/ITO stack considered in this work. More precisely, because of the metal-like properties of ITO, the stack can be modelled as a metal – semiconductor junction where a Schottky barrier can eventually arise.

When two semiconductor materials A and B are put in contact, according to the Anderson's rule, free carriers coming from one of the two semiconductors, spontaneously diffuse towards the other one and vice versa, leading to a uniform Fermi level for the whole system [24, 25]. From this, several ways of band alignment can arise depending on the properties of the two materials. In the simplest junction, A and B are composed by the same semiconductor with different doping, for instance p and n -silicon. This is the so-called p - n homojunction, where the two materials share the same energy gap but different position of the Fermi levels within the bands. In this junction, the alignment of the Fermi levels brings to a uniform and smooth bending of the valence band and conduction band

(E_V, E_C) . In a heterojunction, A and B are two different semiconductors with distinct energy gaps. Also in this case an alignment of the Fermi levels occurs, but due to the band offset, an abrupt energy barrier can arise at the interface. A third type of junction arises when a semiconductor is kept in contact with a metal. In this case, the Fermi level (E_F) of the metal does not lie within a forbidden energy gap and the alignment of Fermi level of the only semiconductor creates eventually a Schottky barrier with rectifying properties and which sign depends on the semiconductor doping (p or n) or, alternatively an ohmic contact can take place [24].

2.1.1 Heterojunction Theory

Consider now two different semiconductors of different types, each of them characterised by its own energy gap E_g , work function ϕ and electron affinity χ which represent the energy difference between the conduction and the valence band, the energy required to remove an electron from the Fermi level E_F to the vacuum and the energy required to remove an electron from the minimum of the conduction band E_C to the vacuum, respectively. Because of their definitions, it's easy to see that ϕ is depending on the doping since E_F position varies with it while χ is invariant.

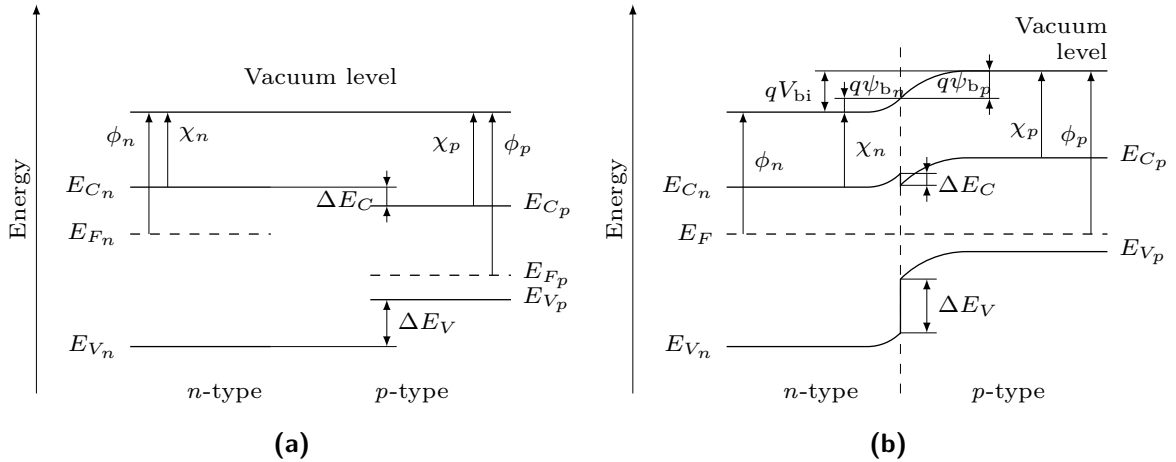


Figure 2.1: n - p heterojunction (a) before and (b) after contact.

As shown in Figure 2.1, after the contact the difference of the two Fermi levels leads the electrons to flow from the n -type semiconductor to the p -type causing the alignment of the Fermi levels and the band bending at the interface, with abrupt steps due to the difference of conduction bands minima ΔE_C and valence bands maxima ΔE_V . Let us define now $q\psi_{bn}$ and $q\psi_{bp}$ the shifts of the two vacuum levels from their original value before the contact to their new position after the contact, in respect of the interface as shown in Figure 2.1b. We can then say that the Fermi levels difference $\Delta E_F = E_{Fp} - E_{Fn}$

before the contact took place, corresponds to

$$E_{F_p} - E_{F_n} = q(\psi_{bn} + \psi_{bp}) = qV_{bi} \quad (2.1.1.1)$$

where the right-hand side is the difference of the two vacuum levels *after* the contact, V_{bi} is the so-called *built-in* potential and q is the elementary charge of the carrier. Because after the contact $E_{F_p} - E_{F_n} = 0$, from the definitions of work function, the built-in potential can be also rewritten to the form

$$V_{bi} = |\phi_n - \phi_p|. \quad (2.1.1.2)$$

The analysis of the heterojunction electronic properties is more complex compared to a simple ideal homojunction, but can be considerably simplified if we assume that band bending transition occurs only within a small region close to the interface, or alternatively that depletion region is small. This can be translated as thinking that after distances x_n and x_p from the interface in the corresponding regions, the bands are completely flat, where, for charge conservation

$$\frac{x_n}{x_p} = \frac{N_A}{N_D} \quad (2.1.1.3)$$

with N_D and N_A are the *donor* and *acceptor* atom concentrations [21]. Always using a geometrical construction, the abrupt steps of ΔE_C and ΔE_V can be calculated as

$$\Delta E_C = \chi_n - \chi_p, \quad (2.1.1.4a)$$

$$\Delta E_V = (E_{gn} - E_{gp}) - (\chi_n - \chi_p). \quad (2.1.1.4b)$$

It also simply follows that

$$\Delta E_C + \Delta E_V = E_{gn} - E_{gp} = \Delta E_g. \quad (2.1.1.5)$$

What was shown so far is calculated for a n - p heterojunction, but the above equations must be valid also in the opposite case of a p - n heterojunction, taking care of signs [21].

Let us consider, for better understanding, an ideal p - n homojunction. When we treat non-degenerate semiconductors, i.e. when the Fermi level lies within the band gap ($|E - E_F| \gg k_B T$), then the Fermi-Dirac distribution can be expressed by [26]

$$f_{FD}(E) = \frac{1}{\exp\left(\frac{E - E_F}{k_B T}\right) + 1} \approx \exp\left(-\frac{E - E_F}{k_B T}\right) \quad (2.1.1.6)$$

that permits to calculate the free charge carrier concentrations in the two doped regions of an extrinsic semiconductor, at thermal equilibrium, by the Boltzmann relations

$$n_0 = n_i \exp\left(\frac{E_{F_n} - E_i}{k_B T}\right) \quad (2.1.1.7a)$$

$$p_0 = n_i \exp\left(\frac{E_i - E_{F_p}}{k_B T}\right) \quad (2.1.1.7b)$$

where n_i is the intrinsic carrier concentration, E_i is the Fermi level of the intrinsic semiconductor and k_B is the Boltzmann's constant. Even for extrinsic semiconductor the relation $p_0 n_0 = n_i^2$ still holds at thermal equilibrium. When a bias voltage V is applied to the junction, the carrier densities change and the Fermi levels are replaced with the quasi-Fermi levels and currents start flowing inside the device. From the continuity equations and carrier recombination dynamics it can be demonstrated that the minority-carrier diffusion currents are given [27] by

$$J_p = -qD_p \left. \frac{dp_n}{dx} \right|_{W_{D_n}} = \frac{qD_p p_{n_0}}{L_p} \left[\exp\left(\frac{qV}{k_B T}\right) - 1 \right] \quad (2.1.1.8a)$$

$$J_n = -qD_n \left. \frac{dn_p}{dx} \right|_{-W_{D_p}} = \frac{qD_n n_{p_0}}{L_n} \left[\exp\left(\frac{qV}{k_B T}\right) - 1 \right] \quad (2.1.1.8b)$$

where p_n , n_p and p_{n_0} , n_{p_0} are the minority-carrier concentrations at non-equilibrium and at equilibrium, D_i is the diffusions coefficient, L_i is the carrier diffusion length and W_{D_i} is the depletion region width of the corresponding side ($i = p, n$). Thus, summing up the two contribution of currents (2.1.1.8) we obtain the well known Schottky relation for the total current of the p-n homojunction

$$J = J_n + J_p = J_0 \left[\exp\left(\frac{qV}{k_B T}\right) - 1 \right] \quad (2.1.1.9)$$

which is, indeed, the ideal diode equation [22].

Returning to the initial discussion about heterojunction, if one assumes that the condition of smooth transition (2.1.1.3) far from the interface still holds, then the relations for the diffusion currents can be applied also to the heterojunction, taking care to adjust all coefficients for the two regions. Therefore, the equations (2.1.1.8) become

$$J_n = \frac{qD_{n_p} n_{i_p}^2}{L_{n_p} N_{A_p}} \left[\exp\left(\frac{qV}{k_B T}\right) - 1 \right] \quad (2.1.1.10a)$$

$$J_p = \frac{qD_{p_n} n_{i_n}^2}{L_{p_n} N_{D_n}} \left[\exp\left(\frac{qV}{k_B T}\right) - 1 \right] \quad (2.1.1.10b)$$

and, likewise to the total current density of the homojunction, the total current density for the heterojunction is given by [21, 27]

$$J = J_0 \left[\exp\left(\frac{qV}{k_B T}\right) - 1 \right]. \quad (2.1.1.11)$$

Despite the heterojunction charge diffusion transfer characteristic (2.1.1.11) appears to be completely identical to that one of standard homojunction, its behaviour is governed and tuned by the parameters of the two distinct semiconductors instead of only

one as in case of homojunction. Even though the Shockley model well predicts simply interfaces at low current densities, it is limited by several factors neglected in a first approximation, such as the presence of a parasitic series resistance, surface defects, generation and recombination of carries in the depletion region and the tunnelling effects.

2.1.2 Metal – Semiconductor Junction

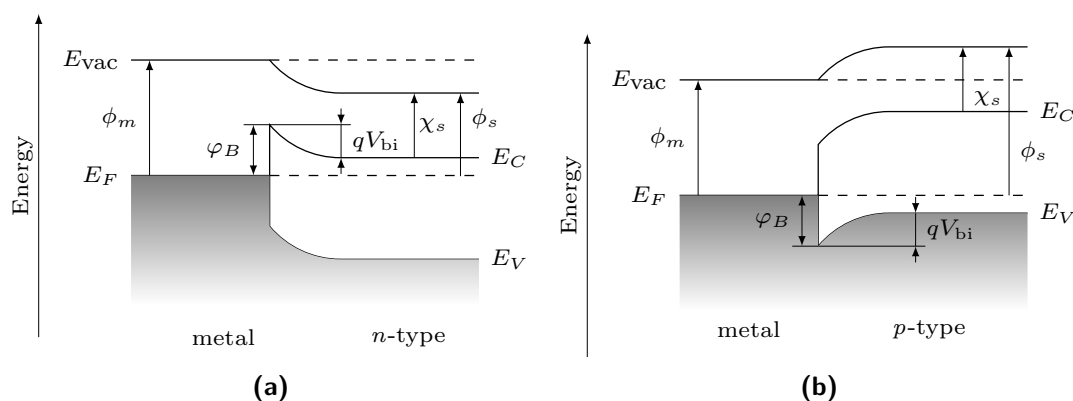


Figure 2.2: Two metal – semiconductor junctions with different doping: n -type and p -type semiconductors. If the semiconductor is n -type (a), the Schottky barrier φ_B hinders electrons coming from the metal towards the semiconductor. If it is p -type (b) the barrier affects holes flowing in the same direction. In both cases a smaller barrier qV_{bi} exists for carriers flowing from the semiconductor to the metal.

The same phenomena of Fermi levels alignment and band bending are also observed when a semiconductor is brought in contact with a metal, with the main difference that in a metal there is no energy gap and the Fermi level lies within a band. After the contact, the band structure of the metal remains substantially unaltered while, at thermal equilibrium, the free charge diffusion, responsible for the Fermi level of the semiconductor alignment with the metal one, causes the bending of the semiconductor energy bands depending on its doping. Consider now a junction between a metal and a n -doped semiconductor, as shown in Figure 2.2a and define again the electronic affinity of the semiconductor as $\chi_s = E_{vac} - E_C$ and $\phi_m = E_{vac} - E_C$ the metal work function. When the contact takes place, if $\chi_s < \phi_m$, electrons from the semiconductor diffuse into the metal, causing a shift of both E_C and E_V making them more negative at the interface. As consequence, we immediately notice the presence of a barrier at interface that obstacles the electron flow from the metal to the semiconductor. The barrier takes the well-known name of *Schottky barrier* whose height is calculated by

$$\varphi_B = \phi_m - \chi_n. \quad (2.1.2.1)$$

Similarly, as what we have seen previously for the heterojunction, a built-in potential V_{bi} is present due to the vacuum levels offset after the contact, but this time it also plays

the role of barrier for the electrons flowing from the semiconductor to the metal and, denoting ϕ_s the semiconductor work function, is given by [21, 23]

$$qV_{\text{bi}} = \phi_m - \phi_s. \quad (2.1.2.2)$$

In the opposite case, when $\chi_s > \phi_m$, there is no barrier for electrons flowing from the semiconductor to the metal and the junction becomes a simply ohmic contact. When, instead, a Schottky barrier is present ($\chi_s < \phi_m$), the metal – semiconductor junction becomes rectifying and behaves similarly to a simply p - n junction: applying a potential difference to the junction, whenever the potential over the n -semiconductor is lower than the one on the metal (forward polarisation) the barrier φ_B is lowered and an electron current is allowed. At the opposite, when the metal undergoes a lower voltage than the semiconductor (reverse polarisation) the barrier height increases creating a current interdiction, until the condition of breakdown is reached.

Under a working condition where $\varphi_B \gg k_B T$, that allows to neglect thermal fluctuations, it is a fair assumption to say that the Schottky barrier plays a lead role in the junction overall resistivity. Because in a metal – semiconductor junction two barriers are present, the total current flowing in the device is mainly due to the privileged motion of majority charge carriers from the semiconductor to the metal since affected by a smaller barrier ($qV_{\text{bi}} < \varphi_B$).

As for the heterojunction, the current density is proportional to the density of state in the conduction band and the charge transfer characteristic is calculable trough the Fermi – Dirac statistics. The complete derivation can be found in Ref. [23] and we only show that the total current density of the metal – semiconductor junction is given by

$$J = J_S \left[\exp \left(\frac{qV}{k_B T} \right) - 1 \right] \quad (2.1.2.3)$$

where J_S is the saturation current

$$J_S = A^* T^2 \exp \left(\frac{-q\varphi_B}{k_B T} \right) \quad (2.1.2.4)$$

and A^* is the Richardson's constant for thermo-ionic electron emission

$$A^* \equiv \frac{4\pi e m_n^* k_B^2}{h} \approx 120 \text{ A}/(\text{cm}^2 \text{ K}^2) \quad (2.1.2.5)$$

where e is the electron charge, m_n^* is the effective electron mass and h is the Plank constant. Inverting (2.1.2.4) we find that the Schottky barrier height is

$$\varphi_B = \frac{k_B T}{q} \ln \left(\frac{A^* T^2}{J_S} \right). \quad (2.1.2.6)$$

The two equations (2.1.1.9) and (2.1.2.6) represent, however, the ideal case. A more realistic illustration for the current density is given considering a series resistance R_S due to the contact and it leads to the expression [26]

$$J = J_S \left[\exp \left(\frac{q(V - IR_S)}{nk_B T} \right) - 1 \right] \quad (2.1.2.7)$$

where we introduced the *ideality factor* n that takes into account any not ideal aspects, such as charge recombination or losses. Thus, the series resistance can be calculated as

$$R_S = \left. \frac{\partial V}{\partial J} \right|_T \quad (2.1.2.8)$$

that is it negligible at low voltage allowing us to calculate n , which takes in account the charge carrier recombination and or defects, as

$$n = \frac{q}{k_B T} \frac{\partial V}{\partial(\ln J)}, \quad (2.1.2.9)$$

where $n > 1$ and $n = 1$ corresponds of course to the ideal case.

In the above description, we neglected every tunnelling effects trough the barrier that can effectively permit a majority carrier current also under reverse bias. This is particularly true for highly doped semiconductors, where the Schottky barrier becomes sufficiently thin to permit a tunnel current. Moreover, this simplified model only takes into account values of work functions and electronic affinities of materials before the contact, assuming that they remain unaltered after the contact, but it has been shown that these values change considerably after the contact due to defects at interface and chemical reaction between the two components.

2.2 Electronic transport in Perovskite-silicon Tandem Solar Cells

To better understand the electronic transport within a perovskite-silicon tandem solar cell, it is necessary to describe a perovskite solar cell, to define the role of its components and to clarify why it requires a well defined stack of selective contact layers for charge harvesting and collection. As these layers are necessary to have a significant power conversion efficiency (PCE) in a single PSC, in a tandem device the stack of all required layers must be designed to avoid any current losses at the interface between the PSC and silicon bottom cell as much as possible. It is also quite obvious that, in addition to having perfect electronic properties, these materials must also be optically transparent in the wavelength ranges used by the two cells, to guarantee a good energy conversion of incoming photons.

2.2.1 Perovskite solar cell (PSC)

With perovskite, a wide group of chemical compounds is meant, represented by the raw formula ABX_3 where A and B are two cations and X is an anion, with A larger than B [5, 28, 29]. In photovoltaic applications, the perovskite absorbers are mainly made of organic-inorganic halide perovskites, where A is usually methylammonium ($CH_3NH_3^+$ or simply MA) or ethylammonium ($CH_3CH_2NH_3^{3+}$) and B is commonly Pb, while the anion X is a halogen like I, Br, or Cl. At present time, the most studied perovskite structures are methylammonium lead triiodide ($CH_3NH_3PbI_3$ or $MAPbI_3$) and mixed (or hybrid) halide compounds such as $MAPbI_{3-x}Cl_x$ and $MAPbI_{3-x}Br_x$ [5, 16]. Other perovskite materials currently under investigation are $CH(NH_2)_2PbI_3$, $MASnI_3$, $CsSnI_3$ and more [24]. For all of them several deposition techniques are possible, such as spin coating or evaporation.

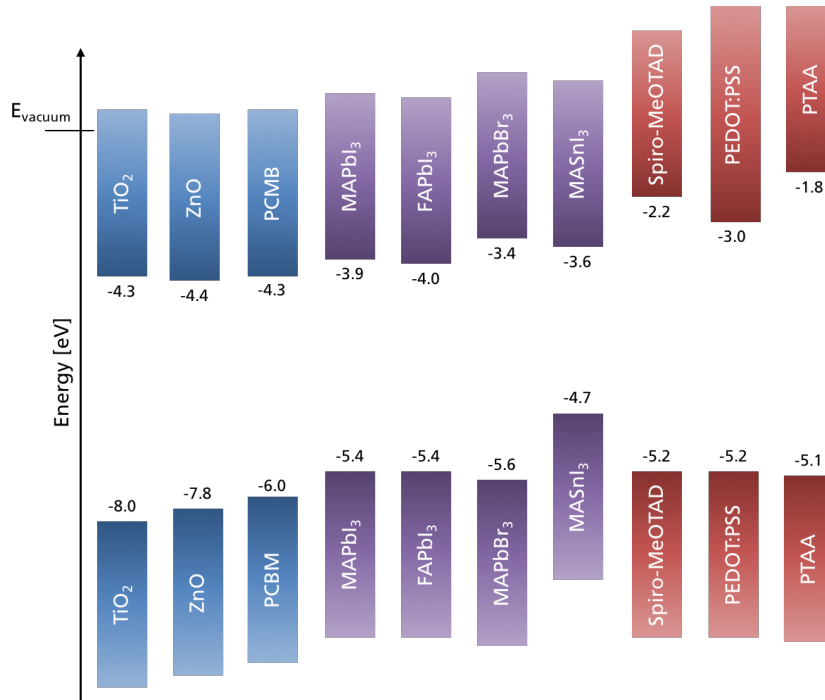


Figure 2.3: Energy bands of some of most common perovskite absorber materials [30, 31]. In blue are shown ETLs, purple perovskite absorbers, in red HTLs.

The great attraction of these materials is due to several key features that make them perfect candidates for photovoltaics applications and in particular for tandem devices: a wide and tunable energy gap within the range of about 1.55 eV and 2.28 eV, high absorption coefficients and long carrier diffusion lengths [29, 32, 33]. However, a fully working PSC is not complete until the perovskite absorber is embedded in between an Electron Transport Layer (ETL), and a Hole Transport Layer (HTL) which perform the

function of collecting and extracting the charge carrier generated within the perovskite [6].

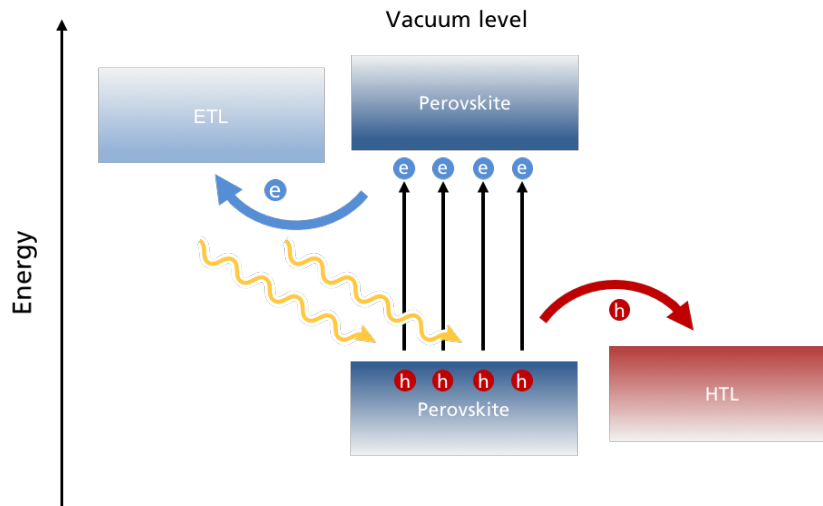


Figure 2.4: Schematic band diagram to illustrating the charge production and extraction by ETL and HTL in a Perovskite Solar Cell (picture not in scale).

When an incoming photon is absorbed by the perovskite material, a hole – electron pair (exciton) is generated. While in organic absorber materials the exciton is strongly bound and, after its diffusion to the interface, needs to be dissociated in free carriers, in perovskite materials, instead, the exciton binding energy is much lower making PSCs “silicon-like” solar cells where the photon absorption and the consequent free carrier generation are almost instantaneous [34].

ETLs and HTLs are specifically designed to have a particular energy band structure to favour the extraction of one type of charge carriers. In Figure 2.3 some of the most used and investigated ETL and HTL with their respective band structures are reported. In particular, the former must have the minimum of the conduction band E_C close in energy with the minimum of the conduction band of the perovskite absorber while the latter must have the maximum of the valence band E_V close to perovskites valence band in the way to collect a hole and electron, respectively (Figure 2.4). Having a good band alignment between the transport layers and the perovskite absorber means also to reduce energy barriers at the interface, in particular the built-in potential, that can occur. In other words, the small mismatch between the conduction band of ETL and the valence band of HTL with the correspondent perovskite band edges favours the formation of an ohmic contact. In addition to an energy barrier reduction, and thus, a current transport losses, good band alignment increases the final open-circuit voltage (V_{OC}) of the solar cell [35]. The most used ETLs are TiO_2 , ZnO , SnO_2 and [6,6]-Phenyl- C_{61} -butyric acid methyl ester (PCBM), while common HTLs are

spiro-MeOTAD, PEDOT:PSS and poly(triaryl amine) (PTAA).

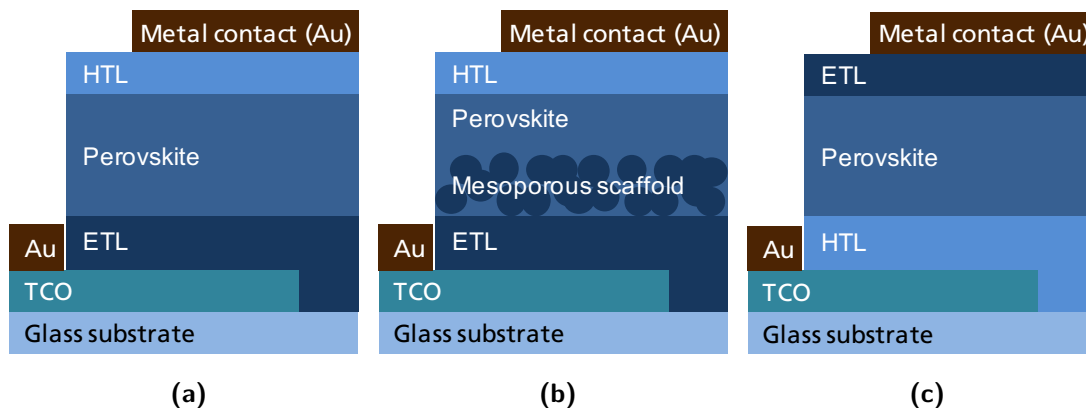


Figure 2.5: Examples of perovskite solar cells with (a) regular planar structure, (b) regular structure with mesoporous scaffold and (c) inverted planar structure. TCO refers to *Transparent Conductive Oxide*.

PSCs can have many different structures depending on different layer arrangements. The first common distinction is between the so-known *regular* and *inverted* structure. Since there is no actual preferred illumination direction (both structure can be ideally illuminated from both sides), it is commonly accepted to call the structures *regular* structure or *n-i-p*, when the ETL is the first layer deposited on the glass substrate (Figure 2.5a). Contrariwise, the *inverted* structure, or *p-i-n*, is commonly referred to cells where the HTL is the first layer deposited on the substrate (Figure 2.5c). From here onwards we will use this convention.

Since the first attempts with PSCs it has been shown that perovskite grown on electron conductive mesoporous scaffolds exhibit higher efficiencies thanks to a higher electron injection, better perovskite growth and stability [6, 15, 17, 36, 37]. As shown in Figure 2.5b, the perovskite absorber is deposited directly on the mesoporous scaffold generally made of TiO_2 or Al_2O_3 , creating nanoparticles inside the scaffold its self. In most cases the mesoporous layers were produced with a sintering step at high temperatures. This limits the choice of the substrate as well as can damage the bottom cell during the processing of a tandem device. Currently, many research groups are studying different routes to achieve the same efficiency and stability without using a high temperature sintered mesoscopic scaffold, to enable the PSC integration on substrates and devices that require low temperature processing. Examples are the planar structure with compact ETL (Figure 2.5a) or TiO_2 nanocompound solutions [38–40]. Furthermore, a new route for low temperature mesoporous TiO_2 by UV curing has been recently developed at Fraunhofer ISE [37]. Figure 2.6 shows two examples of PSCs studied at Fraunhofer ISE with mesoporous TiO_2 scaffold (Figure 2.6a) and one with inverted structure (Figure 2.6b).

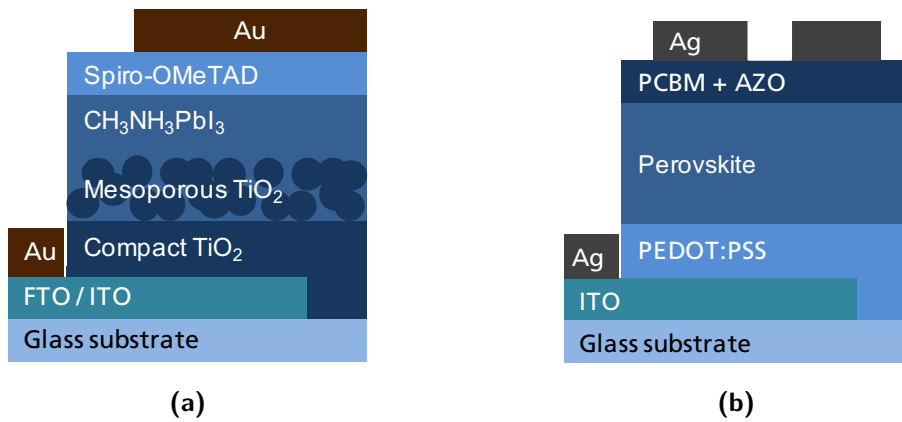


Figure 2.6: Examples of perovskite solar cells with (a) planar structure with mesoporous TiO_2 scaffold and (b) planar inverted structure realised at Fraunhofer ISE.

2.2.2 Tandem device

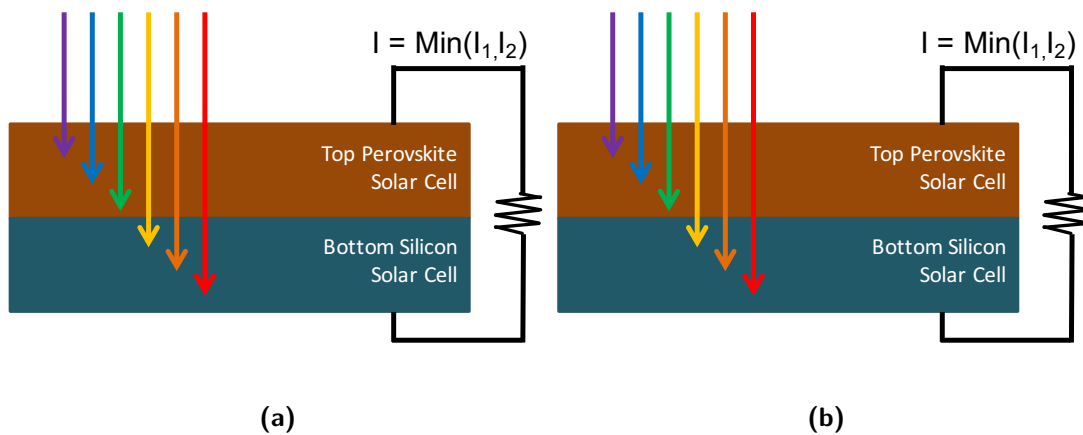


Figure 2.7: Scheme of a monolithic two-terminal (a) and mechanically stacked four-terminal (b) tandem devices. Shorter wavelength light is absorbed by the top perovskite cell and longer wavelengths by the silicon bottom cell as illustrated.

Perovskite-silicon tandem solar cells are mainly built with the two configurations shown in Figure 2.7: the monolithic two-terminal tandem structure or the mechanically stacked four-terminal tandem. Because of their energy gaps, in both cases the perovskite cell is placed on top to absorb photons with shorter wavelengths, while the silicon bottom cells is designed to absorb the photons with longer near infrared wavelengths [20, 41]. The four-terminal tandem is easier to realise since the two cells are fabricated separately. On the other hand, the two-terminal monolithic tandem has the advantage of requiring a lower number of fabrication steps as well as a lower number of electrodes, leading to potentially reduced overall manufacturing costs [41]. The advance of the two-terminal

tandem solar cells is mainly due to the easiness of the integration in modules, since less electrical connections are required and simpler electronic control unit are required, compared to a four-terminal device, where the two subcells must be handled separately (Figure 2.7).

However, monolithic tandems are not free of inconvenience since they require a chain of compatible processes for the two sub-cells. As already mentioned, perovskite cells with mesoporous TiO_2 scaffold exhibit higher performance but they are obtained with high temperature sintering. While high temperatures are compatible with c-Si sub-cells, they are problematic for high efficient a-Si:H/c-Si heterojunction cells (SHJ), which have been shown to suffer thermal instability and degradation for temperature above 200°C [20]. Another crucial aspect, that holds generally for all types of tandem cells, is that the perovskite top cell must maximise the absorption within its working wavelength range and simultaneously be transparent in the near infrared to permit the silicon bottom cell to absorb the lower energy photons (Figure 2.7).

This requirement is also equally mandatory for the interconnection layer which role is to electrically contact the two cells. For this task, transparent conductive oxides (TCO) are utilised as recombination layer of minority carriers and ohmic contact, such as indium tin oxide (ITO), indium zinc oxide (IZO) or aluminium doped zinc oxide (ZnO:Al) [42, 43]. The importance to have a good ohmic contact is to reduce the energy barrier for the majority carriers that could lead to recombination at the interfaces and then to a total current degradation [44, 45].

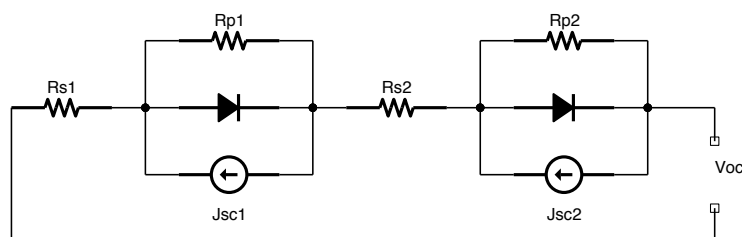


Figure 2.8: Electrical equivalent circuit of two solar cells in series with single diode model.

From an electrical point of view, we can describe a two-terminal tandem device as two distinct solar cells connected in series (as displayed in Figure 2.8). It follows that the total current flowing in the device must be the same for both cells. Because of the two current generators J_{sc1} and J_{sc2} , representing the sub-cells short circuit currents, the total current is dominated by the smaller of them. Moreover, for a given current, the total output voltage V must be the sum of the two output V_1 and V_2 produced by the two individual subcells at the same current. Another requirement resulting from series connection is that the bias of the two sub-cells must have the same sign. In other words,

this means that, if p -side of the top cell is under illumination, the p -side of the bottom cell must be connected to the n -side of the top cell. To connect the two sub-cells, two routes are possible. One is to interpose a transparent conductive oxide (TCO) between the p and n sides of the two cells, as illustrated in Figure 2.9. Such kind of contact leads to a recombination of electrons coming from the n -side of the top cell with the holes coming from the p -side and the TCO acts as carriers emitter for the two sub-cells. In this way, the majority carriers flow with the same direction along the whole tandem cell and they can be collected out by the two metal contacts. A second option is to replace the TCO with two oppositely highly doped semiconductors (n^{++}/p^{++}) creating a tunnel junction at the interface. But because of the high dope, then the tunnel junction becomes very thin and the free carrier absorption can be enough small to not significantly compromise the overall performance [46], allowing also in this case the recombination between holes and electrons near to the interface.

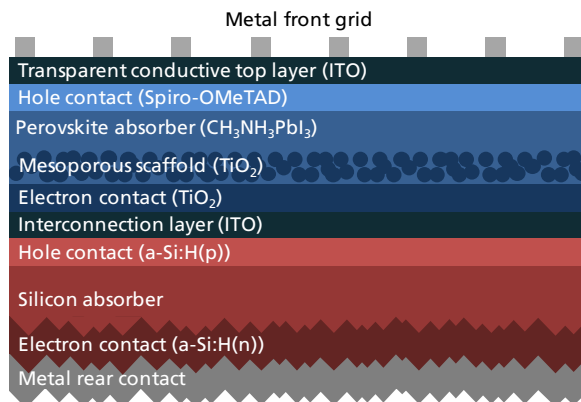


Figure 2.9: Monolithic two-terminal Perovskite-silicon tandem solar cell under production at Fraunhofer ISE.

2.2.3 Interconnection ITO – TiO₂ stack

As already mentioned, the top layer of silicon heterojunction solar cells (SHJ) is generally made of ITO [18], while PSCs studied at Fraunhofer ISE present a low temperature processed mesoporous TiO₂ scaffold coated on a compact TiO₂ layer. It is then clear that is necessary to investigate the properties of the at the interface between the ITO and compact TiO₂ layers, where ITO, in addition to be the front contact of the SHJ cell, plays the role of recombination layer for this kind of device.

TiO₂ exists in several different phases, amorphous and crystalline phase such as Anatase or Rutile or, more likely, in mixtures of them and its chemical composition can also vary in a more realistic form of TiO_x. For these reasons, it is not a trivial task to define electronic properties of this material that are also affected by the deposition techniques, which can produce defects in the bulk as well as at the surface. Nevertheless, TiO₂ is typically a *n*-type semiconductor with an estimated energy gap of approximately 3.0 eV – 3.3 eV [31, 47] and electronic affinity about 4.1 eV – 4.4 eV [48, 49]. ITO, instead, is a heavily doped *n*-type wide band gap semiconductor ($E_g = \sim 3.5 \text{ eV} - 4.3 \text{ eV}$) with the Fermi level E_F located very closely to the conduction band maximum E_C [19]. Thanks to these properties ITO is so well conductive that it can be considered metal-like but still transparent in the low visible and the near infrared range. Depending on the surface treatment and deposition technique, ITO work function ϕ_m can vary considerably [50]. Nevertheless, the most accepted value of ITO work function is about 4.7 eV [51–53]

Considering ITO as a pure metal, the ITO – TiO₂ interface can be modelled as a metal – *n*-type semiconductor junction where a Schottky barrier is present, since $\phi_m > \chi_s$ and a rectifier behaviour is expected. In reality, it has been shown that, even if the barrier height cannot be modified as it depends on the fixed values ϕ_m and χ_s (equation (2.1.2.1)), its width can be drastically reduced by increasing the TiO₂ work function. In fact, ϕ_s of

TiO₂ can be quite different depending on the deposition technique and can be changed with post-deposition treatment like annealing or UV irradiation [48, 54] and thus, the probability of tunnelling through the barrier is significantly enhanced. If this would be the case, then a good ohmic contact with sufficiently low resistance could be achieved maintaining the electron transport properties of TiO₂.

Chapter 3

Experimental Methods

In this Chapter, a detailed description of the used experimental methods is presented, with particular focus on the Atomic Layer Deposition and the Electron Beam Physical Vapour Deposition used for thin TiO₂ film coating. Afterwards, the preparation of the samples and the characterisation methods used to study the electrical and physical properties of the ITO/TiO₂/ITO stack are described.

3.1 Film preparation

3.1.1 Atomic Layer Deposition (ALD)

Atomic Layer Deposition is a thin film deposition technique that permits to grow a wide selection of materials from vapour gases (precursors). Although it relies on the chemical reactions of two precursors with the substrate, it differs from a traditional chemical vapour deposition (CVD), where the reactants are introduced simultaneously in the reaction chamber. During ALD, the precursors are introduced sequentially in two separate steps and they chemically adsorb on the layer deposited in the step before. The main advantage of ALD is that the two reactions are self-limited, guarantying a very precise control of the deposition process due to a monolayer by monolayer growth, and thus of the thickness, as well as a very high homogeneity of the films surface [55–58].

Figure 3.1 shows a complete ALD cycle: during the first step, the first reactant is introduced into the reaction chamber and it is adsorbed onto the substrate until the surface is completely covered forming one monolayer. Because of the self-limiting reaction, the gas remaining in the reactor, plus any eventual reaction product, is purged out by an inert purging gas, such as pure nitrogen or argon. Therefore, the second step of the process starts introducing the second precursor that reacts with the monolayer just deposited by the first reactant until the surface is again completely covered. Once the

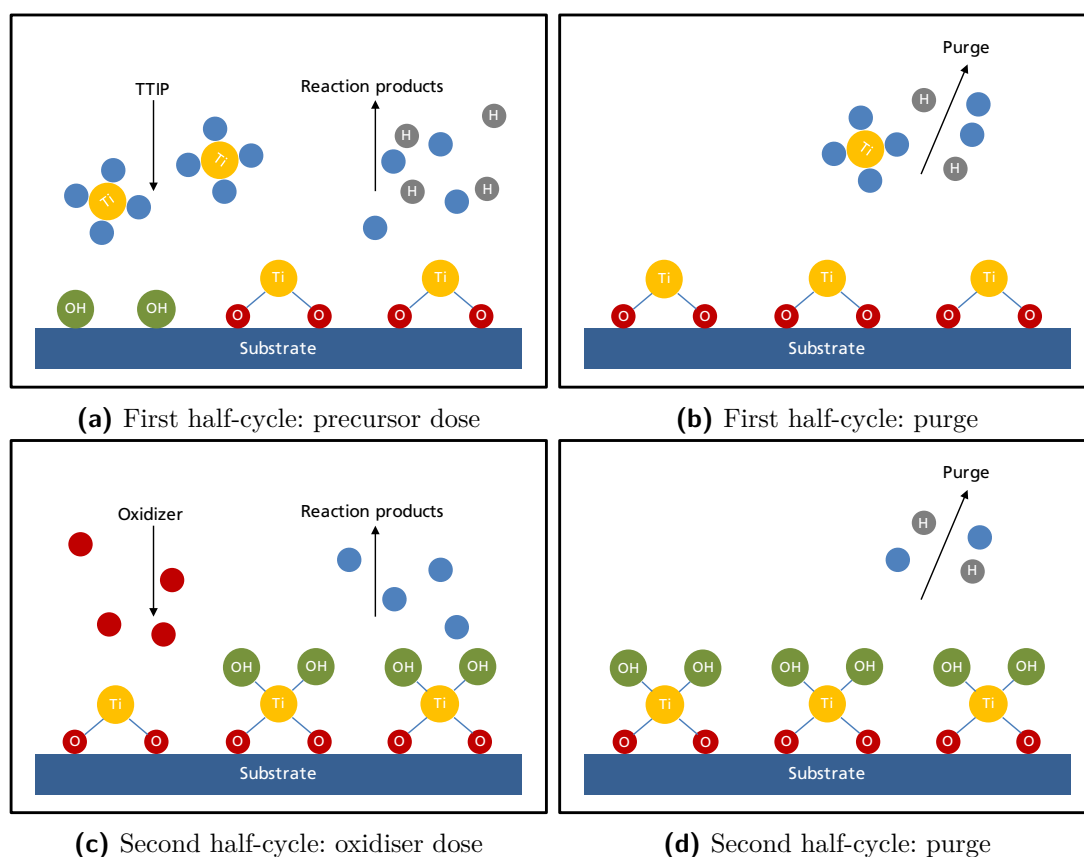


Figure 3.1: A complete ALD cycle: during the first half of cycle (a) and (b) the first precursor, as for instance titanium tetraisopropoxide (TTIP), reacts with the substrate and the reaction stops when the whole surface is covered. In the second half (c) and (d) the oxidiser is pumped into the chamber completing the reaction. When all sites are oxidised the first layer is deposited and another cycle is repeated.

second precursor gas and all the reaction residues are purged out of the chamber, an entire cycle is concluded and the first layer of the desired material is deposited. Then the cycle is repeated as many times as needed to get the desired thickness.

Many ALD variants are possible and among those Thermal ALD and Plasma Enhanced ALD are commonly used. To grow TiO_2 films, several titanium precursors can be used, such as titanium chloride TiCl_4 or titanium tetraisopropoxide $\text{Ti}\{\text{OCH}(\text{CH}_3)_2\}_4$ (TTIP), while trimethylaluminium (TMA) is commonly used to grow Al_2O_3 . Oxidiser can be water vapour, hydrogen peroxide (H_2O_2), plasma O_2 and ozone (O_3) [59]. Both TiO_2 and Al_2O_3 were grown through a FlexAL reactor from Oxford Instruments, which provides either Thermal ALD or Plasma Enhanced ALD. For each deposition, a silicon sample was coated together with the substrates for thickness control and then measured by ellipsometry. All the ALD processes described in following paragraphs are standard

processes developed prior to this work and in Table 3.1 the parameters used are reported.

Table 3.1: Summary table of TiO₂ and Al₂O₃ films grown by ALD.

Film	Process	Precursor	Oxidiser	Precursor dose (s)	Oxidiser dose (s)
TiO ₂	T-ALD	TTIP	H ₂ O	1.2	6
	PE-ALD	TTIP	Plasma O ₂	1	6
Al ₂ O ₃	PE-ALD	TMA	Plasma O ₂	0.02	2

Thermal ALD

In Thermal ALD (T-ALD), in particular the oxidising reactions are mainly driven by a relative high temperature of the substrate. A relative high temperature is also needed to prevent the gas condensation but, at the same time, it must be not too high to evaporate the layers already deposited [55]. Additionally, each step, in particular the precursor dose, must be long enough to guarantee a complete adsorption over the surface.

TiO₂ films were grown with TTIP (g) as titanium precursor and H₂O (g) as oxidiser at 200 °C. The deposition starts with vacuum pumping for 30 s, followed by a pre-heat of the samples for 2 min at 500 mTorr to efficiently reduce the temperature and a pump-down to the base pressure (7.8 mTorr) for 5 s. The cycle is composed of a TTIP dose 1.2 s long, then the chamber is purged with argon for 3 s. The chamber is pumped down to base pressure for 3 s and a pressure of around 80 mTorri is build with argon for 3 s. Then a pulse of 6 s provided the water followed by a 30 s purge. In Figure 3.3b a complete cycle is illustrated.

Plasma Enhanced ALD

The main advantage of Plasma Enhanced ALD (PE-ALD) is to create electronically charged free radicals of the oxidiser (O₂) by a plasma, and thus increasing its reactivity [55]. This allows for an ideally faster TiO₂ deposition with a higher growth per cycle (GPC) rate and depositions at rather low temperature, e.g. even at room temperature. Nevertheless, also in this case 200 °C base temperature of the substrate was set for both TiO₂ and Al₂O₃ depositions. The O₂ plasma source used in this work was the inductively coupled plasma configuration shown in Figure 3.2, generated through a radio-frequency (RF) coil powered at 300 W with a frequency of 15.6 MHz.

The TiO₂ deposition starts with a 30 s long plasma gas stabilisation followed by a pre-heat step for 2 min at a pressure 500 mTorr and a second pre-heat step for 1 min at a pressure 200 mTorr. Then, each cycle consists for a TTIP pulse of 1 s and 3 s purge

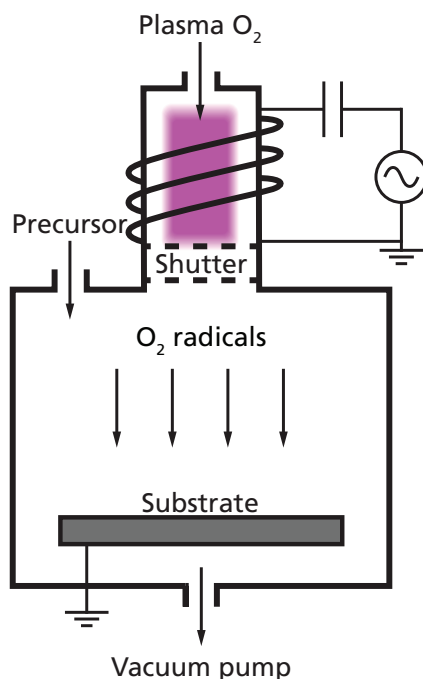


Figure 3.2: Scheme of a ALD reactor featuring a RF coil for PE-ALD deposition. During a PE-ALD deposition, in the first half of the cycle the precursor is introduced in the chamber. In the second half of cycle, an inductively induced plasma of ionised O_2 is generated through the RF coil, bombarding the substrate and completing the deposited layer. In a T-ALD deposition, the first half of cycle is substantially the same as for PE-ALD while, in the second half, the oxidiser is introduced as water vapour.

with argon. Afterwards, the plasma gas is stabilised for 1.5 s and is maintained for 6 s (Figure 3.3b).

To grow Al_2O_3 films, trimethylaluminium ($Al(CH_3)_3$ or TMA) was utilised as metal-organic precursor in combination with plasma O_2 . The chamber is pumped down to the base pressure for 1 min, then the substrate is heated for 3 min at $200^\circ C$ with a pressure set of 200 mTorr. Then the chamber is pumped down to around 80 mTorr for 5 s follows. The reaction starts with a TMA pulse of 20 ms follow by a 2 s argon purge. After a plasma gas stabilisation for 1.5 s, plasma is maintained for 2 s. Finally, the cycle ends with an after-plasma purge of 800 ms (Figure 3.3c). An oxygen flow of 60 sccm is kept active for the whole cycle.

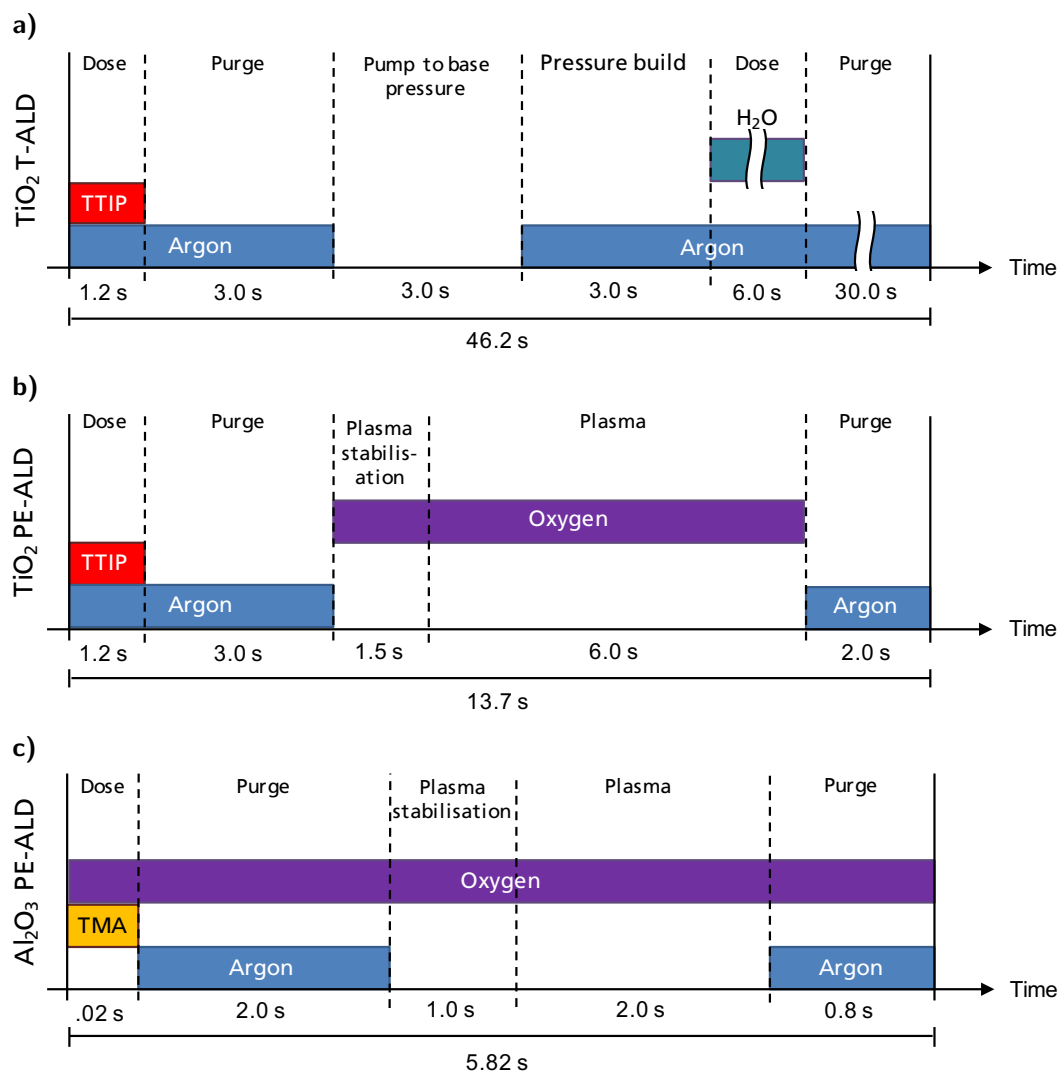


Figure 3.3: Time evolution of a complete ALD cycle of (a) TiO₂ T-ALD, (b) TiO₂ PE-ALD and (c) Al₂O₃ PE-ALD. With different colours are depicted the gases in the chamber. The drawing is not in scale.

ALD Growth Per Cycle rate (GPC)

For both T-ALD and PE-ALD techniques, thickness variation batches were performed permitting to estimate the growth per cycle (GPC) and to identify the presence and thickness of a native silicon oxide on the coated samples used for thickness control. The thickness of the TiO₂ films deposited was measured with spectroscopic ellipsometry described in Section 3.4.2. GPCs of 0.413 Å/cycle for T-ALD and 0.448 Å/cycle for PE-ALD were calculated by the slopes of the fits shown in Figure 3.4, while the intercepts indicated the presence of a native oxide on the silicon samples used. Since a native oxide should not be present on the ITO layer to be coated with TiO₂, a rough estimation of the thickness of the TiO₂ films can be calculated by

$$d = \text{GPC} \times \text{No. of cycles.} \quad (3.1.1.1)$$

From the calculated thickness listed in Table 4.1, it is possible to appreciate the final thickness precision of the TiO₂ films grown with both T-ALD and PE-ALD. The deposition of a 20 nm thick TiO₂ layer through PE-ALD took around 1 h 40 min, while the deposition of the same thickness by T-ALD took more than 6 h 40 min, requiring overnight runs per each substrate.

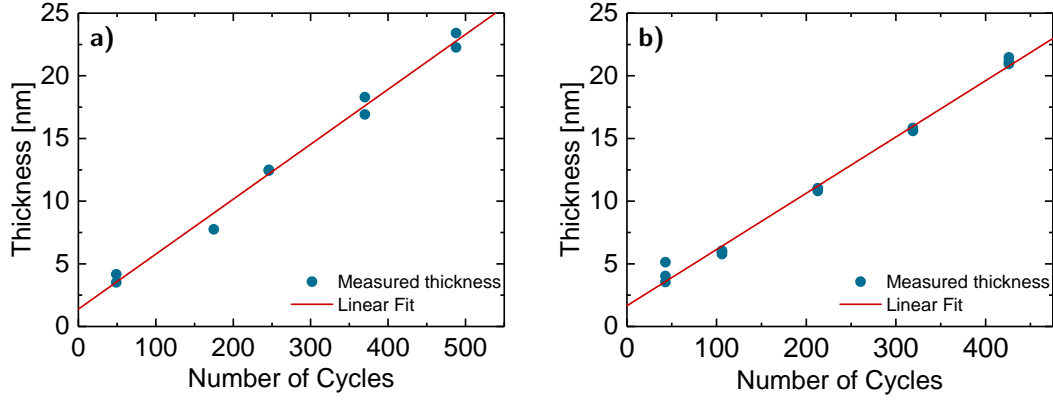


Figure 3.4: Measured thickness of TiO₂ films deposited on silicon deposited by (a) T-ALD and (b) PE-ALD in function of number of cycles used during the ALD processes. The growth per cycle (GPC) is calculated as the slope of the linear fit.

Table 3.2: ALD processes for TiO₂ films: the growth per cycle (GPC) and the native oxide thickness are calculated as slope and intercept of the two linear fits shown in Figure 3.4. The thickness is calculated by multiplying the GPC times the number of ALD cycles used for each deposition.

ALD Process	GPC (Å/cycle)	Native oxide thickness (nm)	No. of cycles	Nominal Thickness (nm)	Thickness (nm)
T-ALD	0.413	1.75	49	2	2.11
			123	5	5.30
			246	10	10.6
			370	15	16.0
			488	20	21.0
PE-ALD	0.448	1.66	43	2	1.92
			106	5	4.75
			213	10	9.54
			319	15	14.3
			426	20	19.1

3.1.2 Electron Beam Physical Vapour Deposition (EBPVD)

In Electron Beam Physical Vapour Deposition, an electron beam is generated through a current-carrying tungsten filament by thermo-ionic effect and accelerated by a high voltage within the range of 3kV – 40kV. As shown in Figure 3.5, a magnetic field B is induced perpendicularly to the direction of the beam, focusing it towards the ingot containing the material to evaporate, in this case Ti_2O_3 . Pure oxygen is injected into the chamber reacting with the evaporated titanium particle to form TiO_x . The so formed molecules are then attracted towards the electrically charged samples and they precipitate onto the substrates to form the film. To guarantee a homogeneous coating, the sample holders rotates during the deposition, while a shutter controls the deposition window time, letting the evaporated material reach the samples or blocking it to stop the deposition.

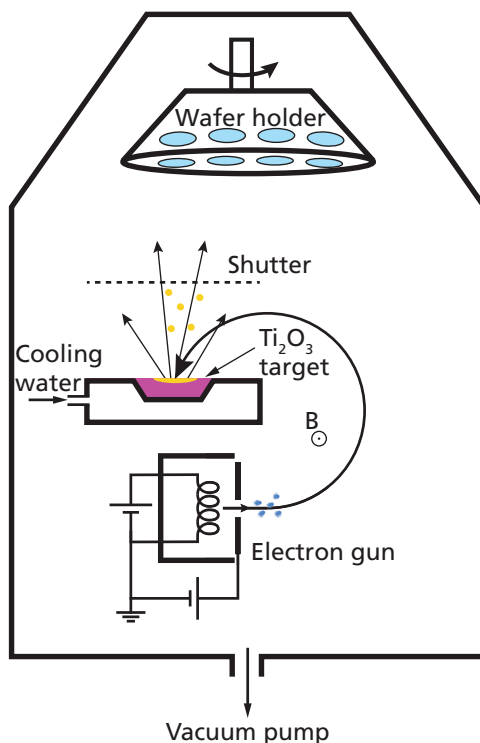


Figure 3.5: Schematic sketch of an electron beam evaporation system.

The technique requires a very high vacuum grade, since the mean free path of the evaporated particles is very sensitive to the impurity density in the chamber. Indeed, the vacuum grade of the chamber, in addition to provide a more impurity-free coating, drastically affects the deposition rate that can span from some nm per minute up to several μm per minute.

The main advantages of the EBPVD are a very fast deposition rate and the entire

process is performed at room temperature. On the other hand, since the TiO_2 deposition rate is around 1 nm/s and thus, it takes around 20 s to deposit 20 nm thick film, the shutter closing time is not negligible and this leads to a less precise control over the final thickness of the films. Hence, the thickness precision of EBPVD is in the order of some nm, fairly worse than ALD that can achieve a precision in the order of some Å.

To deposit the ETL of the stack shown in Figure 3.1b and Figure 3.1c, 20 nm thick TiO_2 was evaporated on ITO in a Pfeiffer PLS 570 evaporation system by a Telemark Model 267 electron gun. During the process the pressure was 10^{-4} mbar and the temperature around 20 °C.

3.2 Sample preparation

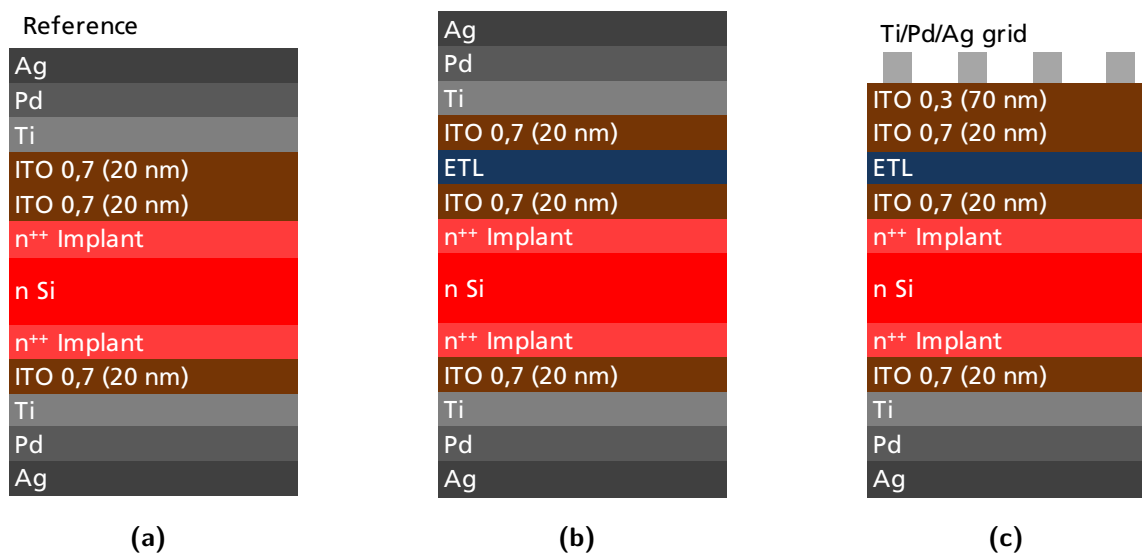


Figure 3.6: Structures analysed to investigate the resistance of the ITO/ TiO_2 /ITO stack: (a) reference samples without TiO_2 layer; (b) samples for resistance measurements. ETL represents TiO_2 deposited with different techniques. For some samples ETL is replaced with insulating Al_2O_3 . (c) samples for DLIT images. The front metal contact is replaced with a metal grid. In this case ETL indicates only TiO_2 .

Each substrate is made of an *n*-type Float-zone 200 μm thick 4-inch silicon wafer, with a crystal orientation of $\langle 100 \rangle$ and a resistivity of $\rho = 1 \Omega \text{ cm}$. In order to form a ITO/*c*-Si contact with a very low contact resistivity, the *c*-Si wafer was subjected to heavy phosphorus diffusion after a standard RCA clean procedure (including an additional HNO_3 cleaning step). Then n^{++} emitters were diffused from a phosphosilicate glass (PSG) formed from phosphoryl chloride (POCl_3) at 840 °C for one hour, resulting in a sheet resistance $R_{\text{sheet}} = \sim 50 \Omega/\text{sq}$. Finally, the PSG was etched away for five minutes in a

buffered oxide etch.

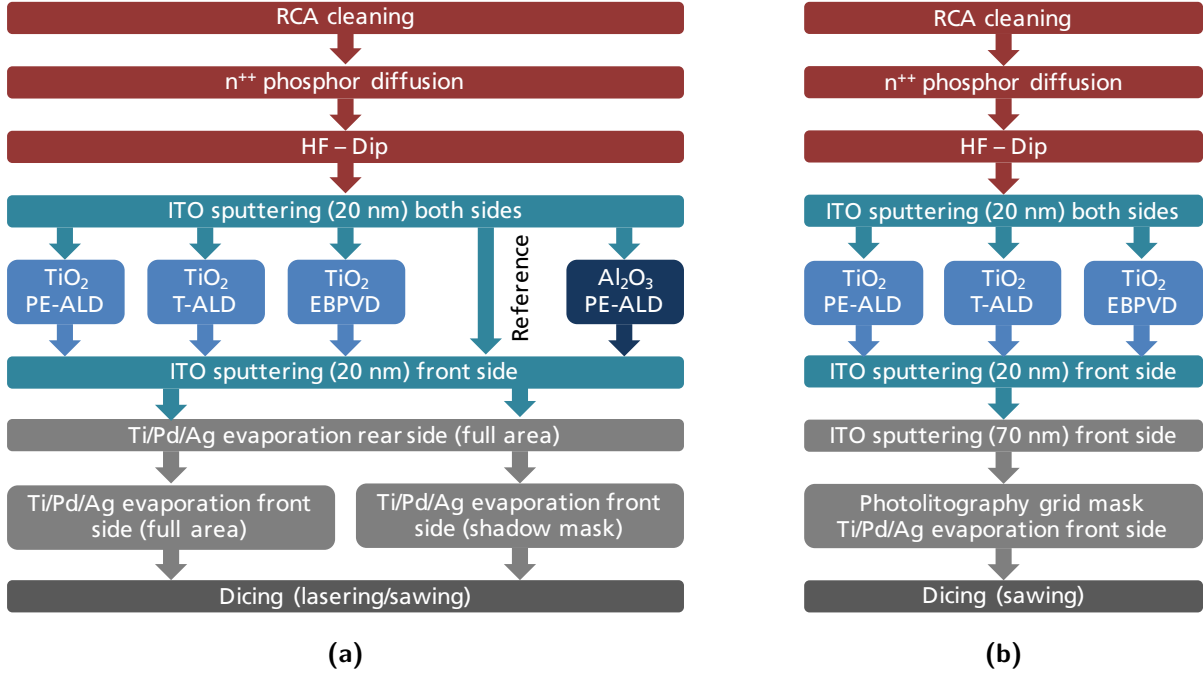


Figure 3.7: Samples processing from the silicon substrates to the final structure. In red substrate preparation in clean room; in blue ITO/TiO₂/ITO stack deposition; in grey metal contact evaporation and dicing. (a) process chain for reference and resistance measurement samples shown in Figure 3.8a and (b) process chain of samples with metal grid for DLIT probe (Figure 3.8b).

After 20s etching in 1% HF (hydrofluoric acid) to remove a native silicon oxide, 20 nm ITO layers are sputtered, using a standard process for SHJ cells, on both sides of the wafers with a Plasmalab System 100 from Oxford Instruments at 100 °C for 54s, with 0.7 sccm oxygen flow. The choice to sputter ITO also the back side of the silicon wafer is motivated to avoid the formation of a native oxide that would require a second, subtle, one-side HF etching with the risk of damaging the active front surface.

On the top ITO layer (Figure 3.6b), the electron transport layer (TiO₂) was deposited via Plasma Enhanced Atomic Layer Deposition (PE-ALD), Thermal ALD (T-ALD) or reactive Electron Beam Physical Vapour Deposition (EBPVD). In a first place, for every deposition methods the desired TiO₂ thickness is 20 nm, the standard utilised at Fraunhofer ISE for perovskite ETLs. In a second place, TiO₂ thickness variation experiments were conducted to study the dependence of film resistance as function of the thickness. As first experiment, some samples were prepared replacing the TiO₂ layer with 20 nm Al₂O₃ (deposited by PE-ALD) as insulator to investigate eventual shunts generated during dicing, while for every batch samples shown in Figure 3.6a without ELT were made as baseline references.

All the samples were then sputtered with a second ITO layer identical to the first one; for very highly conductive reference samples, the second ITO layer was deposited directly on the first one. The final stacks shown in Figure 3.6a and Figure 3.6b were then finished by the evaporation of metal contacts, composed of 50 nm thick Ti, 50 nm thick Pd and 1000 nm thick Ag stacks on both sides.

Since DLIT probe requires that layers to analyse are faced to the IR sensitive camera, a full metal top contact is not suitable. The top contact is thus replaced by a 50 nm Ti, 50 nm Pd, 2000 nm Ag grid in the active $2 \times 2 \text{ cm}^2$ area, with a finger width of $30 \mu\text{m}$ and a finger pitch of $800 \mu\text{m}$, which was realised by photolithography and metal evaporation (Figure 3.6c). To guarantee a better perpendicular current flow, a 70 nm ITO layer with lower sheet resistance ($\sim 60 \Omega/\text{sq}$) was interposed between the top ITO layer and the metal grid, obtained with 0.3 sccm oxygen flow for 2 min 50 s. In figure Figure 3.7, all processing steps of all the analysed devices are illustrated.

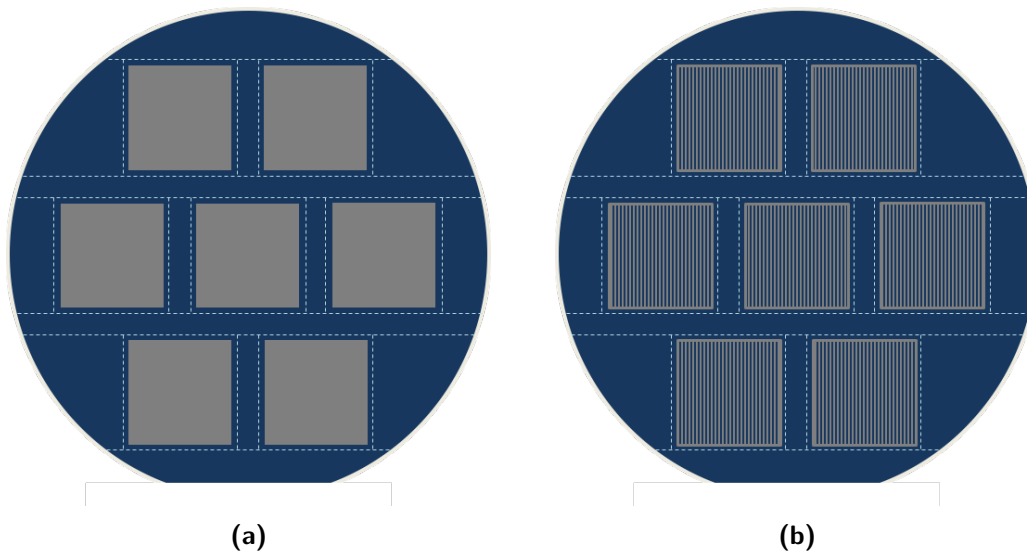


Figure 3.8: Top view of the prepared 4-inch wafers: (a) $2 \times 2 \text{ cm}^2$ metal pads evaporated with shadow-mask for resistance measurements and (b) $2 \times 2 \text{ cm}^2$ metal grids for DLIT probes. The colour blue represents the top ITO layer. The dashed lines indicate the cutting lines.

For the top contact of the references samples (Figure 3.6a) and for the samples intended for resistance measurements (Figure 3.6b), two different routes were adopted: some wafers have been covered with the exactly same full-area metal stack as the bottom side, some other, instead, with the same metal stack but using a seven pads shadow mask of $2 \times 2 \text{ cm}^2$ area per each pad, as shown in Figure 3.8a.

The top contact of samples intended for DLIT probe is replaced with $2 \times 2 \text{ cm}^2$ metal grid (see Figure 3.8b) composed of 50 nm titanium, 50 nm of palladium and 2000 nm of silver deposited by photolithography. The grid fingers have width of $30 \mu\text{m}$ spaced of $800 \mu\text{m}$.

3.2.1 Dicing methods

To properly measure the resistivity of the samples, it is required to define the area of the current flow. To achieve this, for every structure described above, the 4-inch wafers, or half-wafers, were cut in square pieces with area of $2 \times 2 \text{ cm}^2$ – even those with a top full-area metal contact – through laser cut or using an Automatic Dicing Saw DAD 3350 from Disco. In a preliminary experiment, a group of wafers was diced with a partial engraving (e.g. $150 \mu\text{m}$ deep for the dicing saw) from the top or from the bottom, with both the techniques, followed then by a mechanical breaking to divide the single samples. A second group of wafers with full-area metal contact was completely cut through by laser, without requiring a subsequent mechanical breaking. As we will see in Chapter 4, the experiment showed that there is no significant difference between partial engraving performed either with laser or dicing saw, while a complete cut produced significant shunts. Therefore, the option of partial engraving with dicing saw was adopted for all the next samples.

3.3 Perovskite solar cell preparation

Four groups of perovskite solar cells were prepared using the mesoporous structure shown in Figure 2.5b. One group of cells was prepared using a fluorine-doped oxide (FTO) glass substrate, which plays also the role of back contact, coated with 20 nm thick TiO_2 films deposited by EPBVD, acting as electron transport layer. On top of the compact TiO_2 layer, a mesoporous TiO_2 scaffold was spin coated and subjected to UV curing. Therefore, the perovskite absorber, consisting in $\text{CH}_3\text{NH}_3\text{PbI}_3$ (methylammonium lead triiodide or MAPbI_3), was deposited on the mesoporous layer by spin coating. 2,2',7,7'-Tetrakis[N,N-di(4-methoxyphenyl)amino]-9,9'-spirobifluorene (spiro-MeOTAD) was used as hole transport layer (HTL). Finally, the metal contacts were realised by gold evaporation. For a detailed description of the perovskite solar cells preparation refer to ref [37]. This kind of structure is a good candidate to become a standard for PSC at Fraunhofer ISE and thus, this group of cells was used as reference.

Three more groups of cells were prepared coating on a glass substrate 606 nm thick indium tin oxide (ITO) layer using an oxygen flow of 0.3 sccm, with a resulting sheet resistance of around $7 \Omega/\text{sq}$, which is a comparable value to FTO sheet resistance, to improve the lateral conductivity. Then a second 20 nm thick ITO layer was coated on top of it using an oxygen flow of 0.7 sccm to have the same layer of the samples used for resistance measurements. For these three groups of cells, differently processed 20 nm thick TiO_2 films deposited by EBPVD, T-ALD and PE-ALD were used as ETL. For the TiO_2 film deposition refer to Section 3.1 and for ITO deposition to Section 3.2. Then, the mesoporous TiO_2 scaffold, the perovskite absorber, the HTL and gold contacts have been processed identically as for the reference cell with FTO.

3.4 Characterisation

3.4.1 Resistance measurements

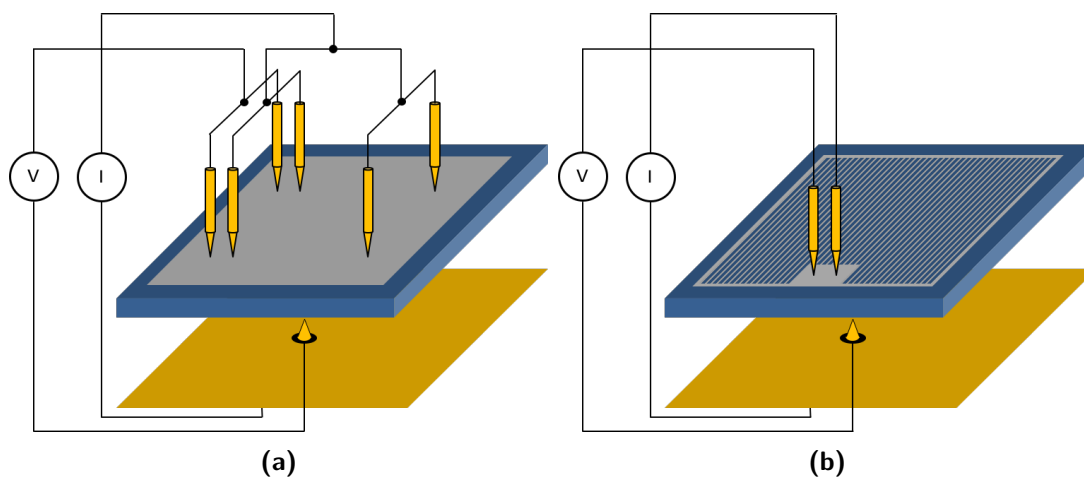


Figure 3.9: Sketch of four-point probe resistance measurements setup and electrical connections for (a) regular pad samples and (b) samples with grid metal contact for DLIT. The blue and grey colours represent the metal-coated samples. The back vacuum chuck and the connection needles are coloured in yellow.

The perpendicular resistance of every sample was measured with a custom four-point probe setup as shown in Figure 3.9. Samples with full-metal area top contact were measured with two voltage needles, around one centimetre spaced, and four current needles with the same spacing (Figure 3.9a). This four current needles configuration was chosen to guarantee a better current flow distribution over the entire volume, rather than through a narrow spatial line. The presence of only two voltage needles is justified by the very high conductivity of the top $1\ \mu\text{m}$ silver layer, which guarantees a perfect equipotential surface. The rear of the samples is contacted by a conductive vacuum chuck as current electrode and a single needle as voltage electrode. A slightly different solution was adopted for samples with the metal grid as top contact: as illustrated in Figure 3.9b, the same back electrodes were used, while a single needles pair for current and voltage is brought in contact directly to the grid contact pin.

In both cases, the resistance was measured using a Keithley 2651A source meter, scanning the current–voltage characteristic. Each measurement was conducted via a forward scan from zero voltage to a positive voltage, and a reverse scan from zero voltage to a negative voltage. The upper and lower voltages were adjusted according to the resistance of the sample always keeping a current limit of $150\ \text{mA}$ to prevent damages or modification of the films. The final resistance values were calculated as linear fit in a current density range between $15\ \text{mA}/\text{cm}^2$ and $30\ \text{mA}/\text{cm}^2$ to simulate the working condition of

a real perovskite solar cell, which current density lies ideally in the range of 20 mA/cm^2 . As already mentioned, all measurements were conducted on as-deposited samples and after thermal annealing on a hotplate (in ambient air) at different temperatures and for different annealing times.

3.4.2 Spectroscopic Ellipsometry

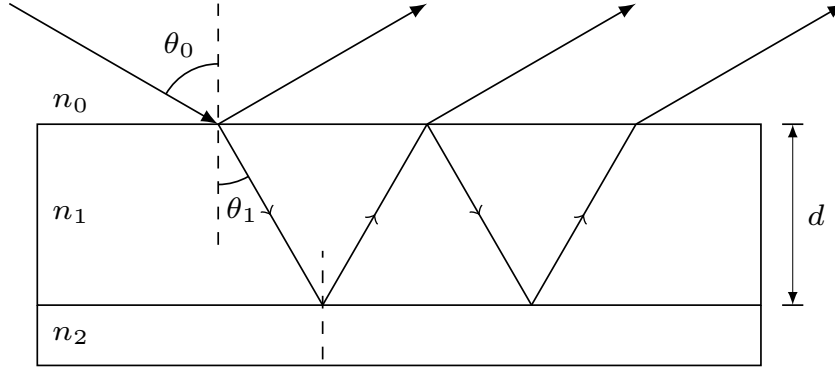


Figure 3.10: Sketch of the interference phenomenon for ellipsometry thickness measurement. The polarised light is reflected at the angle θ_0 at the surface, n_0 is the refractive index of the air, n_1 the refractive index of the film to analyse and n_2 is the refractive index of the substrate.

To measure the thickness of TiO_2 thin films spectroscopic ellipsometry was used. A monochromatic and polarised light with wavelength λ and known s- and p-polarisation components is sent to the surface of the sample subtending an angle close to the Brewster angle. This permits to maximise the information carried by the reflected light when measured at different angles close to the Brewster angle, since a slightly difference in this region results in a signal difference significantly higher than at other angles far from the Brewster angle. The polarisation components of the incident light are then modified during reflection at the surface, which can be analysed according to the following complex ratio expression

$$\rho = \frac{r_p(\lambda)}{r_s(\lambda)} = \tan(\Psi(\lambda)) e^{i\Delta(\lambda)} \quad (3.4.2.1)$$

where r_p and r_s are the complex reflected polarisation components, Ψ is the amplitude ratio and Δ is the phase shifts of the two components [60, 61]. The thickness d is calculated according to [62]

$$d = \frac{\lambda}{4\pi n_1 \cos \theta_1} \Delta \quad (3.4.2.2)$$

where n_1 is the refraction index of the film to analyse and θ_1 is the angle of the refracted ray inside the film, as displayed in Figure 3.10. The refractive index is performed recording a spectroscopic scan in λ and fitted using approximated model.

In this work a M-2000F ellipsometer system from J.A. Woollam Co. was used to record the spectroscopic scan and the evaluations were made with the CompleteEASE Software tool from the same company, using the so-called Cauchy-model described by the expression

$$n(\lambda) = A + \frac{B}{\lambda^2} + \frac{C}{\lambda^4} \quad (3.4.2.3)$$

where n is the real part of the refractive index and A , B and C are fit parameters [60, 61].

Since the Cauchy model is suitable only for not absorbing materials and to keep the spectroscopic ellipsometry analysis as simple as possible, a piece of clean silicon wafer was coated with TiO_2 together with the substrates for thickness control. The measurements were performed at 65° , 70° and 75° around the Brewster angle of TiO_2 of 69.1° , in order to increase the measured information and thus, to reduce the error. The fit was restricted in a wavelength range between 400 nm to 1000 nm to avoid the absorption of TiO_2 that is present for wavelength lower than approximately 350 nm [63] and absorption of silicon for wavelength below approximately 400 nm [64].

3.4.3 X-ray diffraction (XRD)

X-ray diffraction (XRD) is a well established technique to investigate the crystalline structure of powders or thin films, identifying single or poly crystalline phases.

The concept behind XRD is given by the usual phenomenon of Bragg diffraction, for which an incident radiation is scattered by a diffraction grating when the wavelength of incoming photons is in the same range of the slits spacing of the grid. In the case of crystalline materials, the diffraction grating is ideally replaced with the set of crystal planes and, since the planar spacing is in the order of angstroms, the wavelength of the incident radiation must be in the range of X-rays to be scattered. Because each crystalline material has a different structure, the reflected radiation forms a diffraction pattern with unique interference peaks, which represent the signature of the material itself making it identifiable. To perform XRD, several different techniques are available, nevertheless diffractometers with $\theta - 2\theta$ configuration are often used for thin films. In these devices, the X-ray source is typically an X-ray tube with a metallic anode with the K_α components well-known, and the reflected light is recorded by a semiconductor detector. In the $\theta - 2\theta$ configuration the sample is rotated of an angle θ in respect of the X-ray source, while the detector moves along a circular path with an angle 2θ in respect of the source. In this way, an angle θ is always subtended between the sample and the detector [65–67].

To identify any eventual crystal phases in TiO_2 films, XRD measurements were recorded by a diffractometer X'Pert MRD system from Philips, equipped with a copper anode X-ray source with components $K_{\alpha_1} = 1.541 \text{ \AA}$ and $K_{\alpha_2} = 1.544 \text{ \AA}$. The tube current was of 35 A and the accelerating voltage 45 kV. The scans were performed within

the range of angles 2θ between 20° and 70° with steps of 0.075° and integration for 1 second per each step.

3.4.4 X-ray Photoelectron Spectroscopy (XPS)

X-ray photoelectron spectroscopy is a technique that permits to identify the chemical composition, stoichiometry and binding states of compounds within few nanometers from the surface. A monochromatic X-ray beam is sent towards the sample exciting an electron in a particular orbital, corresponding to a certain binding energy. When the excitation energy is high enough the electron can escape from the surface and an electron energy analyser measures its kinetic energy. Therefore, the binding energy results to be the difference between the energy of the X-ray photons and the measured energy of the electron.

The measurements were conducted at the Institut für Mikrosystemtechnik – IMTEK of Freiburg University with a XPS PHI 5600 ESCA System from Perkin Elmer, using a X-ray source with standard Mg anode and photon energy of 1253.6 eV. The anode power was 300 W and the X-ray voltage 13 kV. The lateral resolution is within an area of 200 μm diameter and the depth sensitivity is around 3 nm – 10 nm. For every measured sample, the structure was the usual shown in Figure 3.6b but with the TiO_2 directly exposed i.e., without the top metal contact and upper ITO layer.

For each samples a survey spectra scan was performed before sputtering to identify all elements present and a second one was performed after 15 s sputtering with argon to remove any eventual contamination on the sample surface, in particular carbon from the atmosphere. Then, a detail scan was executed around the titanium 2p orbital and oxygen 1s to evaluate the stoichiometry composition of the TiO_2 films. Refer to Table 3.2 for all XPS setup parameters. The concentrations reported in Table 4.2 were evaluated at IMTEK using the software MultiPak from Ulvac-phi. Per each atomic orbital specific to one element, a Relative Sensitive Factor (RSF) is used to calculate the relative atomic concentration according to the formula

$$C_x = \frac{\text{Peak area}}{\text{RSF}} \quad (3.4.4.1)$$

where C_x is the relative concentration of the element x , and RSF depends on several factors, such the electron cross section, the inelastic electron mean-free path, the area analysed and more. A more accurate RSF factor, denoted as Corrected-RSF, is provided by the manufacturer and it takes into account parameter such as X-ray flux, the detector efficiency, symmetry corrector factor and others.

Table 3.3: Summary table of XPS setup. For each sample a survey scan was performed before and argon sputtering, then a detail survey scan was conducted around Ti_{2p} and O_{1s} orbitals.

XPS measurement	Parameter	Value
Survey scan	Energy region	1200 – 0 eV
	Pass energy	187.85 eV
	Step energy	0.800 eV
	Step time	20 ms
	Sputter time	15 s
	Sputter area	2 mm × 2 mm
Detail scan	Pass energy	23.50 eV
	Step energy	0.025 eV
	Step time	100 ms

3.4.5 Dark Lock-In Thermography (DLIT)

Dark lock-in thermography is a technique widely used in many different applications to investigate the thermal emission of different objects. In particular, in photovoltaic applications, it is very useful to study the heat distribution of a solar cell or thin films. The principle behind the DLIT applied to thin films, is to supply a bias voltage to the sample and detect with an infrared (IR) camera the heat emitted. Shunts in the film consist in less resistive paths where current flows more easily producing higher local heat emissions and thus, they can be identified through a thermography image.

The DLIT is one branch of the more general lock-in thermography (LIT) technique often used in solar cell characterisation. This technique is based on the lock-in principle to extract very small signals from a rather noisy background. It consists in averaging a periodic signal $F(t)$ affected from noise and multiplied by a periodic reference signal $K(t)$ on a time interval t_{int}

$$S = \frac{1}{t_{\text{int}}} \int_0^{t_{\text{int}}} F(t)K(t). \quad (3.4.5.1)$$

Therefore, choosing opportunely the period of the reference signal $K(t)$, it is possible to suppress the continuous component (DC) of the original signal $F(t)$ corresponding to the noise [68, 69]. In DLIT, the periodic signal consists in a square-wave voltage applied to the sample to generate a periodic thermal-wave signal captured by an infrared camera. Using a square-wave with 50% duty cycle, the electrical power of the sample is $P_{\text{el}} = \Delta I \Delta V / 2$ and the temperature variation is given by [70]

$$T(t_1) - T(t_0) = \delta T = \frac{\delta Q}{c \cdot m} = \frac{1}{c \cdot m} \int_{t_0}^{t_{\text{lock-in}}/2} P_{\text{el}}(t) dt = \frac{\Delta I \Delta V}{2 \cdot c \cdot m}, \quad (3.4.5.2)$$

where T is the temperature, Q the heat, c specific heat capacity, m the mass and $t_{\text{lock-in}}$ the time of the complete lock-in period. Since a sample consists in a stack of multiple

layers, each one with a different not known heat capacity, solving the above equation can be very demanding and usually it is simplified to $\Delta T \sim P_{\text{el}}$ [70].

During one lock-in period, the camera acquires a certain number of frames each of which is multiplied by two correlation function (generally sine and cosine) producing two new images with suppressed noise. Because sine and cosine functions are phase shifted of 90° , commonly images correlated with the first one are named *in phase images* S_0 while images correlated with the second one are called -90° *phase shifted images* S_{-90} . Combining these new types of images it is possible to obtain two more new images: the amplitude-image A and the phase-image Φ described by [69]

$$A = \sqrt{S_0^2 + S_{-90}^2}, \quad \Phi = \arctan\left(-\frac{S_{-90}}{S_0}\right). \quad (3.4.5.3)$$

The aim of DLIT applied to the samples used in this work, is first to identify local inhomogeneity in the current transport i.e., to characterise the current distribution over the whole films and in particular pinholes produced during the dicing at the edges or eventually during the film depositions. Pinholes could potentially bear the risk of shunting the top and bottom ITO films within the ITO/TiO₂/ITO sandwich structure degrading the properties of electron transport layer of TiO₂. The idea behind this characterisation is that, in regions with low resistance (compared to the general bulk resistance of the sample), a higher current is flowing and thus shunts are distinguishable as hot spots over the sample surface. Therefore, the DLIT analysis provides a quantitative estimation of the heat flux emitted by the shunts and thus, the power dissipated by them.

In this work a custom DLIT system setup was used, equipped with a Millennium 327k SM camera from IRCAM GmbH and source meter from Toellner Electronic Instruments GmbH. The voltage supplied to each sample was chosen as function of its resistance. All the images presented in Section 4.5 are amplitude-images with power emission calibrated on an area of 4 cm².

Chapter 4

Experimental Results

In this chapter, all the results obtained are presented and discussed. The main goal is to characterise the series resistance of the ITO/TiO₂/ITO stack before and after thermal treatment. As it will be shown, a thermal annealing affects significantly the conduction properties of these structures. The results are then discussed with the aim of finding a correlation between the electrical properties, the chemical composition or the crystalline structure. The chapter ends with the illustration of the results of perovskite solar cells realised with TiO₂ deposited on ITO.

4.1 General Structure Analysis

To properly characterise the series resistance of the samples, they must have a defined area to avoid a lateral current spreading far from the metal contacts which could potentially lead to wrong measurements. Therefore, it was necessary to dice all the samples and identify the best dicing methods. In this section, the series resistance of similar samples diced differently is shown and discussed with DLIT images to study the effect of the dicing at the edges.

4.1.1 Overview Resistance Investigation

As preliminary experiment, the series resistance of samples with 20 nm thick TiO₂ films deposited by EBPVD and PE-ALD was compared after the different types of cutting displayed in Figure 4.1. Samples prepared replacing the TiO₂ with insulating 20 nm thick Al₂O₃ deposited by PE-ALD were used to identify the presence of possible limitations due to the cuts and samples without ETL were used as reference.

Samples prepared with TiO₂ deposited by EBPVD, T-ALD and reference samples, with a front (or top) metal-pad contacts (Figure 3.6b), were diced using both a laser

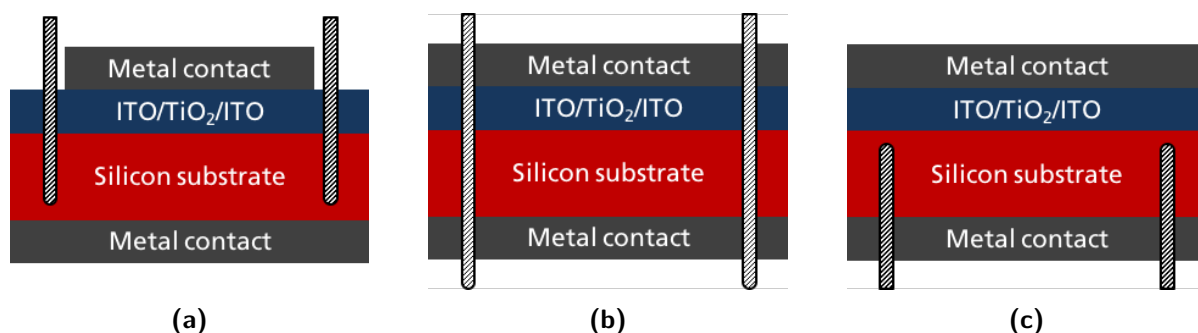


Figure 4.1: Sketch of the different types of sample dicing techniques used: (a) partial engraving by laser or dicing saw from the top metal-pad contact evaporated with a shadow-mask; (b) complete laser cut through the wafer from the top full-metal contact; (c) partial engraving with dicing saw from the bottom, with top full-area metal contact.

cut and the dicing saw 150 μm deep from the front side (Figure 4.1a). Samples prepared with Al_2O_3 with metal-pad contacts were diced with laser and dicing saw 150 μm in deep from the front, while samples with the same film but top full-area metal contact were diced from the rear with dicing saw (Figure 4.1c) and with laser completely through the wafer from the front side (Figure 4.1b).

Figure 4.2 shows the resistance results calculated as the inverse of the slope of the recorded J - V curves. In particular, two resistance values were calculated for each sample according to the voltage scan direction: a forward scan was performed from 0 V to $+V$ and a reverse scan was performed from 0 V to $-V$, where the $\pm V$ voltages were chosen according to the resistance of the samples, keeping the current below 40 mA/cm^2 . For samples with TiO_2 processed with EBPVD it was used a voltage range from 0 V to 0.02 V for the forward scan and from 0 V to -0.02 V for the reverse scan; for samples with TiO_2 processed with PE-ALD 0 V to 0.5 V for forward and 0 V to -0.5 V for reverse scan; for samples with Al_2O_3 processed with PE-ALD it was used 0 V to 0.4 V for forward and 0 V to -0.4 V for reverse scans and for reference samples it was a range from 0 mV to 2 mV and from 0 mV to -2 mV for forward and reverse scan respectively.

The reference samples exhibited a series resistance of approximately $0.027 \Omega \text{cm}^2$, which corresponds mainly to the resistance of 200 μm thick silicon wafer ($R_s = 0.02 \Omega \text{cm}^2$ for a resistivity of $1 \Omega \text{cm}$) plus tiny contributions of the other layers and interfaces. This clearly proves the very high conductivity of ITO and this value was also the lowest resistance value possible to measure.

The results also show that no significant difference is present between samples partially diced by laser cut or dicing saw, in both cases of top full-area metal contacts or metal-pad contacts evaporated with a shadow-mask, independently on the cut side. Contrariwise, Al_2O_3 samples extracted from wafers by a full-metal area diced with a laser cut completely through the wafers were strongly affected by shunts, probably generated by the cutting itself. Because of the equivalence between the partial laser cut and the

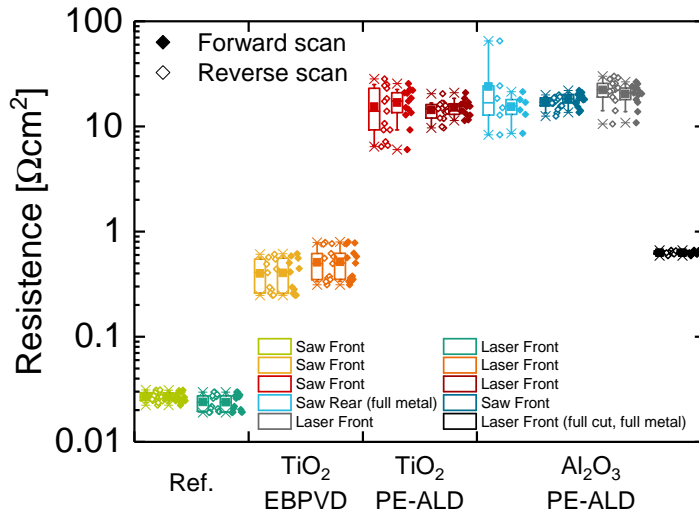


Figure 4.2: Resistance measurements results after different dicing methods of differently processed samples: TiO_2 deposited via EBPVD and PE-ALD, Al_2O_3 deposited via PE-ALD and reference samples without ETL. Two groups of samples with Al_2O_3 were fabricated with a front full-area metal contact, all the others samples were fabricated with front metal-pad contacts evaporated using a shadow-mask.

partial mechanical cut with the dicing saw, both performed from the front side of wafers with metal pads, the partial engraving with the dicing saw on wafers with metal pads was chosen for convenience for all other samples used in this work.

Notably is the difference between samples with TiO_2 films prepared with EBPVD and PE-ALD: the first group has an average resistance of around $0.4 \Omega \text{cm}^2$ while the second group of around $11 \Omega \text{cm}^2$. Surprisingly, samples with insulating Al_2O_3 presented a resistance in the same range of those with TiO_2 deposited via PE-ALD. This could suggest that shunts produced either during the film deposition or during the dicing prevented to measure higher values of the resistance and thus, also TiO_2 deposited by PE-ALD could be less conductive than what was measured.

Let us mention that all the samples used for this experiment were processed without the rear side ITO contact shown in Figure 3.6b. However, the results of the reference samples, which demonstrated the low resistivity of the ITO layers, led to the decision of using the additional rear side ITO to simplify the fabrication processes of the samples considerably.

4.1.2 Analysis of shunt at the edges

To investigate more in detail the effect of the shunts potentially produced during the dicing, DLIT images of grid-metal samples (Figure 3.6c) with TiO_2 films deposited through T-ALD and PE-ALD were recorded, applying two different thicknesses for the latter. The use of the metal-grid was necessary to study the heat emitted directly by the ITO/ TiO_2 /ITO stack, which otherwise would have been drastically reduced by the top full metal-pad. In parallel to these samples, a second group of samples was prepared with the same TiO_2 films but with metal-pad contacts to compare the resistance with samples provided of metal-grid.

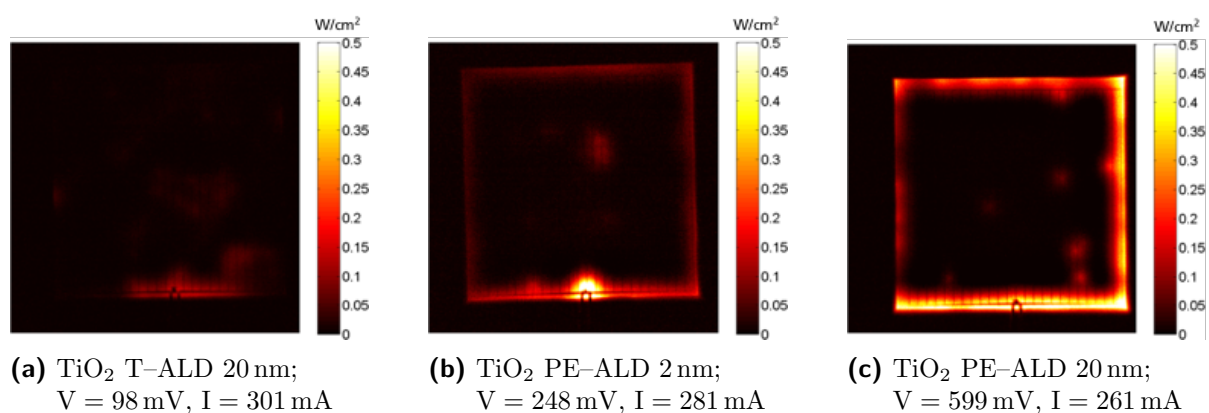


Figure 4.3: DLIT investigation of three samples with different TiO_2 films prepared with a top grid-metal contact as shown in Figure 3.6c. The voltage biases were chosen to generate roughly the same total current. For similar total current flowing through the sample, brighter areas indicate a higher local current flow due to low resistive paths.

In Figure 4.3, DLIT images of three exemplary samples subjected to approximately the same current are shown, while Figure 4.4 shows the resistance of the two groups of samples with grid and pad contacts. Considering their series resistance, the samples with TiO_2 films obtained by PE-ALD, which showed a higher resistance compared to T-ALD, were more sensitive to shunts generated at the edges, as indicated by brighter areas of Figure 4.3b and Figure 4.3c. These bright areas indicate that a higher local current is flowing compared to the total current flowing through the whole area of the samples, dissipating power in form of heat and thus, a low resistance is present there.

Let us notice that the resistance of samples with metal-grid contacts prepared with 20 nm T-ALD TiO_2 and 2 nm PE-ALD TiO_2 shown in Figure 4.4 was in the same order. But comparing the resistance of samples with the same TiO_2 films with metal-grid contacts to samples with pad contacts, it is possible to see a difference of around $0.9 \Omega \text{cm}^2 - 1.0 \Omega \text{cm}^2$. In fact, it was calculated that only the metal-grid contributes to the series resistance adding roughly $\sim 0.8 \Omega \text{cm}^2$ (estimated using gridSim [71]) which represents a lowest limit of the resistance measurable for this structure.

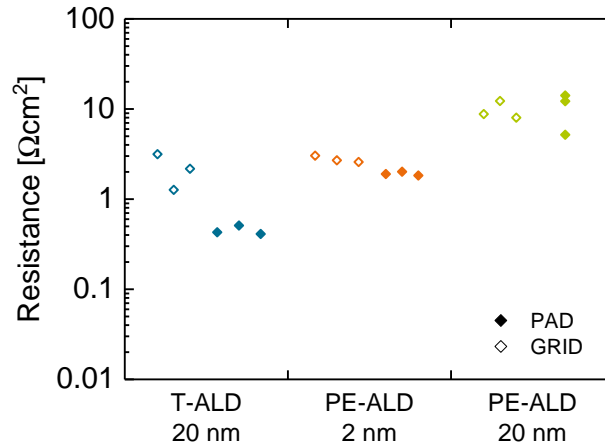


Figure 4.4: Resistance results of samples provided with top grid-metal contact used for the DLIT investigation showed in Figure 4.24 and samples provided with top pad-metal contact. These samples were used as references for samples with metal-grid.

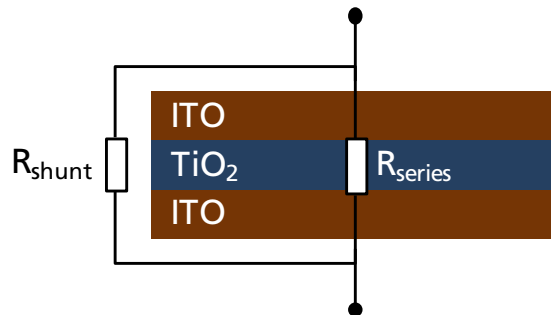


Figure 4.5: Electrical scheme of the series resistance R_{series} due to the TiO_2 film and the interfaces with ITO and the shunt resistance R_{shunt} due to the dicing connected in parallel.

All this consideration could confirm what was already supposed in Section 4.1.1: shunts are created at the samples edges by the dicing, but it seems to have a significant influence on the measured resistance only if a high resistance is present in the ETL i.e., TiO_2 processed with PE-ALD. As shown in Figure 4.5, we can simplify the ITO/ TiO_2 /ITO stack with two resistors connected in parallel: a series resistor with resistance R_{series} , due to the TiO_2 film electrical properties and the contact resistance at the interfaces with ITO, and a shunt resistor with resistance R_{shunt} due to the dicing of the samples (plus eventual shunts in the TiO_2 film). It is clear that current will flow along the path with minor resistance. Therefore, when $R_{series} \gg R_{shunt}$, the shunt resistance becomes the limiting factor.

Nevertheless, this limitation in the measurement of R_{series} is not too problematic for

the scope of this work, since values above $10 \Omega \text{ cm}^2$ are completely not suitable for tandem solar cell applications, as it would result in a huge power loss (compare Figure 1.3).

4.2 Resistance results

In this section, all the results of the resistance measurements are reported in a detailed analysis of each TiO_2 film deposition technique as a function of the TiO_2 thickness. For all of them, thermal annealing experiments were conducted to study the effect of thermal treatments. Therefore, a general comparison between samples with 20 nm thick TiO_2 films is presented as-deposited and after thermal annealing. All the results reported in the following sections are extracted from samples with the structure shown in Figure 3.6b with top metal contact deposited by shadow-mask and diced by dicing saw from the top, unless otherwise specified. The label “reference” always means the structure showed in Figure 3.6a, with the same top metal contact and diced in the same way as for regular samples.

4.2.1 Plasma Enhanced ALD

To calculate the resistance of the samples, forward (from 0 V to +V) and reverse (from 0 V to -V) voltage scans were recorded and the two resistance values were calculated as the inverse of the slope of the two obtained J - V curves. It was observed that, when the scans were performed within a *small* range (roughly from -0.5 V to 0.5 V), the behaviour of the samples was ohmic. However, exceeding these values, both in the positive and negative direction, the samples stopped to be ohmic and a diode-like J - V curve was observed.

In Figure 4.6, J - V characteristics of samples with 20 nm thick TiO_2 films grown with PE-ALD are shown. Figure 4.6a shows the voltage scans performed to calculate the resistance as the inverse of the fitted slope, from 0 V to 0.7 V (forward) and from 0 V to -0.7 V (reverse). These voltage biases were chosen to keep the current below 40 mA/cm^2 and a not ohmic behaviour was observed. Figure 4.6b shows voltage scans performed from -0.5 V to 0.5 V and a from 0.5 V to -0.5 V. In this case, the samples behaved perfectly as an ohmic conductor. In Figure 4.6c, hysteresis effect is shown after repeating several times scans from 0 V to 2 V, then from 2 V to -2 V and from -2 V to 0 V. After each scan the resistance slightly decreased toward a kind of saturation curve. Figure 4.6d shows the same effect repeating a voltage scan from -2 V to 2 V and from 2 V to -2 V.

Figure 4.6c and Figure 4.6d clearly show a decrease of the resistance when the voltage scans are repeated several times within a range between -2 V and 2 V; in particular, it seems that a sort of threshold for this effect is present around roughly 1 V and -1 V in the positive and negative directions, respectively. A similar effect, called *resistance*

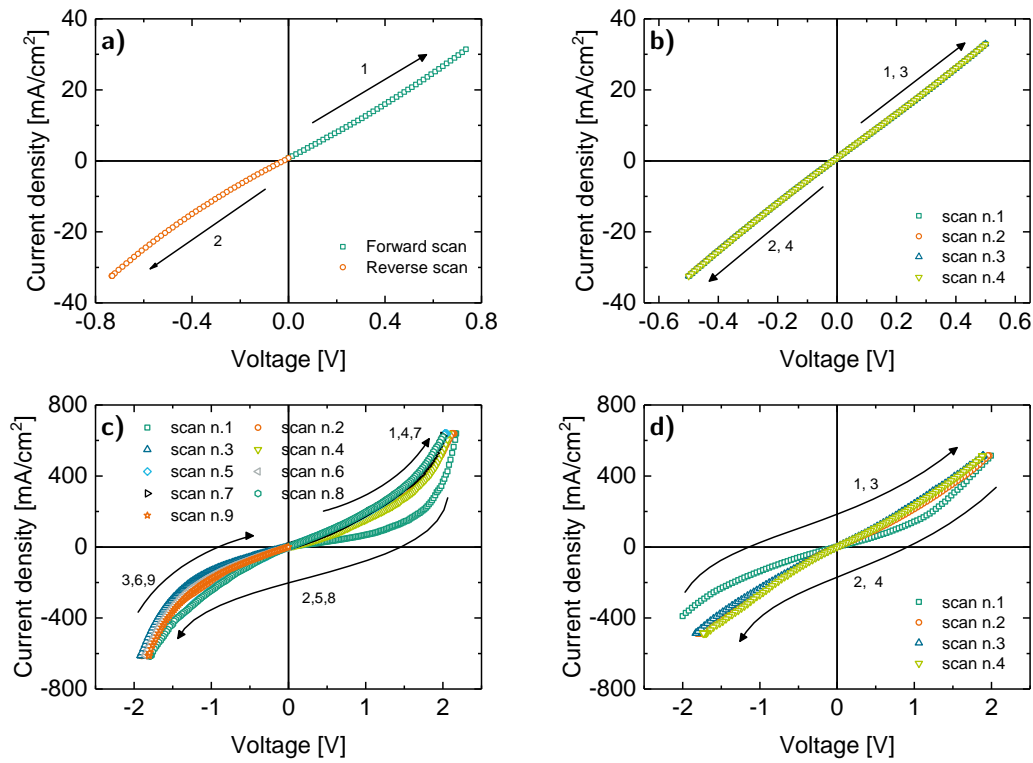


Figure 4.6: Current–Voltage characteristic of samples with 20 nm thick TiO₂ film recorded with different voltage scans: (a) 0 V to 0.7 V (forward) and 0 V to -0.7 V (reverse) scans used to calculate the total series resistance; (b) scan from -0.5 V to 0.5 V and from 0.5 V to -0.5 V; (c) scan from 0 V to 2 V, from 2 V to -2 V and from -2 V to 0 V; (d) scan from -2 V to 2 V and 2 V to -2 V.

switching has been reported for a similar ITO/TiO₂/ITO sandwich [72] and for other TiO₂ thin films [73]. The resistance switching effect is a phenomenon for which a material, if subjected to a threshold voltage, can drastically change its resistance state. This new resistance state (*set*) remains constant if the threshold voltage is not exceeded again. When this happens, the material *switches* its resistance back to the old original state (*reset*). The resistance switching materials are classified as *unipolar* when the set and reset threshold voltages coincide in sign, or as *bipolar* when they have opposite sign [72–74]. However, in this work the *reset* of the resistance was not observed and then it is not possible to identify the resistance switching effect. Nevertheless, it has been shown that a threshold voltage is present and after exceeding it the electrical properties and, thus film resistance, are drastically effected. On the other hand, restricting the voltage range by limiting the current to the operational conditions of a PSC (around 20 mA/cm²) and not exceeding roughly 40 mA/cm² in both scan direction, the *J–V* curve (and consequently

the resistance) was not affected by the measurements, as it is shown in Figure 4.6b.

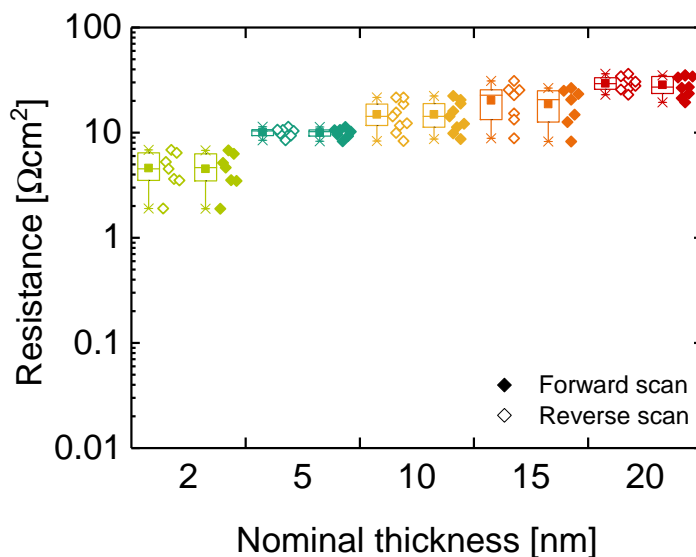


Figure 4.7: Resistance results of samples with different TiO_2 thicknesses processed with PE-ALD calculated fitting the J - V curves recorded in forward (0 V to $+V$) and reverse (0 V to $-V$) directions. The voltage bias was adjusted for each samples to limit the current below 40 mA/cm^2 . For more accurate thickness values refer to Table 3.2.

Figure 4.7 shows the resistance results measured on samples with different TiO_2 thicknesses deposited by PE-ALD. Two resistance values for each samples were obtained fitting the reverse and forward scans shown in Figure 4.6a. A rather strong scattering of the data was present indicating that samples with the same TiO_2 thickness showed different resistance values. For this reason, the bias voltage was adjusted always to not exceed a current of 40 mA/cm^2 thus, for those samples subjected to a voltage higher than 0.5 V (absolute value) in both directions, a slightly non-ohmic behaviour was observed. Nevertheless, also in this cases, the linear fits of the two scan direction always produced identical resistance values and the samples were assumed as ohmic.

It is evident that the resistance increased with increasing the thickness of the film, as expected for an ohmic material. Using the thicknesses listed in Table 3.2, a linear fit of resistance as function of the thickness was calculated to obtain the resistivity of the bulk TiO_2 film and the contact resistance of the ITO/ TiO_2 interface. In particular, from the fit shown in Figure 4.8, the resistivity of the bulk was calculated from the slope and the contact resistance was calculated from half of the intercept. The obtained values are $(13.0 \pm 0.9) \times 10^6\ \Omega\text{ cm}$ for the resistivity of the bulk TiO_2 and $(1.4 \pm 0.5)\ \Omega\text{ cm}^2$ for the contact resistance of the TiO_2 /ITO interface in the as-deposited state. In other studies it has been shown that the TiO_2 resistivity can drastically change according to the deposition technique. For examples, a resistivity of $1.0\ \Omega\text{ cm} - 10.0\ \Omega\text{ cm}$ for magneto-

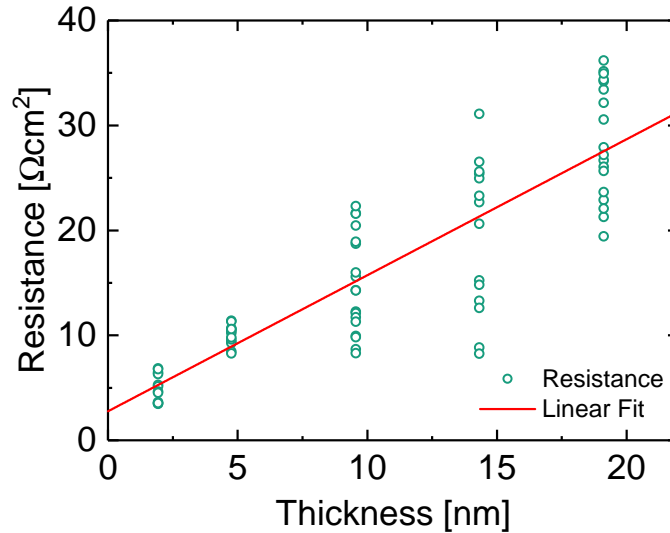


Figure 4.8: Resistance of samples prepared with PE-ALD processed TiO_2 films vs the film thickness listed in Table 3.2. In red is indicated the linear fit used to calculate the resistivity of the TiO_2 and the contact resistance with ITO.

sputtering [75].

The effect of the thermal treatment was investigated annealing the samples in air with steps of 50°C , for 5 min and 55 min per each temperature step starting from 100°C . Since the resistance values resulted to be quite scattered for every TiO_2 thickness, as shown in Figure 4.9, samples with the highest (Figure 4.9a) and lowest resistance values (Figure 4.9b) were chosen for this annealing experiment. For both groups, the resistance of the ITO/ TiO_2 /ITO stack slightly decreased with the annealing temperature and the annealing time until a critical point of 200°C after 60 min was reached. Around this point, the resistance of all samples strongly decreased and reached $0.05 \Omega \text{cm}^2$, independently from the resistance prior the annealing and from the TiO_2 thickness. Interestingly, for samples with 2 nm thick TiO_2 layers, this strong decrease was observed already after 5 min at 200°C . After 1 hour at 200°C , the resistance of all the samples reached its minimum, close to the resistance of the reference samples without TiO_2 layer and then it slightly increased with further annealing at higher temperature. Also the resistance of the reference samples showed an increase after this temperature and this could explain to some extent the similar increase observed for samples with TiO_2 films.

This experiment suggested that the bulk properties of very thin TiO_2 layers deposited by PE-ALD strongly change in the temperature range around 200°C , improving significantly the conductivity of the ITO/ TiO_2 /ITO stack. However, it cannot be excluded that strong modifications of the two interfaces with ITO can also occur. For example, defects and trap states at the interface could have been rearranged after the thermal an-

nealing, as well as ions could migrate creating vacancies at the contact region. Moreover, as it has been shown in Chapter 2, energy barriers are always present at interface of both heterojunctions and metal-semiconductor Schottky junctions and thus it is possible that these energy barriers drastically changed after the thermal treatment above 200 °C.

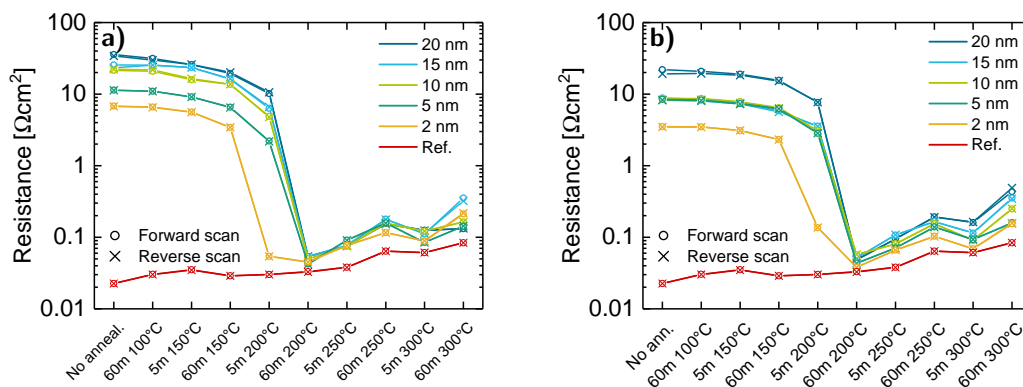


Figure 4.9: Thermal effect on the resistance of samples with TiO₂ films prepared by PE-ALD as function of temperature and annealing time. Two distinct groups were analysed: one set of samples with (a) the highest resistance values and one with (b) the lowest resistance values. The red line indicates the resistance of a reference samples without TiO₂ film.

To study this temperature induced change of the resistance in more detail, a second experiment was performed narrowing the temperature range and the time steps around this critical annealing point. In Figure 4.10 the effect of thermal treatment is reported for every TiO₂ thickness used, keeping each sample at one fixed temperature and incrementing the annealing time on the hotplate. Although there are slight differences for some of the two identical treated samples per variation (TiO₂ thickness and annealing temperature), clear trends as function of the annealing temperature, the annealing time and the TiO₂ thickness can be observed. Annealing at 175 °C resulted only in a slight reduction of the resistance, expect for samples with 2 nm thick TiO₂ layers, where a significant reduction is observed after 30 min of annealing. A very strong reduction of the resistance was observed at 200 °C and 225 °C, reaching a minimum around 0.05 Ωcm^2 for each sample. The annealing time required to reach this minimum was significantly shorter the higher the annealing temperature and the lower the TiO₂ thickness. Note that the samples annealed at 225 °C showed a weak increase of the resistance again at annealing time above roughly 15 min, which is quite similar to the increase of the resistance observed for the reference samples without TiO₂ shown in Figure 4.10f, indicating that this increase is not associated to the TiO₂ bulk resistance or the ITO/TiO₂ interfaces.

In order to separate the bulk from the interface contribution, for each annealing condition, a linear fit of the resistance in function of the thickness of TiO₂ films was performed to calculate the bulk resistivity and the contact resistance due to the TiO₂/ITO

interface. Figure 4.11 shows the corresponding data for the two groups of samples, one composed of high resistive samples ((a)) and one composed of low resistive samples ((b)). Note that the data shown in Figure 4.11a Figure 4.11b are simply different representations of the data displayed in Figure 4.9a and Figure 4.9b, respectively. It is evident that only the group of samples with a high resistance prior annealing (Figure 4.11a) showed a linear trend of the resistance as function of the thickness and the annealing conditions, while the group of with a low resistance as-deposited did not exhibited any linearity (Figure 4.11b). Therefore, the linear fits to calculate the bulk resistivity of TiO_2 and the contact resistance of the ITO/ TiO_2 interface were performed only for the first group. The results obtained from the fit analysis of the high resistance samples are reported in Table 4.1. Although the linear fits were unable to provide very accurate values due the scattered data, it is important to notice that after 1 hour at 200°C the bulk resistivity dropped from the order of $\text{M}\Omega\text{ cm}$ down to $\text{k}\Omega\text{ cm}$ and the contact resistance decreased of two orders of magnitude. This result indicates that the main series resistance contribution of the ITO/ TiO_2 /ITO sandwich processed with PE-ALD is the TiO_2 bulk resistance rather than the contact resistance of the interface and this bulk resistance is strongly reduced during thermal annealing. The contact resistance reduced as well but the bulk has the main influence.

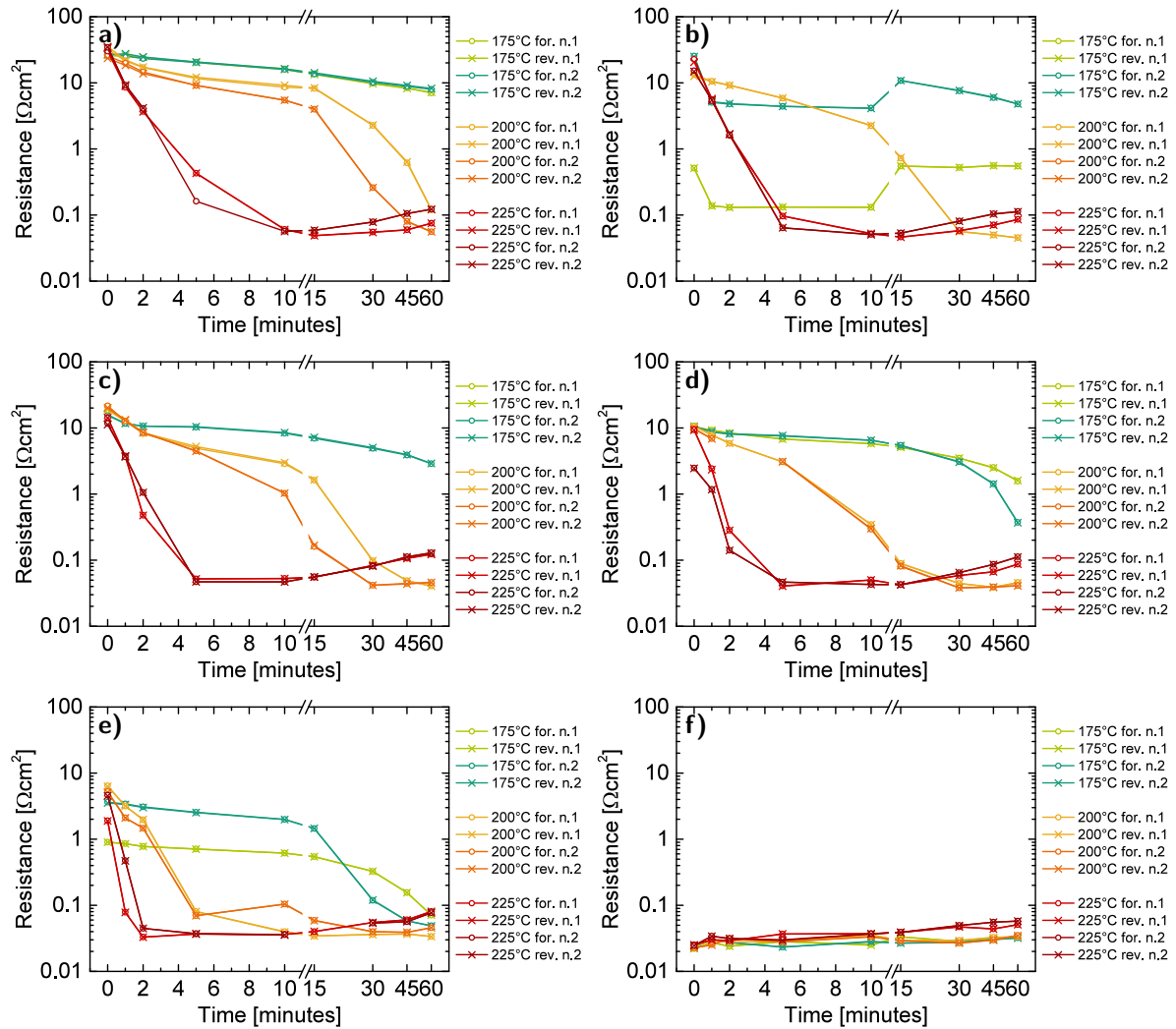


Figure 4.10: Detailed thermal treatment investigation for several different nominal thicknesses of TiO_2 film deposited by PE-ALD: (a) 20 nm; (b) 15 nm; (c) 10 nm; (d) 5 nm; (e) 2 nm; (f) reference samples without TiO_2 . Two samples were used for each thickness and as reference.

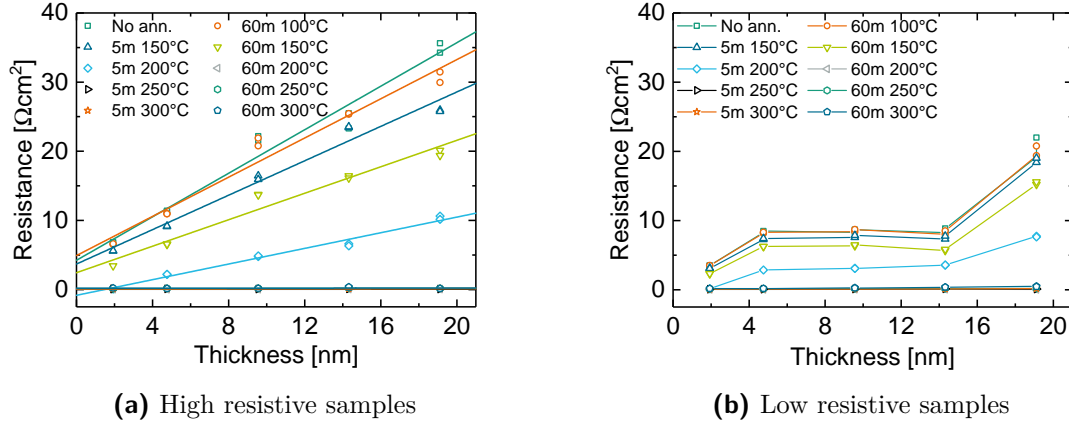


Figure 4.11: Effect of the thermal treatment on the linearity of the resistance as function of the TiO_2 film thickness for (a) high resistive samples and (b) low resistive samples. The displayed data are the same values shown in Figure 4.9.

Table 4.1: Resistivity of TiO_2 films deposited with PE-ALD and contact resistance of the TiO_2/ITO interface as function of the annealing conditions. The results were calculated as the slope and half of the intercept of all linear fits shown in Figure 4.11a. Not physical values obtained from the fits are omitted.

Annealing condition	Resistivity ρ (Ωcm)	R_{contact} (Ωcm^2)
No annealing	$(15.7 \pm 0.9) \times 10^6$	2.1 ± 0.6
60 min 100 °C	$(14.1 \pm 0.9) \times 10^6$	2.5 ± 0.5
5 min 150 °C	$(12.4 \pm 0.7) \times 10^6$	1.9 ± 0.4
55 min 150 °C	$(9.6 \pm 0.6) \times 10^6$	1.2 ± 0.4
5 min 200 °C	$(5.7 \pm 0.2) \times 10^6$	–
55 min 200 °C	$(6.7 \pm 1.0) \times 10^3$	0.0021 ± 0.0005
5 min 250 °C	–	0.042 ± 0.002
55 min 250 °C	$(20 \pm 9) \times 10^3$	0.065 ± 0.005
5 min 300 °C	$(20 \pm 5) \times 10^3$	0.040 ± 0.005
55 min 300 °C	–	1.2 ± 0.4

4.2.2 Thermal ALD

In Figure 4.12 the results of the resistance measured for TiO₂ films grown with T-ALD are shown. Also in this case, two resistance values were measured for each sample as the inverse of the fitted J - V curves recorded with a forward scan from 0 mV to 14 mV and a reverse scan from 0 mV to -14 mV for samples with 20 nm thick TiO₂ layers (Figure 4.13).

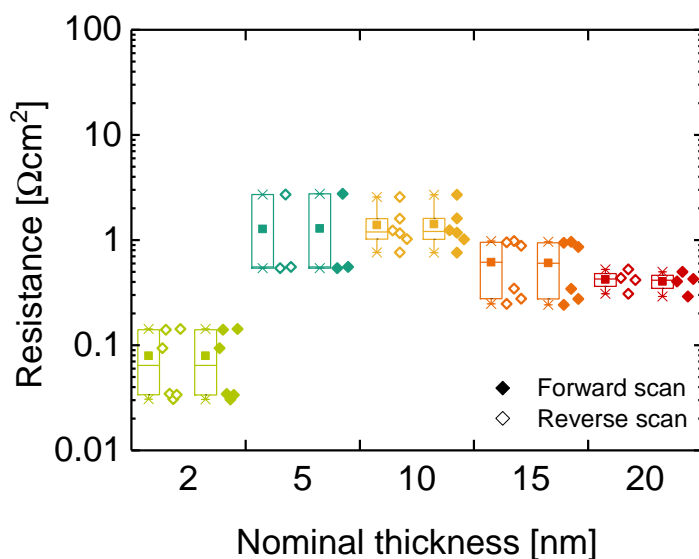


Figure 4.12: Resistance of samples with different TiO₂ thicknesses, grown via T-ALD.

Surprisingly, no linearity of the resistance as function of the thickness was observed, as one would expect from an ohmic material. The lowest resistance values were measured for samples with 2 nm thick TiO₂ films with a mean value around $0.08 \Omega \text{ cm}^2$. The resistance becomes much higher for samples with 5 nm and 10 nm thick TiO₂ films which have a mean resistance of around $1.5 \Omega \text{ cm}^2$. For thicker films, a decrease of the resistance was observed while increasing the TiO₂ thickness. In particular, the measured resistance was around $0.6 \Omega \text{ cm}^2$ and $0.4 \Omega \text{ cm}^2$ for samples with 15 nm and 20 nm thick TiO₂ films, respectively.

These very different results compared to the samples prepared with PE-ALD, could be explained by relating the resistance of the samples to the deposition time required to deposit the TiO₂ films on the first ITO layer. The deposition of 10 nm and 20 nm thick TiO₂ layers via PE-ALD required roughly 50 min and 1 h 40 min, respectively. On the other hand, to deposit TiO₂ films of same thicknesses via T-ALD, the deposition took 3 h 10 min and 6 h 18 min for 10 nm and 20 nm, respectively. During this time, the samples remained in the reactor chamber subjected to a temperature of 200 °C and it is possible that a thermal annealing occurred *in-situ* during the deposition itself. Since

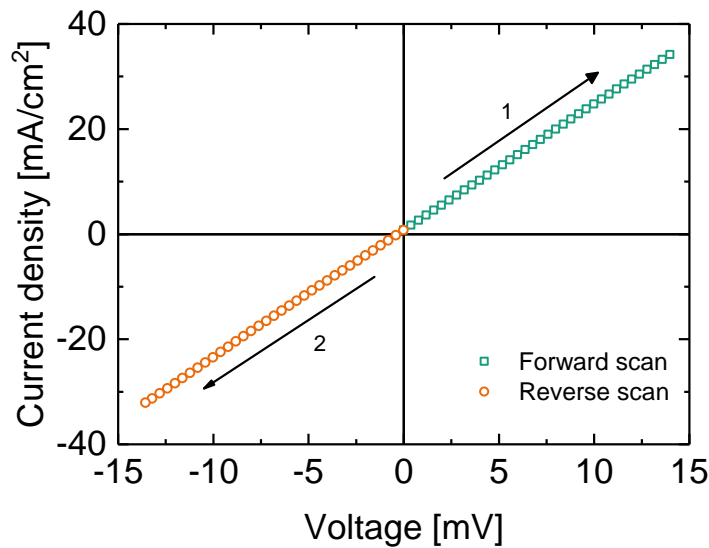


Figure 4.13: Example of J - V characteristic of 20 nm thick TiO_2 film. The arrows indicate the direction of the voltage scans.

the samples processed with T-ALD suffered a much longer exposure at this temperature, it is then possible that a change of the TiO_2 properties occurred during the deposition itself, as well as a modification of the interface between the TiO_2 and the first ITO. Note that the second ITO layer of the stack was deposited at 100°C and with the same deposition time for all the samples and thus, there is no reason to believe that this deposition process could have affected so dramatically the final resistance. Although this is only a speculation, the annealing experiments performed on samples prepared via PE-ALD clearly showed a strong decrease of the resistance when the samples are subjected to a temperature of 200°C for several minutes, corroborating this hypothesis. Since the linearity of the resistance as function of the TiO_2 film thickness was not observed, a linear fit to extract the bulk resistivity and the contact resistance of the interfaces with ITO is meaningless and thus it was not performed.

A second important difference compared to the samples with TiO_2 deposited by PE-ALD, is that all the T-ALD processed samples exhibited a perfect ohmic behaviour without any threshold voltage effects. The reason might be the very low voltage biases applied, in range of millivolts, to not exceed the current of 40 mA/cm^2 . Since this values were far below the threshold voltage observed for PE-ALD (approximately $\pm 0.5\text{ V}$), it is possible that a similar effect can be also observed for samples processed with T-ALD.

Annealing experiments, similar to what described in the previous section, were performed also for samples processed via T-ALD. Figure 4.14 shows the effect of thermal treatment on samples with different TiO_2 thicknesses. For all of them, there was a rather significant increase of the resistance after annealing for 1 hour at 100°C , followed by a

constant decrease after further annealing steps at higher temperatures. Similarly to the samples with TiO₂ films deposited with PE-ALD, also in this case the resistance reached a minimum value after around 1 hour at 200 °C and 5 min at 250 °C, which is significantly lower than the value measured in the as-deposited state. As such, these results indicate that the resistance of the T-ALD TiO₂ and/or its interface with ITO can still be improved by annealing and, similar to PE-ALD, a value below 0.1 Ω cm² is reached after annealing between 1 h at 200 °C and 5 min at 250 °C. Note again that the resistance of the reference samples without TiO₂ slightly increase after further annealing steps at temperatures above 200 °C. We should further note here that after annealing for 60 min at 200 °C, all the samples have roughly a resistance of 0.03 Ω cm², independent of the TiO₂ thickness (i.e. there is no significant slope being present), indicating that the resistance of this ITO/TiO₂/ITO stack (with T-ALD processed TiO₂) is mainly dominated by an interface resistance rather than an TiO₂ bulk resistance.

As it has been just shown, a strong dependence of the resistance of the ITO/TiO₂/ITO stack with the annealing temperature and the annealing time was observed also for samples processed via T-ALD. This aspect corroborates even more the hypothesis of an in-situ annealing during the TiO₂ deposition that can significantly change the current transport properties of the stack.

In a separate batch, a detailed investigation of the thermal treatment was performed on samples with a 20 nm thick TiO₂ film around the crucial temperature of 200 °C. In Figure 4.15a the trend of the resistance is reported for samples subjected to three different temperatures as function of the cumulative annealing time. Also in this case, it is possible to identify an increase of the resistance after just one minute for every used temperature and then a slow decrease with the increasing annealing time was observed. Similar to the annealing results of the samples processed with PE-ALD, resistance minima of around 0.05 Ω cm² and 0.04 Ω cm² were reached after 10 min at 225 °C and after 45 min at 200 °C, respectively.

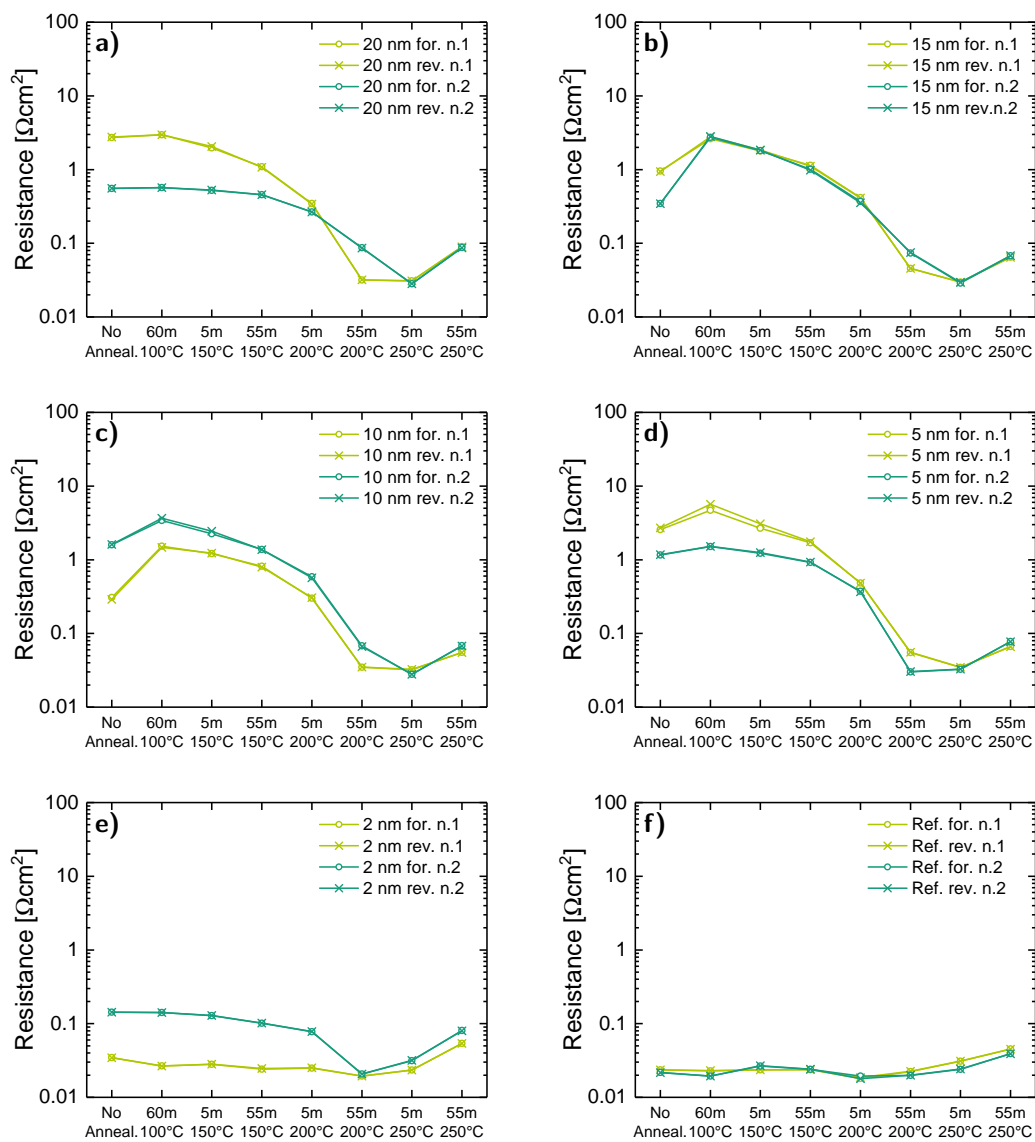


Figure 4.14: Thermal treatment effect on samples with different TiO₂ thicknesses films deposited with T-ALD: (a) 20 nm; (b) 15 nm; (c) 10 nm; (d) 5 nm; (e) 2 nm; (f) reference samples without TiO₂.

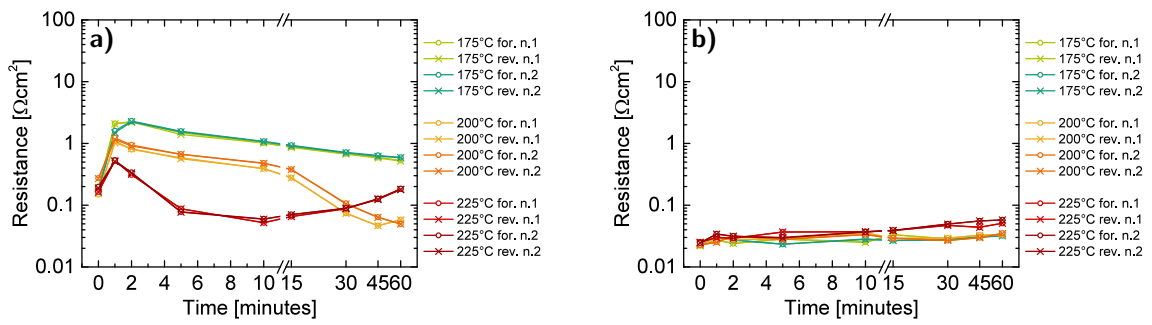


Figure 4.15: (a) detailed analysis of the thermal treatment on 20 nm thick TiO_2 films deposited with T-ALD; (b) reference samples without TiO_2 film.

4.2.3 Electron Beam Physical Vapour Deposition

Also for samples with TiO_2 deposited via EBPVD the resistance of samples with different TiO_2 thicknesses was measured to study the properties of the bulk TiO_2 and of the interfaces with the ITO layers.

Figure 4.16 shows the results of the resistance measurements of samples with different TiO_2 film thicknesses grown through EBPVD in two different batches. The decision to have thicker films compared to the ones grown with ALD was motivated by the less precise control on the film thickness due to the very high deposition rates of 1 nm/s in the used EBPVD tool. Comparing the results of the two batches (batch n.1 and batch n.4), where the samples were processed identically as far it is known, it is clear that a strong inconsistency is present.

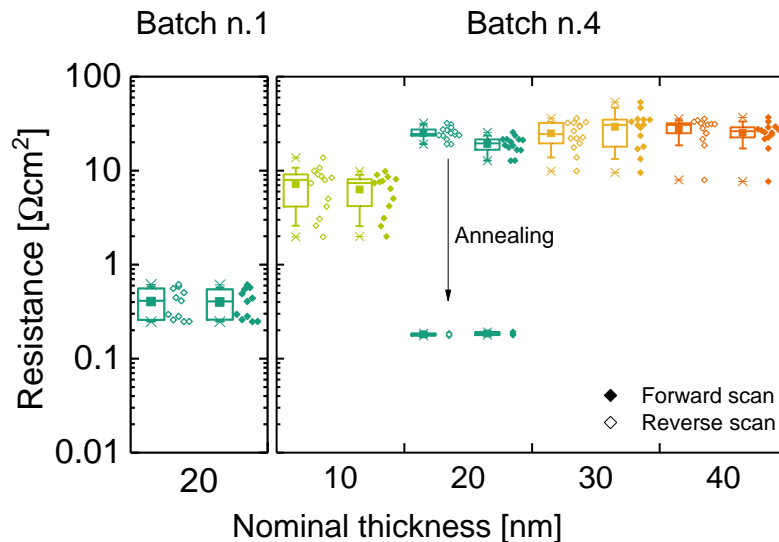


Figure 4.16: Resistance of samples with different TiO_2 films thicknesses grown by EBPVD in two different batches. In the first batch only samples with 20 nm thick TiO_2 film were prepared. The two batches showed completely different results without clear reason. Furthermore, three exemplary samples with 20 nm thick TiO_2 film were annealed at 225 °C for 15 min showing a drastic reduction of the resistance.

In Figure 4.17, one representative J - V curve of the batch n.1 (Figure 4.17a) and one of the batch n.4 (Figure 4.17b) for samples with 20 nm thick TiO_2 are compared. Since the samples fabricated in the batch n.1 showed a very low resistance, a small bias between -20 mV and 20 mV was sufficient to stay in the working region of the current for a PSC (within ± 40 mA/cm²) and a perfect ohmic behaviour was observed for these samples (Figure 4.17a). On the other hand, samples realised in the batch n.4, required a much higher voltage bias to reach the same current. As it can be seen in Figure 4.17b,

above 1 V in the positive direction, the resistance changed drastically and the samples stopped to behave linearly. During a scan in the opposite direction, the slope of the J - V curve had already changed and the non-ohmic behaviour was observed below -0.5 V.

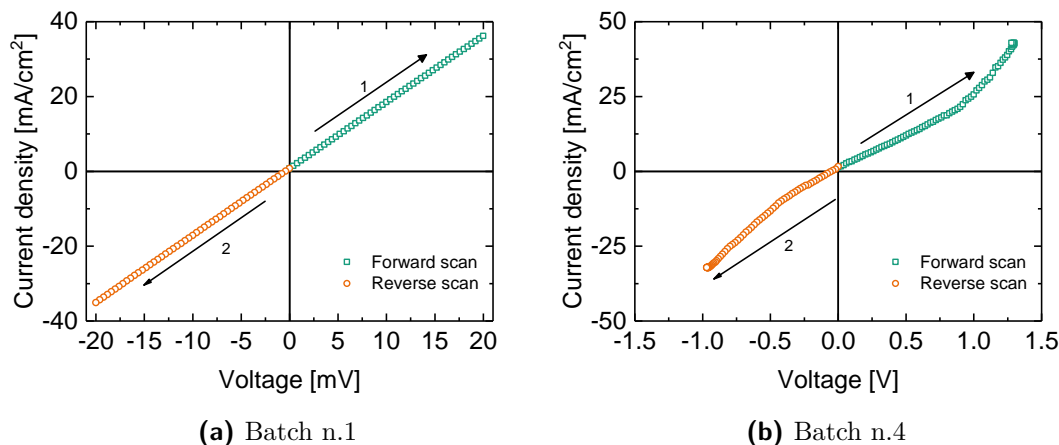


Figure 4.17: J - V characteristics of two samples with 20 nm thick TiO_2 films deposited with EBPVD in two distinct batches. The arrows indicate the direction of the voltage scans.

Figure 4.18 illustrates this hysteresis effect in more detail by showing the results for several voltage sweeps. Similarly to samples with PE-ALD TiO_2 films, the repetition of the voltage scans resulted in a more linear J - V curve (Figure 4.6d). Although it is not clear why the samples produced in the two batches behaved differently, from the samples fabricated in the batch n.4 it was confirmed the presence of a threshold voltage that, once it is exceeded, strongly changes the electrical properties.

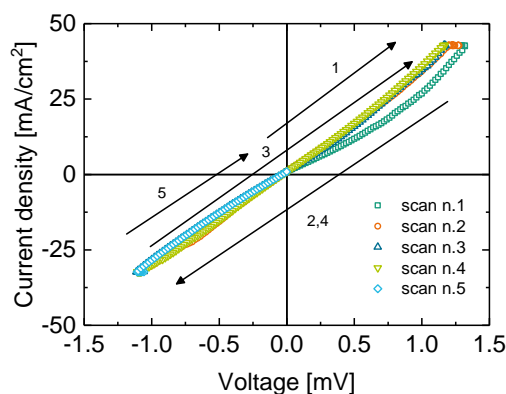


Figure 4.18: J - V hysteresis observed on samples with 20 nm thick TiO_2 prepared in the batch n.4; The numbers and the arrows represent the order and the directions of the scans: $0V \rightarrow +V \rightarrow -V \rightarrow +V \rightarrow -V \rightarrow 0V$.

Additionally, three exemplary samples with 20 nm thick TiO_2 films realised in the

batch n.4 were annealed at 225 °C. Figure 4.16 shows the effect of this thermal treatment: the resistance value of these samples drastically decreased to around $0.02 \Omega \text{ cm}^2$, which is a similar value than for samples of batch n.1 in the as-deposited state. This might be an indication that unintentionally some process temperatures after the ITO/TiO₂/ITO stack fabrication might have been different (e.g., the temperature used during the metal evaporation). In order to clearly understand the inconsistency observed in these two batches, a more detailed investigation is required.

However, other studies conducted at Fraunhofer ISE on perovskite solar cells showed low values of the resistance of TiO₂ grown with EBPVD and this was confirmed also by the PSCs result presented in Section 4.6. Thus, thermal treatment experiments were performed on samples prepared in the batch n.1 with 20 nm thick TiO₂. The results reported in Figure 4.19 indicate that the resistance of ITO/TiO₂/ITO stack with TiO₂ deposited with EBPVD slightly increased while increasing the annealing time and the annealing temperature until a maximum of around $0.5 \Omega \text{ cm}^2$ after 1 h at 150 °C. With further annealing steps at higher temperatures, the resistance drastically decreased reaching a value of around $0.15 \Omega \text{ cm}^2$ after 1 h at 200 °C, then it remained approximately constant. Afterwards, at an annealing temperature of 300 °C the resistance increased again. Figure 4.19c shows the resistance as function of the annealing time with fixed annealing temperatures. At 150 °C the resistance remained substantially unaltered after every annealing time. Samples annealed at 170 °C and 180 °C, after a very slight increase of the resistance, they showed a decrease after around 15 min reaching a minimum of $0.2 \Omega \text{ cm}^2$ after 1 h. The resistance of the sample annealed at 200 °C, that was around $0.7 \Omega \text{ cm}^2$, increased reaching a maximum of $2 \Omega \text{ cm}^2$ after 2 min and then it decreased increasing the annealing time, reaching a value slightly above $0.01 \Omega \text{ cm}^2$.

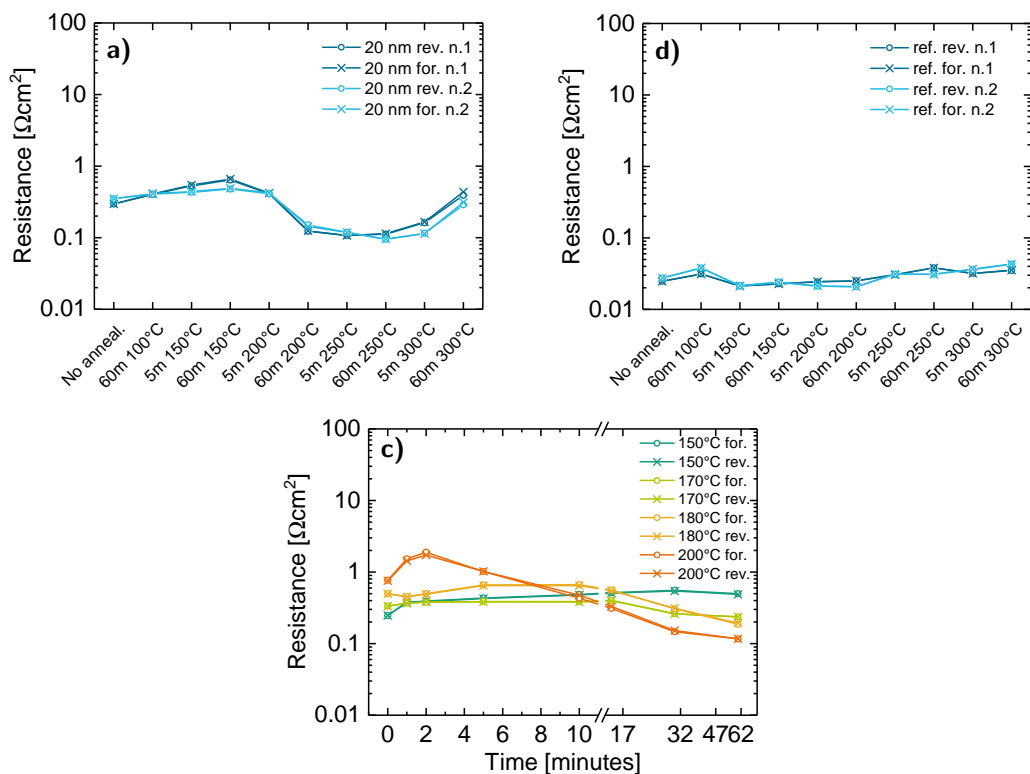


Figure 4.19: Thermal treatment effect on the resistance of samples with 20 nm thick TiO₂ films grown with EBPVD: (a) general overview of thermal effect on two samples; (b) reference samples without TiO₂; (c) detailed investigation of the thermal effect on samples with fixed temperature and cumulative annealing time.

4.2.4 General resistance comparison

In Figure 4.20, resistance values of as-deposited samples with 20 nm thick TiO₂ prepared with the three different deposition techniques are compared. For each technique two batches were performed. Both ALD techniques produced quite consistent results within the two different runs, even though with very different values. PE-ALD exhibited very high resistance, with mean values between around 15 Ωcm^2 and 30 Ωcm^2 and the single data-points are rather strongly scattered. T-ALD films, instead, showed high conductivity, with the resistance in the range of around 0.2 Ωcm^2 and 0.4 Ωcm^2 and with much less scattering. The results for the electron beam evaporated TiO₂ films were instead rather unexpected: the two runs produced completely different resistance values and no explanation for this behaviour was found. No significant differences in the deposition methods were discovered, suggesting that the TiO₂ films grown on ITO by EBPVD are very sensitive to even tiny condition variations. At the moment of writing,

it is not clear if this discrepancy is related on the bulk properties of TiO_2 films rather than defects at the interfaces with the two ITO layers. Also variations in the substrate processing, as well as in the metal evaporation of contacts, cannot be excluded and thus, further detailed investigation after this work is definitely necessary.

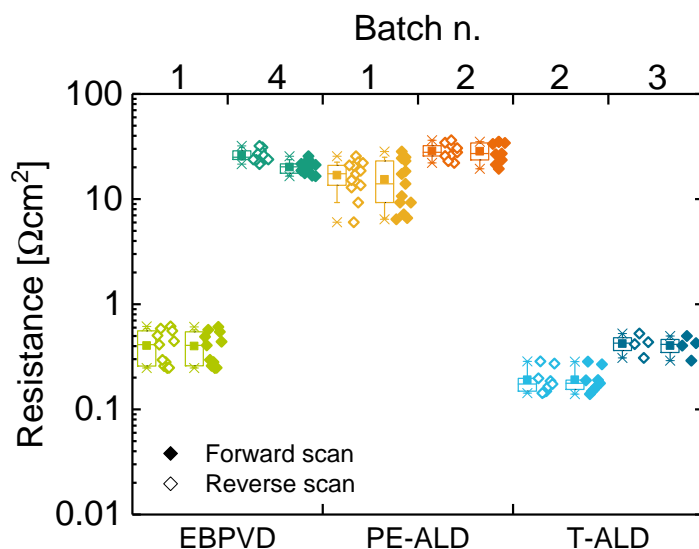


Figure 4.20: Resistance values of the samples with 20 nm thick TiO_2 films deposited with electron beam physical vapour deposition (EBPVD), plasma enhanced ALD (PE-ALD) and thermal ALD (T-ALD). For each technique, samples were realised in two separate batches.

4.3 X-ray Photoelectron Spectroscopy (XPS)

To clarify whether the observed differences in the resistivity are the result of a variation in the chemical composition, the XPS analysis was performed on the surface of 20 nm thick TiO_2 films deposited with EBPVD, T-ALD and PE-ALD on ITO. In the studies about the resistive switch effect of TiO_2 films, it was proposed that change of the conductivity can be a consequence of oxygen ions migration; in particular oxygen vacancies in form of *filaments* along the bulk improving the conductivity of the so formed TiO_{2-x} film [72–74, 76]. Since it has been seen that the samples with 20 nm thick TiO_2 deposited with PE-ALD dramatically change their conductivity when subjected to a thermal annealing at 225 °C for 15 min, (see Figure 4.10a), XPS analyses were performed also on two samples prepared with PE-ALD and annealed at this condition. To study if a possible difference of the atomic concentration of oxygen could arise during the annealing, one sample was annealed in air and one sample was annealed in a nitrogen filled glovebox to be sure that

no oxygen atoms from ambient air could be adsorbed at the surface during the annealing process.

Figure 4.21 and Figure 4.22 show the XPS overview spectra (on the left-hand side) before (black) and after sputtering (red) and the detail analysis around the Ti2p and O1s orbital peaks (right-hand side). In the overview spectra, carbon traces are visible for all the TiO₂ films but then they were completely removed after argon sputtering. This clearly indicates that the presence of carbon is a surface contamination due to the exposure of the surface to air and it was not present in the TiO₂ films. Very weak traces of argon were present only after sputtering and they must thus be considered as side effect of the sputtering itself. For all the TiO₂ deposition techniques it is evident that no other chemical contaminations are present.

Peaks at 531 eV, corresponding to the O_{1s} orbital, and at around 459 eV and 464 eV, corresponding to Ti_{2p₁} and Ti_{2p₃} orbitals respectively, were found for every TiO₂ film. Through the detail analysis of these peaks, the atomic concentrations of each TiO₂ film were calculated and are reported in Table 4.2. No significant differences of the chemical stoichiometry were observed comparing the different deposition techniques and therefore it was not possible to correlate the quite huge differences observed in the electrical conductivity of TiO₂ with its chemical composition. Furthermore, PE-ALD TiO₂ films that were annealed either in air or nitrogen showed a slightly (but not significantly) higher concentration of oxygen atoms with respect of the as-deposited sample. If we consider the proposed argument about oxygen vacancies distributed locally as very small filaments through the bulk, it is possible that, if differences of the oxygen concentration are present, they could not be observable with a standard XPS probe, since only a fixed local spot was investigated.

Table 4.2: Atomic concentration of different 20 nm thick TiO₂ films deposited with EBPVD, T-ALD and PE-ALD and calculated from detailed XPS analysis. The annealing in air and in the glovebox (N₂ atmosphere) were performed at 225 °C for 15 min.

Deposition technique	Anneal.	Concentration (%)		O:Ti ratio
		O _{1s}	Ti _{2p}	
EBPVD	-	69.08	30.92	2.23:1
T-ALD	-	68.91	31.09	2.22:1
	-	68.63	31.37	2.19:1
PE-ALD	air	69.15	30.85	2.24:1
	N ₂	68.98	31.02	2.22:1

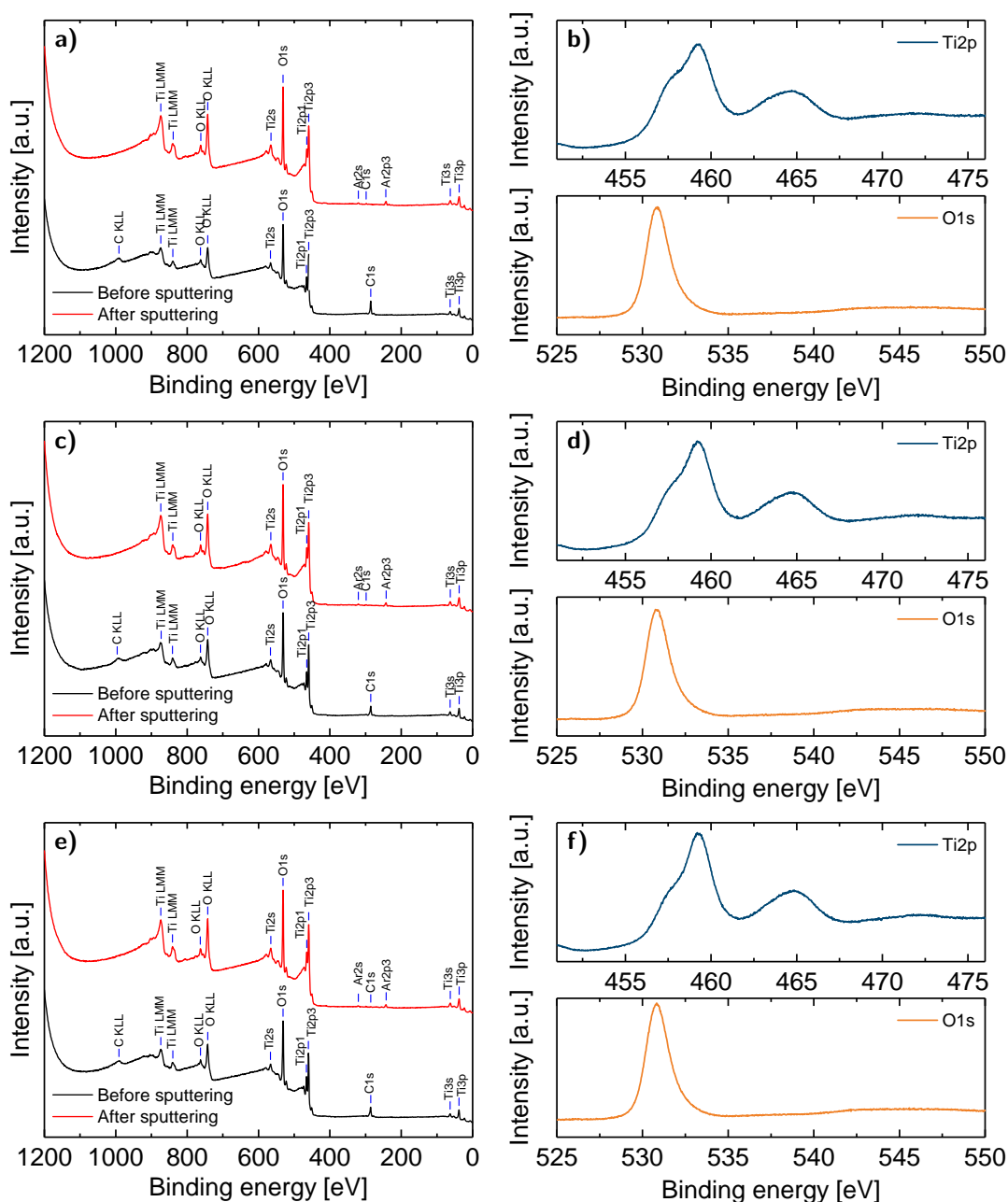


Figure 4.21: XPS investigation of 20 nm thick TiO_2 film grown on ITO with PE-ALD: (a) and (b) overview and detailed spectra as-deposited; (c) and (d) overview and detailed spectra annealed in air; (e) and (f) overview and detailed spectra annealed in the glovebox (nitrogen). The overview scans were performed before (black) and after argon sputtering (red). The atomic concentrations were obtained from the detailed scans around the Ti_{2p} and O_{1s} peaks.

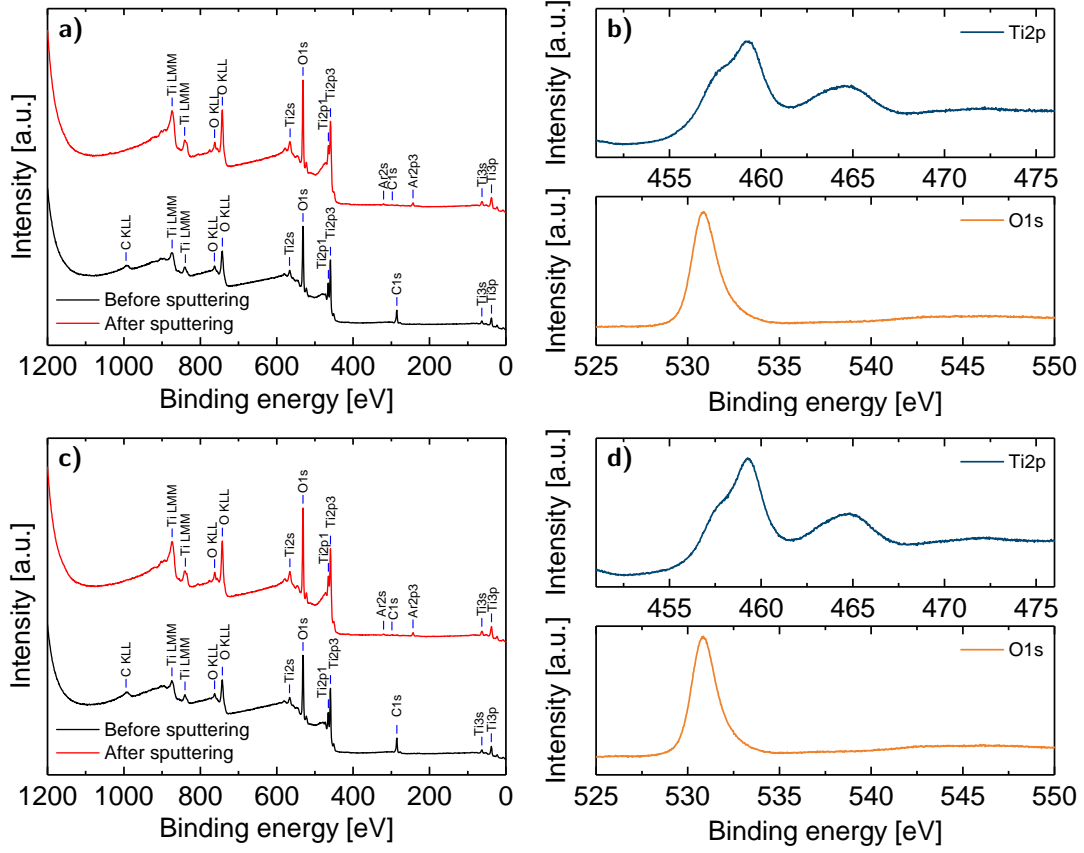


Figure 4.22: XPS investigation of 20 nm thick TiO₂ film grown on ITO with EBPVD and T-ALD. (a) and (b) overview and detailed spectra of TiO₂ grown with EBPVD respectively; (c) and (d) overview and detailed spectra of TiO₂ grown with T-ALD, respectively. The overview scans were performed before (black) and after argon sputtering (red). The atomic concentrations were obtained from the detailed scans around the Ti_{2p} and O_{1s} peaks.

4.4 X-ray Diffraction (XRD)

In recent studies, it has been shown that crystalline phases of TiO₂ (anatase, rutile and brookite) could affect the electrical properties of thin films and the resistivity. In particular, a lower resistivity was observed for TiO₂ film in crystalline or polycrystalline phases compared to the amorphous TiO₂. It has been proposed that the presence of TiO₂ crystalline grains can significantly reduce the electron effective mass enhancing the electron mobility [77]. It was also observed that the grain size increases increasing the annealing temperature which leads to a reduction of grain boundaries and a decrease of the resistivity [78, 79]. Therefore, in this work XRD investigation was performed with the aim to find a correlation between the crystalline structure and the electrical resistivity

of TiO₂ films deposited on ITO, especially after thermal annealing.

Figure 4.23 summarises all the XRD results of the TiO₂ films subjected to different annealing conditions. In Figure 4.23a, XRD spectra of TiO₂ films grown via PE-ALD and EBPVD as-deposited and TiO₂ films grown via PE-ALD, T-ALD and EBPVD after thermal annealing at 225 °C for 15 min are shown. Note that for spectra in light blue (annealed T-ALD TiO₂) and in grey (annealed PE-ALD TiO₂) samples with 2 × 2 cm² were used, while for all the other spectra half 4-inch wafers were used. Since the intensity of the signal for all this samples was rather low, it is probable that the difference between the spectra of these two groups is related to the amount of light reflected by the surface of the samples. All these samples did not show any evident peaks of crystalline TiO₂. Only one wide peak around 30.8° and one tiny peak at 51.2° were visible. It was found that those two peaks belong to the ITO layer underneath, as an independent measurement of a sample prepared with only ITO showed (blue line of Figure 4.23b). This clearly suggests that no crystalline phases were present for all the TiO₂ films deposited with the different techniques in the as-deposited state and even after a thermal treatment on hotplate for 15 min at 225 °C, the annealing condition which exhibited the strongest change in the electrical properties for samples prepared with PE-ALD (Figure 4.10a).

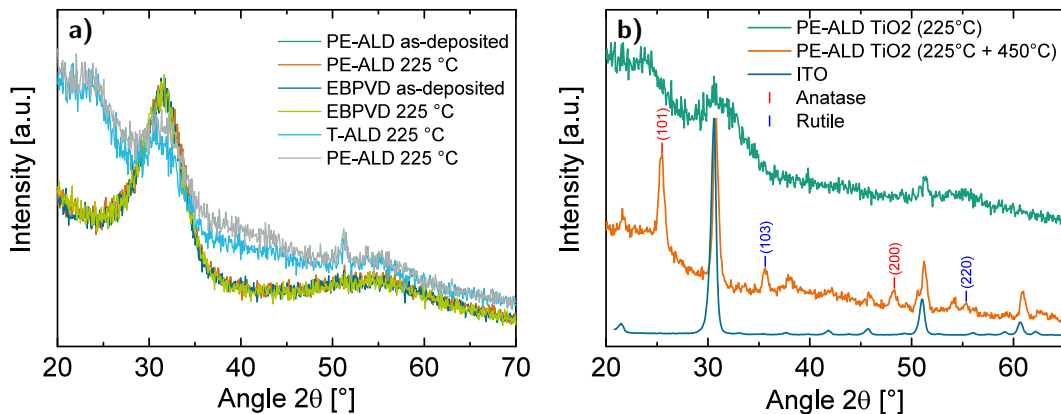


Figure 4.23: XRD spectra of: (a) 20 nm thick TiO₂ films deposited on ITO through the three different deposition techniques used. Samples in light blue and grey have been prepared in a separate batch and they have an area of 2 × 2 cm², while the other samples consist of half 4-inch wafers; (b) TiO₂ film prepared with PE-ALD after one annealing step at 225 °C for 15 min (green) and the same sample after an additional step at 450 °C for 15 min more (orange). Anatase and rutile TiO₂ crystalline phases appeared after this second step as well as peaks coming from the ITO layer underneath. In blue, the XRD spectrum of pure ITO without TiO₂ is shown. All the spectra are normalised.

Figure 4.23b shows the XRD spectra of PE-ALD TiO₂ after an annealing step at 225 °C for 15 min (green) and after an additional annealing step at 450 °C for 15 min

(orange). This test experiment showed the appearance of the anatase phase peaks at 25.5° and 48.3° and the rutile phase peaks at 35.5° and 55.4° (peaks position from ref [80]). After the second annealing step, peaks from the underneath ITO layer became much more distinguishable, as it can be seen from the spectrum of a sample prepared only with ITO (blue line of Figure 4.23b). This result seems to be in agreement with other studies where it was shown that TiO_2 grown with TTIP via PE-ALD crystallises at temperature above 400°C [59].

Thus, no correlation between the crystalline phases and the electrical properties of TiO_2 films was found, since all samples tested with the ITO/ TiO_2 /ITO sandwich showed a strong change of the current transport properties at temperatures around 200°C and 225°C , while, at these temperatures, all the TiO_2 films deposited on ITO were amorphous. Since TiO_2 was analysed only over one ITO layer, it cannot be excluded that when it is sandwiched between two ITO layers it potentially starts to crystallise even at lower temperature.

4.5 Dark Lock-in Thermography (DLIT)

DLIT investigation was performed on samples with top metal-grid contact (Figure 3.6c) to study the current distribution through the ITO/ TiO_2 /ITO sandwich. The samples were prepared on wafers that were split in two parts after the first double-side ITO coating. Then, each half wafer was coated with the same TiO_2 film separately. For each TiO_2 deposition technique, one half of the wafer was prepared with top metal-grid contact and used for the thermography, the second half of the wafer was prepared with top metal-pad contact and used as reference samples for resistance measurements.

Figure 4.24 shows DLIT pictures of samples with metal-grid top contact with 20 nm thick TiO_2 films deposited with EPBVD ((a), (b), (c)), T-ALD ((d), (e), (f)), 2 nm thick PE-ALD TiO_2 ((g), (h), (i)) and 20 nm thick PE-ALD TiO_2 ((j), (k), (l)). Since these groups of samples had different resistance, different input voltages were used to record the DLIT images. To have a better comprehension and comparison, the images shown in Figure 4.24 have been rescaled as function of the input power.

The bright spot of the sample shown in Figure 4.24a is most probably to be considered as misalignment of the needle probes directly on ITO rather than on metal-grid. All the current is in fact flowing only through this little area instead of homogeneously flowing below the entire grid. In general, for almost all the samples, DLIT investigation revealed bright areas which might be due to inhomogeneity of the TiO_2 films, rather than real pinholes. TiO_2 films grown with the EPBVD appeared to be the most inhomogeneous films, as it was expected from this ideally less precise deposition technique compared to the ALD. In particular, the films grown with T-ALD showed the best homogeneity without particularly bright hot spots. The only exception is for the sample shown in Figure 4.24f, but also in this case the bright spot close to the contact region with the

needle probes could have been produced by a misalignment or by an artefact due to the metal-grid. Also the 2 nm films grown with PE-ALD did not revealed significant shunts except for that ones at the edges and near to contact region with the probes. Contrariwise, two of the three samples with 20 nm shown in Figure 4.24j and Figure 4.24k clearly showed the presence of very bright shunts that can be interpreted as true pinholes.

Resistance measurements of the samples used for DLIT investigation and samples prepared with top metal-pad contact were recorded before a thermal annealing for 15 min at 225 °C and the results are shown in Figure 4.25 and Figure 4.26, respectively. DLIT images of the samples recorded after thermal annealing are not shown in this work, since we did not observe any difference compared to the images shown in Figure 4.24 before annealing. However, some discrepancy was observed for both groups of samples provided with grid and pad contacts. In particular, for both groups, the resistance of samples with EBPVD TiO₂ resulted to be higher than expected, as it was observed for samples fabricated in the batch n.4 and mentioned in Section 4.2.3. In fact, all the samples prepared with grid and pad contacts showed a resistance above 10 Ω cm² (Figure 4.25a and Figure 4.26a). Furthermore, only samples with pad contacts showed a strong decrease of the resistance after thermal annealing (Figure 4.26a), as already mentioned in Section 4.2.3, while the resistance of samples with the grid remained substantially unaltered (Figure 4.25a).

Also samples with 20 nm thick PE-ALD TiO₂ behaved quite unexpectedly: the resistance of samples with metal grid shown Figure 4.25d slightly decreased from around 10 Ω cm² to around 6 Ω cm² after annealing, while the resistance samples with pad remained unaltered around 5 Ω cm² – 11 Ω cm². However, a strong decrease of the resistance was expected (down to around 0.05 Ω cm², Figure 4.10a), especially for samples with pad contacts which were fabricated identically to the samples used for the resistance measurements shown in Section 4.2.1.

The samples shown in Figure 4.25b with TiO₂ deposited with T-ALD, showed a resistance between 1 Ω cm² and 3 Ω cm², that is in the expected range considering the contribution of at least 0.8 Ω cm² to the series resistance by the metal-grid (see Figure 4.12 for resistance measurements of 20 nm thick TiO₂ layers). Also the samples with top metal-pad contact (Figure 4.26b) showed an expected value of the resistance for the as-deposited state. Although, after the thermal annealing both of these two groups showed an increase of the resistance, in particular the samples with metal-pads, which was not expected (see the red curve of Figure 4.15a).

The resistance of samples with a 2 nm thick PE-ALD TiO₂ film and pad contact (Figure 4.26c) was around 2 Ω cm² before annealing. This value is slightly below the value of around 5 Ω cm² measured before for similar samples (see Section 4.2.1 and Figure 4.7). The resistance of samples with the grid contact (Figure 4.25c) was in the same range (3 Ω cm²) as for samples with pad contacts, considering the contribution of the grid. However, a very strong decrease, of around two magnitude orders, was expected after the annealing of the samples with pad contacts (see the red curve of Figure 4.10e) but,

similarly to samples with 20 nm thick PE-ALD TiO_2 , no significant changes were observed after thermal treatment.

The causes of these discrepancies have not been found and further investigation are needed after this work. Nevertheless, from this experiment it can be concluded that the ALD, in particular the T-ALD, provided quite homogeneous films. However, as mentioned previously in this section, bright spots were observed in two of the three samples with 20 nm thick PE-ALD films (Figure 4.24k and Figure 4.24l) suggesting that pinholes could arise during the deposition of the TiO_2 film.

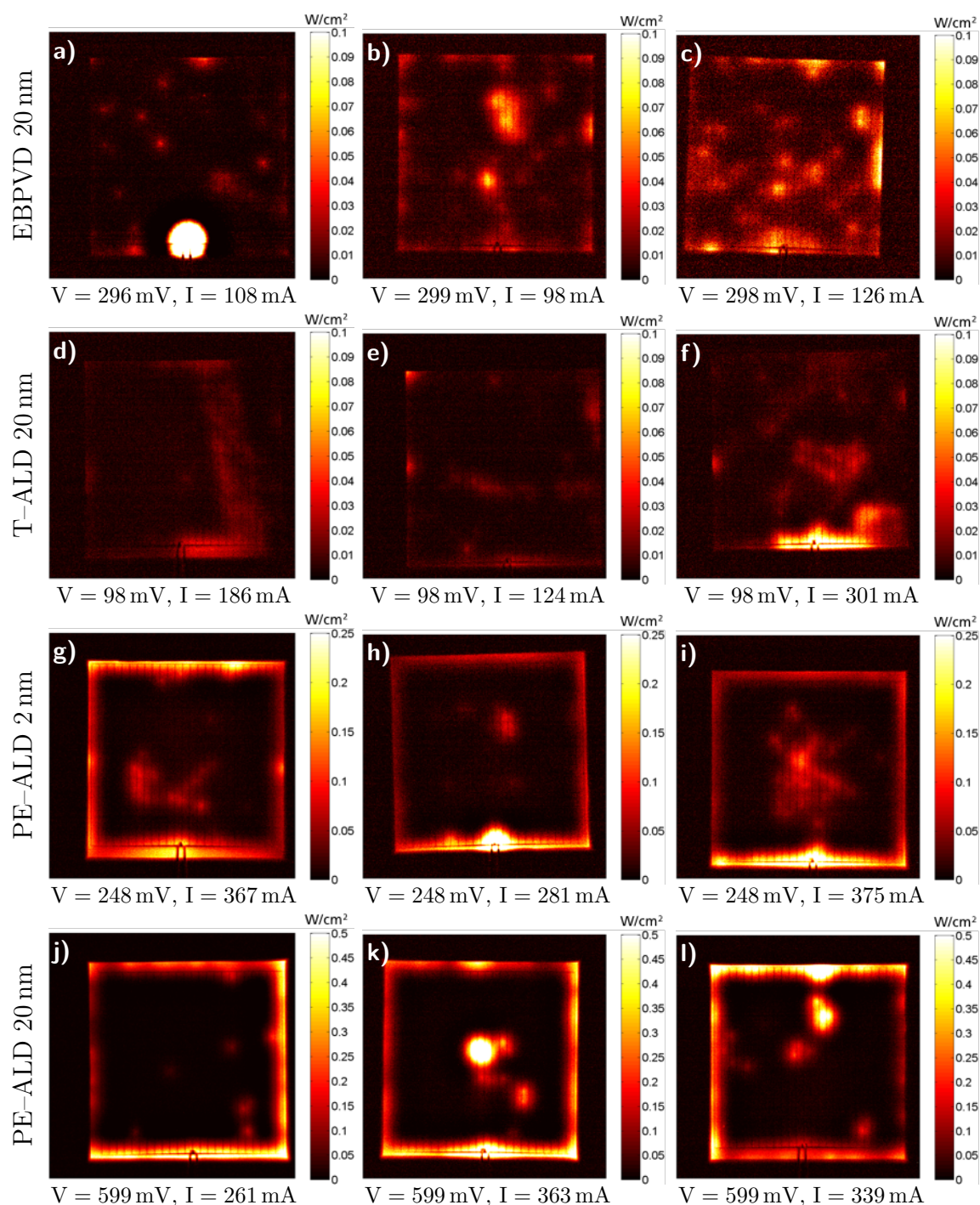


Figure 4.24: DLIT images of TiO_2 films grown by: (a), (b), (c) EBPVD 20 nm; (d), (e), (f) T-ALD 20 nm; (g), (h), (i) PE-ALD 2 nm; (j), (k), (l) PE-ALD 20 nm. Three identically processed samples are shown per each TiO_2 deposition technique. The pictures have been rescaled as function of the input power of the samples.

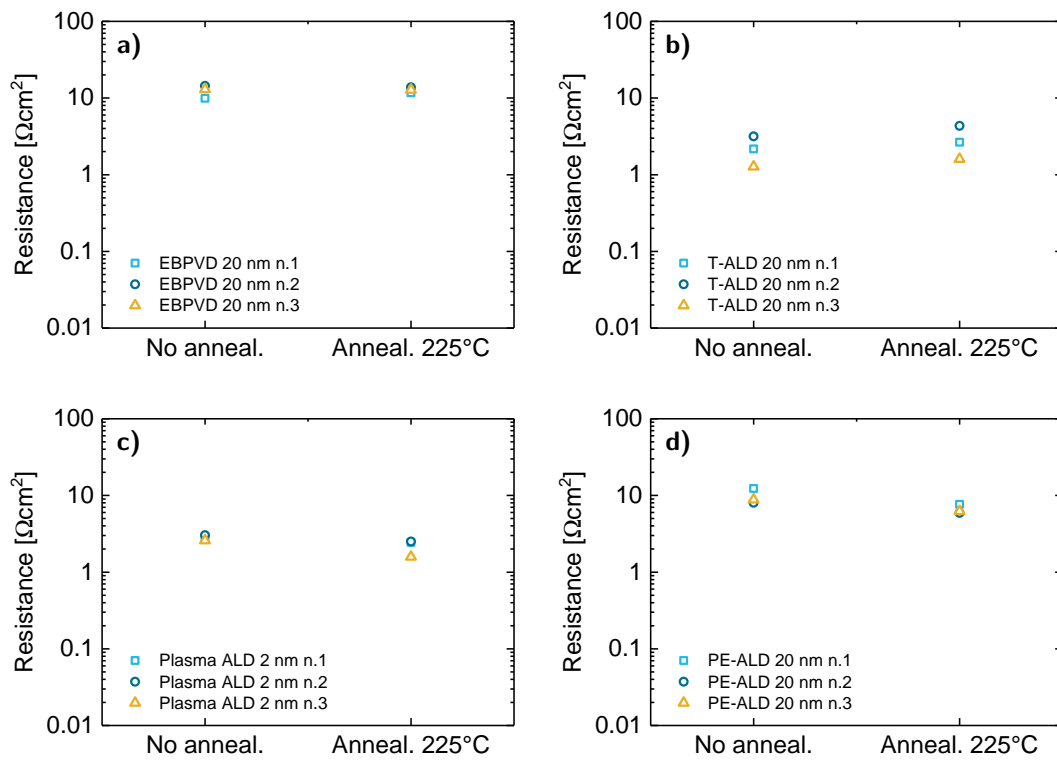


Figure 4.25: Resistance measurements of samples with top metal-grid contact used for the DLIT investigation shown Figure 4.24.

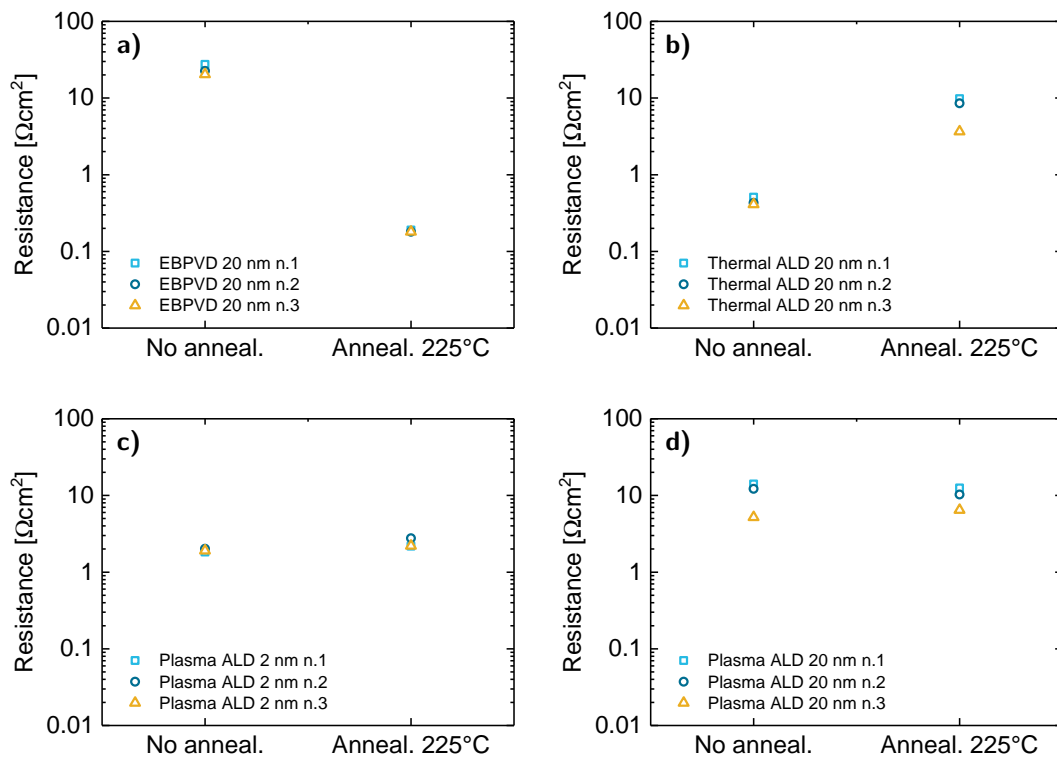


Figure 4.26: Resistance measurements of samples with top metal-pad contact used as reference for the samples prepared with top metal-grid shown Figure 4.24 and Figure 4.25.

4.6 Perovskite Solar Cells Results

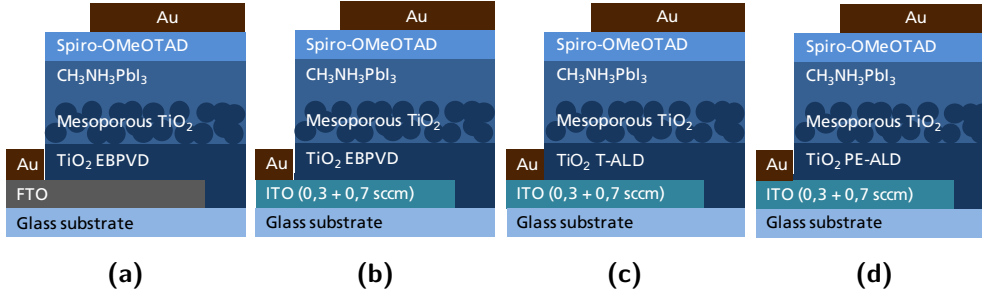


Figure 4.27: Perovskite solar cells (PSCs) with 20 nm thick TiO₂ films acting as electron transport layer deposited on ITO through (b) EBPVD, (c) T-ALD and (d) PE-ALD. Two ITO layers were coated with different oxygen flow: 0.3 sccm to improve the lateral conductivity and 0.7 sccm for having the same contact before and like in a tandem cell. PSCs prepared with 20 nm thick TiO₂ on FTO ((a)) were used as reference cells.

This work ends with a preliminary study of the efficiencies of regular perovskite solar cells (PSCs) with TiO₂ acting as electron transport layer and with mesoporous TiO₂ scaffold processed at low temperature. Figure 4.27 shows the PSC structure with 20 nm thick TiO₂ films processed through EBPVD, T-ALD and PE-ALD. Figure 4.27a shows a PSC with compact TiO₂ layer deposited with EBPVD on a FTO layer. This represents one of the standard PSCs realised at Fraunhofer ISE so far and thus, cells with this structure have been prepared as reference cells. Figure 4.27b, (c) and (d) show PSCs featuring the same 20 nm thick EBPVD, T-ALD, PE-ALD TiO₂ layers respectively and the same ITO/TiO₂ on the rear studied in this thesis.

All the electrical parameters, the short-circuit current density (J_{SC}), the open circuit voltage (V_{OC}), the fill factor (FF) and the power conversion efficiency (PCE) are shown in Figure 4.28. Unfortunately, problems with T-ALD occurred during the deposition process, resulting in a final wrong thickness of the TiO₂ films of around 9 nm to 10 nm instead of the target thickness of 20 nm. In general, cells processed with EBPVD and ITO exhibited the highest PCE and FF values (higher than reference cells with FTO), despite a significant hysteresis between the forward (−0.1 V to 1.2 V) and reverse (1.2 V to −0.1 V) scans being present as shown in Figure 4.29a (red). On the other hand, cells processed with PE-ALD showed slightly higher V_{OC} compared to the reference cells, while the J_{SC} was in the same range. In all cases, cells with TiO₂ deposited on ITO revealed a less prominent hysteresis between the two scan directions, especially with TiO₂ deposited through PE-ALD. PSCs realised with T-ALD showed the worst performance, as expected from process issues during the TiO₂ deposition. In addition to the low values measured, significant scattering between the same kind of cells was recorded that can indicate a strong inhomogeneity of the T-ALD TiO₂ films.

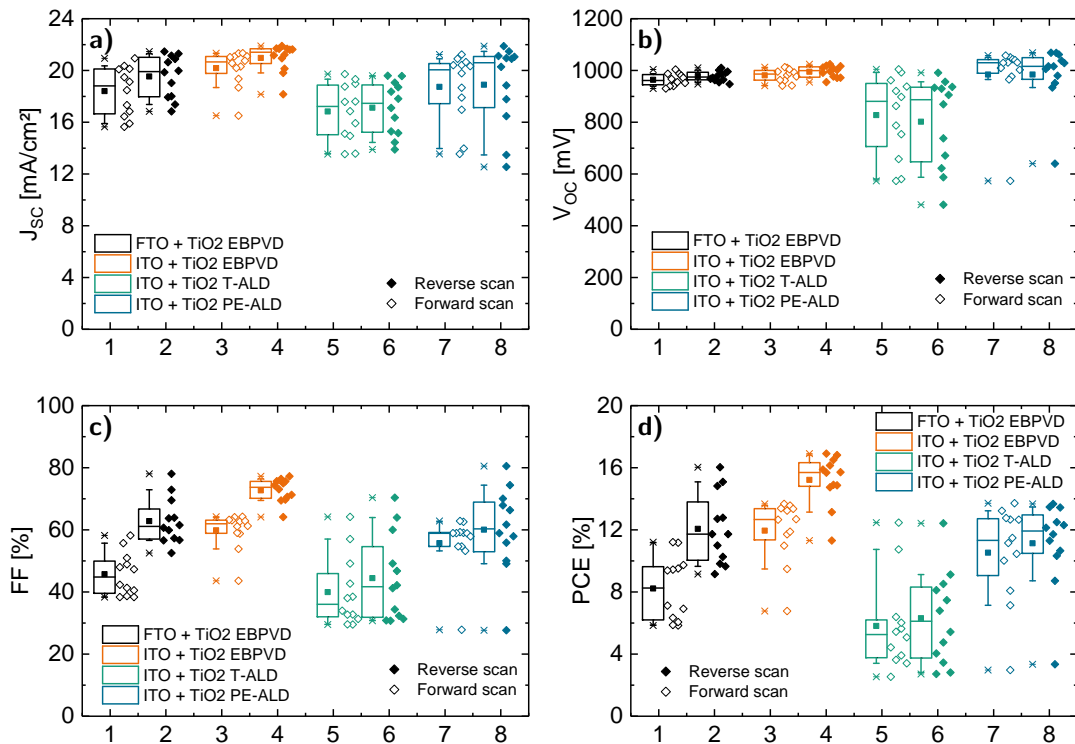


Figure 4.28: Comparison of perovskite solar cells with TiO₂ films deposited on ITO through EBPVD, T-ALD and PE-ALD. Some process problems occurred during the T-ALD deposition causing a wrong layer thickness. Cells with TiO₂ deposited with EBPVD on FTO were used as reference.

In Figure 4.29, current–voltage characteristics of the best cell of each group are reported. Zooming the J – V curves around the V_{OC} (Figure 4.29b) it is possible to appreciate the different values of the series resistance of the entire cells, represented by the inverse slope of the curves. Qualitatively, it can be seen that the reference cell and one processed by EBPVD have similar slope and thus similar series resistance, instead the cell realised using the PE-ALD showed a lower slope that indicates a higher series resistance as it is also shown in Figure 1.3.

Finally, through a fit of the two-diodes model applied to the J – V curves recorded under illumination, the series resistance of the PSCs was estimated. It must be considered that the series resistance here calculated is the series resistance of the whole cell, including all layers and interfaces occurring in the PSC and not only the ITO/TiO₂ films. The results of the PSCs with TiO₂ deposited by EBPVD both on ITO and FTO shown in Figure 4.30, confirmed its good conductivity as reported in Figure 4.2. The

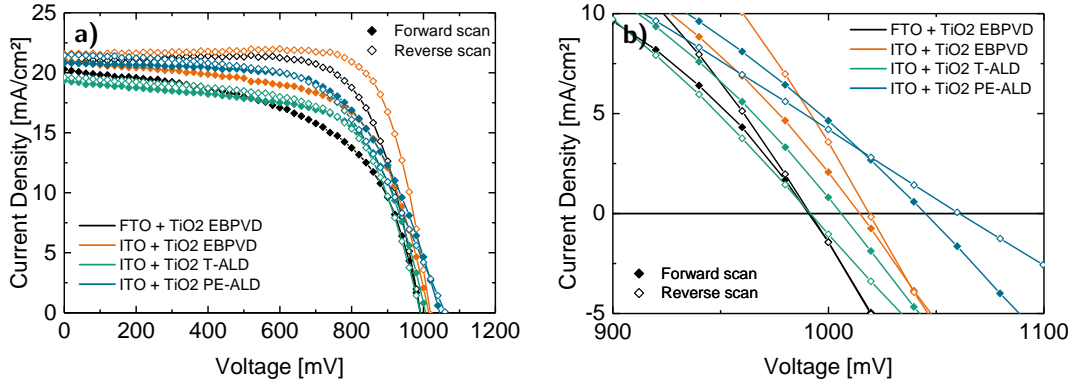


Figure 4.29: (a) current–voltage characteristics of perovskite solar cells prepared with TiO_2 film processed differently and (b) a zoom detail of the same characteristics around the open-circuit voltage points. The slopes represent the overall series resistance of the cells.

value is around $5 \Omega \text{ cm}^2$ which is a typical value for series resistance in PSCs [12, 81–86]. Therefore, the results reported in Figure 4.16 were probably caused by some unidentified issue during the sample processing. Cells processed with PE–ALD presented a series resistance in good agreement with the results shown Figure 4.2 and Figure 4.7, confirming the good homogeneity and stability of this technique. Even though TiO_2 processed with T–ALD was the most promising layer in terms of conductivity and thickness precision, the process issues during the TiO_2 deposition via T–ALD for the PSCs completely compromised the final results, as it can be clearly seen also by the high scattering of the resistance values. Nevertheless, these values are in the same order of magnitude as of the samples prepared with 10 nm thick TiO_2 reported in Figure 4.12, where this thickness revealed the highest resistance values. These results then encourage a further analysis of such kind of TiO_2 as ETL for PSCs.

Figure 4.27 clearly shows a significant difference between the forward and reverse scan direction for all the measured values. The origin of such hysteresis in perovskite solar cells is still under discussion in literature and it might be due to ion migration, charge trapping at contacts or capacitive effects [87]. It has been shown that the better the contact of the ETL the lower the hysteresis. Several different routes have been recently tested to improve the contact: contact improving by UV Curing time [37], contact improving by doping [88] using different deposition techniques and material (e.g. solution processing) [12], or using double-layer selective contacts [89]. From this point of view, it seems that the PE–ALD gives a better contact to the perovskite than evaporated TiO_2 , but however, as the resistance of the PE–ALD TiO_2 is much higher than for evaporated TiO_2 (see Figure 4.2) the overall series resistance for evaporated TiO_2 is lower and thus, the performance is better.

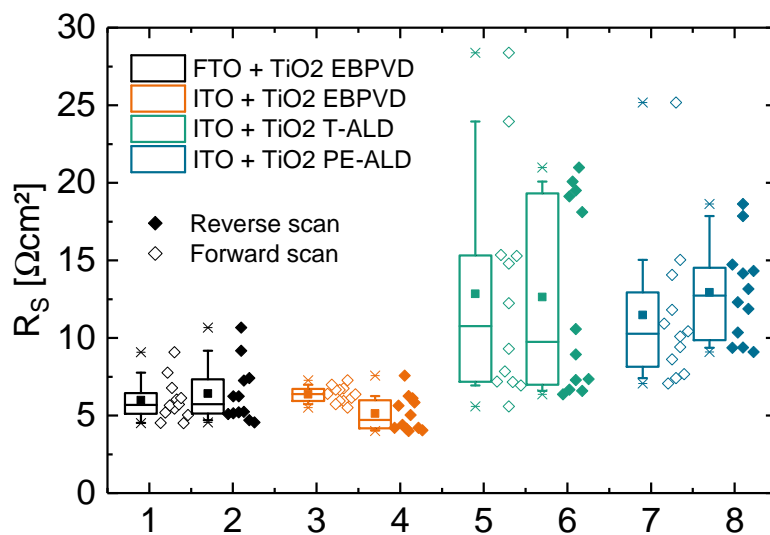


Figure 4.30: Series resistance of the analysed PSCs obtained from two-diodes model fits to the IV curves under illumination.

Chapter 5

Conclusion and outlook

In this experimental work, it has been analysed in detail an innovative interconnection layer stack for perovskite–silicon tandem solar cells composed of titanium dioxide (TiO_2) deposited on indium tin oxide (ITO) through three different thin film deposition techniques: electron beam physical vapour deposition (EBPVD), thermal atomic layer deposition (T–ALD) and plasma enhanced atomic layer deposition (PE–ALD). In particular, this stack is intended for two-terminal monolithic tandem devices, where the top sub-cell is a perovskite cell (PSC) and the bottom subcell is a silicon heterojunction solar cell (SHJ), considered as very promising for this role. In this structure, the ITO layer is the front contact of the SHJ cell and the TiO_2 layer is the rear contact of the PSC, performing also the function of electron transport layer (ETL).

The analysis mainly focused on the characterisation of the series resistance of this layer stack, comparing the three deposition techniques used. The analysis also included X-ray diffraction (XRD) for the investigation of the crystal structure and X-ray photoelectron spectroscopy (XPS) for the investigation chemical composition of the TiO_2 films. In parallel, a qualitative investigation of shunts generated during the TiO_2 depositions and after the dicing of the samples was performed by dark lock-in thermography (DLIT). An exhaustive analysis of the thermal treatments of the samples was conducted highlighting a strong dependence of the resistance of differently processed TiO_2 films.

A first investigation of as-deposited 20 nm thick TiO_2 films sandwiched between two ITO layers, showed that samples processed with T–ALD, using titanium tetraisopropoxide (TTIP) as titanium precursor and H_2O as oxidiser at 200 °C, exhibited the lowest values of the series resistance, with a mean value between $0.2 \Omega \text{ cm}^2$ and $0.4 \Omega \text{ cm}^2$. Similar values were observed for samples processed with EBPVD at room temperature, making these two techniques suitable for tandem devices even without requiring any thermal treatment. Contrariwise, samples with TiO_2 films processed with PE–ALD revealed a series resistance above $15 \Omega \text{ cm}^2$ not useful for solar tandem applications. A comparison with 20 nm thick insulating aluminium oxide (Al_2O_3) suggested that the measurement of the resistance could be limited by the shunts produced at the sample during cutting

them to the desired size.

The analysis of samples subjected to thermal treatments showed a very strong dependence for samples processed with PE-ALD. In particular, the resistance of samples with 20 nm thick TiO₂ dropped below 0.1 Ω cm² after annealing on a hotplate for 15 min at 225 °C in air. At the same annealing conditions, a small resistance decrease was observed also for samples processed with EBPVD and T-ALD. Nevertheless, considering the thermal instability of SHJ it is suggested to avoid thermal sintering of the TiO₂ films deposited with EBPVD and T-ALD since no significant improvements of the conductivity are required.

While samples with TiO₂ films deposited with all the different techniques showed a perfectly ohmic behaviour in the voltage range used to achieved a current density of around 20 mA/cm² (working condition of a perovskite solar cell), it was found that the samples processed with PE-ALD are not ohmic if subjected to voltage biases higher than around 1 V absolute value in both positive and negative directions. Surprisingly, the repetition of voltage scans above this value produced a decreasing of the resistance towards a *quasi*-ohmic saturation current-voltage characteristic. A very similar behaviour was observed for samples processed with EBPVD in a batch where the EBPVD samples resulted in an unexpected high resistance, comparable to samples with PE-ALD TiO₂. Recent studies of similar ITO/TiO₂/ITO stacks showed an effect named *resistive switch*. Thanks to this effect the resistance of these structures can be switched between two states using biases higher than a certain symmetric threshold voltage [72–74]. However, in this study the same effect was not observed. Nevertheless, a threshold voltage that can significantly change the electrical properties once it is exceeded has been discovered.

The XPS investigation of the surface of the TiO₂ films showed an atomic O:Ti concentration ratio of around 2.2 without other element contamination, suggesting a homogeneous chemical composition achieved with all the deposition techniques used. Also TiO₂ films deposited with PE-ALD after thermal annealing at 225 °C for 15 min revealed no significant differences in the stoichiometry. The XRD analysis revealed that TiO₂ deposited with EBPVD, T-ALD and PE-ALD is amorphous as-deposited and even after this thermal annealing condition at which the strongest decrease of the resistance was observed. One test sample prepared with PE-ALD was subjected to an additionally annealing step at 450 °C and it showed the presence of anatase and rutile TiO₂ crystalline phases as expected for such high annealing temperatures.

DLIT investigation showed a significant presence of shunts at the edges of the samples caused by the dicing of the samples, especially for low conductive samples prepared with PE-ALD, suggesting a possible limitation in the measurement of the series resistance. Nevertheless, this limitation above 20 Ω cm² to 30 Ω cm² is not relevant for the purposes of this work, since these values of the series resistance are not suitable for perovskite-silicon tandem solar cells. The shunt investigation also showed bright spots in TiO₂ films prepared with PE-ALD that can be interpreted as most-likely pinholes produced during the deposition itself which result in a shunt of between both ITO layers

in the ITO/TiO₂/ITO sandwich. However, samples realised in this run did not behave as expected after thermal annealing.

As final experiment, perovskite solar cells were produced using TiO₂ films deposited with EBPVD, T-ALD and PE-ALD as compact electron transport layer and an ITO contact. The champion cell processed with EBPVD exhibited a power conversion efficiency (PCE) of 13.4% and 16.8% in forward and reverse scan, respectively. Cells prepared through PE-ALD, instead, showed a PCE of 13.7% and 13.4% for forward and reverse scan direction, respectively. This result shows a less prominent hysteresis than for EBPVD. Unfortunately, it is difficult to draw conclusion about T-ALD since only a partial deposition of the TiO₂ films occurred due to processing problem with the deposition system.

To conclude, samples with TiO₂ films processed with EBPVD, T-ALD and PE-ALD showed significant different results in terms of electrical conductivity and PCE of PSCs. In general, the resistance of TiO₂ films deposited with EBPVD and T-ALD on ITO is low enough to build perovskite-silicon solar tandem cells with this stack as interconnection layer. Also samples prepared with PE-ALD revealed a very good conductivity if treated with thermal annealing. Despite this different characteristics between samples treated with different deposition techniques, no significant differences were found in the chemical composition as well as on the crystalline structure, and the reasons therefore remain unclear. It has been shown, especially for PE-ALD, that the resistivity of the TiO₂ films are mainly controlled by the properties of the bulk but also the interfaces with ITO play an important role on the electrical properties. Defects at the interfaces, trap states and the alignment of the energy bands could potentially affect dramatically the overall conduction of the ITO/TiO₂ stack and thus, the efficiency of the complete tandem solar cell.

A complete perovskite-silicon tandem solar cell was not investigated in this work since both of the subcells are still in development at Fraunhofer ISE and the first tests are scheduled for the coming months after the end of this work.

The results presented in this work must encourage to pursue further research on these layers, since it has been demonstrated that they are potentially suitable as interconnection layers for perovskite-silicon tandem solar cells. Some inconsistencies have been observed within the experiments of this thesis, which could not be explained so far and which definitively show that more experimental work is necessary in order to understand more completely the contact properties of TiO₂ and the ITO/TiO₂ interfaces. Nevertheless TiO₂ is a widely used material in the optoelectronic and photovoltaic industry, with this work it has been demonstrated that it is still far from being fully characterised and understood.

Bibliography

- [1] W. Shockley and H. J. Queisser, “Detailed balance limit of efficiency of p-n junction solar cells”, *Journal of Applied Physics*, vol. 32, no. 3, p. 510, 1961, ISSN: 00218979. DOI: [10.1063/1.1736034](https://doi.org/10.1063/1.1736034).
- [2] A. Richter, M. Hermle, and S. W. Glunz, “Reassessment of the limiting efficiency for crystalline silicon solar cells”, *IEEE Journal of Photovoltaics*, vol. 3, no. 4, pp. 1184–1191, 2013. DOI: [10.1109/jphotov.2013.2270351](https://doi.org/10.1109/jphotov.2013.2270351).
- [3] K. Yoshikawa, H. Kawasaki, W. Yoshida, T. Irie, K. Konishi, K. Nakano, T. Uto, D. Adachi, M. Kanematsu, H. Uzu, and K. Yamamoto, “Silicon heterojunction solar cell with interdigitated back contacts for a photoconversion efficiency over 26%”, *Nature Energy*, vol. 2, p. 17 032, 2017, ISSN: 2058-7546. DOI: [10.1038/nenergy.2017.32](https://doi.org/10.1038/nenergy.2017.32).
- [4] M. A. Green, Y. Hishikawa, W. Warta, E. D. Dunlop, D. H. Levi, J. Hohl-Ebinger, and A. W. Ho-Baillie, “Solar cell efficiency tables (version 50)”, *Progress in Photovoltaics: Research and Applications*, vol. 25, no. 7, pp. 668–676, 2017, ISSN: 10627995. DOI: [10.1002/pip.2909](https://doi.org/10.1002/pip.2909).
- [5] M. A. Green, A. Ho-Baillie, and H. J. Snaith, “The emergence of perovskite solar cells”, *Nature Photonics*, vol. 8, no. 7, pp. 506–514, 2014, ISSN: 1749-4885. DOI: [10.1038/nphoton.2014.134](https://doi.org/10.1038/nphoton.2014.134).
- [6] N.-G. Park, M. Grätzel, T. Miyasaka, K. Zhu, and K. Emery, “Towards stable and commercially available perovskite solar cells”, *Nature Energy*, vol. 1, p. 16 152, 2016. DOI: [10.1038/nenergy.2016.152](https://doi.org/10.1038/nenergy.2016.152).
- [7] M. H. Futscher and B. Ehrler, “Efficiency limit of perovskite/si tandem solar cells”, *ACS Energy Letters*, vol. 1, no. 4, pp. 863–868, 2016, ISSN: 2380-8195. DOI: [10.1021/acsenergylett.6b00405](https://doi.org/10.1021/acsenergylett.6b00405).
- [8] G. Adam, M. Kaltenbrunner, E. D. Głowacki, D. H. Apaydin, M. S. White, H. Heilbrunner, S. Tombe, P. Stadler, B. Ernecker, C. W. Klampfl, N. S. Sariciftci, and M. C. Scharber, “Solution processed perovskite solar cells using highly conductive pedot: Pss interfacial layer”, *Solar Energy Materials & Solar Cells*, vol. 157, pp. 318–325, 2016. DOI: [10.1016/j.solmat.2016.05.011](https://doi.org/10.1016/j.solmat.2016.05.011).

-
- [9] O. Malinkiewicz, A. Yella, Y. H. Lee, G. M. Espallargas, M. Graetzel, M. K. Nazeeruddin, and H. J. Bolink, “Perovskite solar cells employing organic charge-transport layers”, *Nature Photonics*, vol. 8, no. 2, pp. 128–132, 2013, ISSN: 1749-4885. DOI: [10.1038/nphoton.2013.341](https://doi.org/10.1038/nphoton.2013.341).
- [10] Y. Liu, Q. Chen, H.-S. Duan, H. Zhou, Y. Yang, H. Chen, S. Luo, T.-B. Song, L. Dou, and Z. Hong, “A dopant-free organic hole transport material for efficient planar heterojunction perovskite solar cells”, *J. Mater. Chem. A*, vol. 3, no. 22, pp. 11 940–11 947, 2015, ISSN: 2050-7488. DOI: [10.1039/C5TA02502H](https://doi.org/10.1039/C5TA02502H).
- [11] A. B. Huang, J. T. Zhu, J. Y. Zheng, Y. Yu, Y. Liu, S. W. Yang, S. H. Bao, L. Lei, and P. Jin, “Achieving high-performance planar perovskite solar cells with co-sputtered co-doping nio x hole transport layers by efficient extraction and enhanced mobility”, *J. Mater. Chem. C*, vol. 4, no. 46, pp. 10 839–10 846, 2016, ISSN: 2050-7526. DOI: [10.1039/C6TC03624D](https://doi.org/10.1039/C6TC03624D).
- [12] E. H. Anaraki, A. Kermanpur, L. Steier, K. Domanski, T. Matsui, W. Tress, M. Saliba, A. Abate, M. Grätzel, A. Hagfeldt, and J.-P. Correa-Baena, “Highly efficient and stable planar perovskite solar cells by solution-processed tin oxide”, *Energy Environ. Sci.*, vol. 9, no. 10, pp. 3128–3134, 2016, ISSN: 1754-5692. DOI: [10.1039/C6EE02390H](https://doi.org/10.1039/C6EE02390H).
- [13] H. Yang, T. Wu, T. Hu, X. Hu, L. Chen, and Y. Chen, “A homogeneous ethanedithiol doped zno electron transporting layer for polymer solar cells”, *J. Mater. Chem. C*, vol. 4, no. 37, pp. 8738–8744, 2016, ISSN: 2050-7526. DOI: [10.1039/C6TC02369J](https://doi.org/10.1039/C6TC02369J).
- [14] G. Yang, H. Tao, P. Qin, W. Ke, and G. Fang, “Recent progress in electron transport layers for efficient perovskite solar cells”, *J. Mater. Chem. A*, vol. 4, no. 11, pp. 3970–3990, 2016, ISSN: 2050-7488. DOI: [10.1039/c5ta09011c](https://doi.org/10.1039/c5ta09011c).
- [15] H. Liu, Z. Huang, S. Wei, L. Zheng, L. Xiao, and Q. Gong, “Nano-structured electron transporting materials for perovskite solar cells”, *Nanoscale*, vol. 8, no. 12, pp. 6209–6221, 2016, ISSN: 2040-3364. DOI: [10.1039/c5nr05207f](https://doi.org/10.1039/c5nr05207f).
- [16] A. Guerrero, E. J. Juarez-Perez, J. Bisquert, I. Mora-Sero, and G. Garcia-Belmonte, “Electrical field profile and doping in planar lead halide perovskite solar cells”, *Applied Physics Letters*, vol. 105, no. 13, p. 133 902, 2014. DOI: [10.1063/1.4896779](https://doi.org/10.1063/1.4896779).
- [17] F. Di Giacomo, G. Lucarelli, S. Pescetelli, F. Matteocci, S. Razza, A. Di Carlo, A. D’Epifanio, S. Licocchia, T. Brown, V. Zardetto, W. M. Kessels, and M. Creatore, “Device architectures with nanocrystalline mesoporous scaffolds and thin compact layers for flexible perovskite solar cells and modules”, in *2015 IEEE 15th International Conference on Nanotechnology (IEEE-NANO)*, Francesco Di Giacomo, Giulia Lucarelli, Sara Pescetelli, Fabio Matteocci, Stefano Razza, Aldo Di Carlo, Alessandra D’Epifanio, Silvia Licocchia, Thomas Brown, Valerio Zardetto, Wilhel-

- mus M.M. Kessels, Mariadriana Creatore, Ed., pp. 739–742. DOI: [10.1109/NANO.2015.7388714](https://doi.org/10.1109/NANO.2015.7388714).
- [18] S. de Wolf, A. Descoeurdes, Z. C. Holman, and C. Ballif, “High-efficiency silicon heterojunction solar cells: A review”, *Green*, vol. 2, no. 1, pp. 7–24, 2012. DOI: [10.1515/green-2011-0018](https://doi.org/10.1515/green-2011-0018).
- [19] H. Kim, C. M. Gilmore, A. Piqu, J. S. Horwitz, H. Mattoussi, H. Murata, Z. H. Kafafi, and D. B. Chrisey, “Electrical, optical, and structural properties of indium? tin?oxide thin films for organic light-emitting devices”, *Journal of applied physics*, vol. 86, no. 11, pp. 6451–6461, 1999. DOI: [10.1063/1.371708](https://doi.org/10.1063/1.371708).
- [20] S. Albrecht, M. Saliba, J. P. Correa Baena, F. Lang, L. Kegelmann, M. Mews, L. Steier, A. Abate, J. Rappich, L. Korte, R. Schlatmann, N. Mohammad K., A. Hagfeldt, M. Grätzel, and B. Rech, “Monolithic perovskite/silicon-heterojunction tandem solar cells processed at low temperature”, *Energy & Environmental Science*, vol. 9, no. 1, pp. 81–88, 2016, ISSN: 1754-5692. DOI: [10.1039/C5EE02965A](https://doi.org/10.1039/C5EE02965A).
- [21] A. G. Milnes and D. Feucht, *Heterojunctions and metal-semiconductor junctions*. New York: Academic Press, 1972, ISBN: 9780323141369.
- [22] S. M. Sze, *Physics of semiconductor devices*, 2nd. New York: John Wiley & Sons, Inc., 1981, ISBN: 0-471-09837-X.
- [23] M. Grundmann, *The Physics of Semiconductors: An Introduction Including Nanophysics and Applications*, 2. ed., ser. Graduate Texts in Physics. Berlin, Heidelberg: Springer-Verlag Berlin Heidelberg, 2010, ISBN: 978-3-642-13883-6.
- [24] J. Shi, X. Xu, D. Li, and Q. Meng, “Interfaces in perovskite solar cells”, *small*, vol. 11, no. 21, pp. 2472–2486, 2015, ISSN: 1613-6829. DOI: [10.1002/smll.201403534](https://doi.org/10.1002/smll.201403534).
- [25] J. H. Davies, *The physics of low-dimensional semiconductors: An introduction*, Repr. Cambridge [u.a.]: Cambridge Univ. Press, 2009, ISBN: 052148491X.
- [26] D. Cavalcoli, *Lecture notes of semiconductors and low dimensional systems*, 2015.
- [27] S. M. Sze and K. K. Ng, *Physics of semiconductor devices*, 3rd ed. Hoboken, N.J.: Wiley-Interscience, 2007, ISBN: 978-0-471-14323-9.
- [28] Q. Chen, N. de Marco, Y. Yang, T.-B. Song, C.-C. Chen, H. Zhao, Z. Hong, and H. Zhou, “Under the spotlight: The organic–inorganic hybrid halide perovskite for optoelectronic applications”, *Nano Today*, vol. 10, no. 3, pp. 355–396, 2015, ISSN: 17480132. DOI: [10.1016/j.nantod.2015.04.009](https://doi.org/10.1016/j.nantod.2015.04.009).
- [29] O. Ergen, S. M. Gilbert, T. Pham, S. J. Turner, M. T. Z. Tan, M. A. Worsley, and A. Zettl, “Graded bandgap perovskite solar cells”, *Nature materials*, 2016, ISSN: 1476-1122. DOI: [10.1038/nmat4795](https://doi.org/10.1038/nmat4795).

-
- [30] G. Niu, W. Li, J. Li, and L. Wang, “Progress of interface engineering in perovskite solar cells”, *Science China Materials*, vol. 59, no. 9, pp. 728–742, 2016, ISSN: 2095-8226. DOI: [10.1007/s40843-016-5094-6](https://doi.org/10.1007/s40843-016-5094-6).
- [31] J. P. Correa Baena, L. Steier, W. Tress, M. Saliba, S. Neutzner, T. Matsui, F. Giordano, T. J. Jacobsson, A. R. Srimath Kandada, S. M. Zakeeruddin, A. Petrozza, A. Abate, M. K. Nazeeruddin, M. Grätzel, and A. Hagfeldt, “Highly efficient planar perovskite solar cells through band alignment engineering”, *Energy & Environmental Science*, vol. 8, no. 10, pp. 2928–2934, 2015, ISSN: 1754-5692. DOI: [10.1039/C5EE02608C](https://doi.org/10.1039/C5EE02608C).
- [32] W. Zhu, C. Bao, F. Li, X. Zhou, J. Yang, T. Yu, and Z. Zou, “An efficient planar-heterojunction solar cell based on wide-bandgap $\text{CH}_3\text{NH}_3\text{PbI}_2$ perovskite film for tandem cell application”, *Chemical communications (Cambridge, England)*, vol. 52, no. 2, pp. 304–307, 2016, ISSN: 1364-548X. DOI: [10.1039/C5CC07673K](https://doi.org/10.1039/C5CC07673K).
- [33] M. R. Filip, G. E. Eperon, H. J. Snaith, and F. Giustino, “Steric engineering of metal-halide perovskites with tunable optical band gaps”, *Nature communications*, vol. 5, p. 5757, 2014. DOI: [10.1038/ncomms6757](https://doi.org/10.1038/ncomms6757).
- [34] S. Collavini, S. F. Volker, and J. L. Delgado, “Understanding the outstanding power conversion efficiency of perovskite-based solar cells”, *Angewandte Chemie (International ed. in English)*, vol. 54, no. 34, pp. 9757–9759, 2015, ISSN: 1433-7851. DOI: [10.1002/anie.201505321](https://doi.org/10.1002/anie.201505321).
- [35] T.-H. Lai, S.-W. Tsang, J. R. Manders, S. Chen, and F. So, “Properties of interlayer for organic photovoltaics”, *Materials Today*, vol. 16, no. 11, pp. 424–432, 2013. DOI: [10.1016/j.mattod.2013.10.001](https://doi.org/10.1016/j.mattod.2013.10.001).
- [36] F. Di Giacomo, V. Zardetto, G. Lucarelli, L. Cinà, A. Di Carlo, M. Creatore, and T. M. Brown, “Mesoporous perovskite solar cells and the role of nanoscale compact layers for remarkable all-round high efficiency under both indoor and outdoor illumination”, *Nano Energy*, vol. 30, pp. 460–469, 2016, ISSN: 22112855. DOI: [10.1016/j.nanoen.2016.10.030](https://doi.org/10.1016/j.nanoen.2016.10.030).
- [37] P. S. C. Schulze, A. J. Bett, K. Winkler, A. Hinsch, S. Lee, S. Mastroianni, L. E. Mundt, M. Mundus, U. Würfel, S. Glunz, M. Hermle, and J. C. Goldschmidt, “Novel low-temperature process for perovskite solar cells with a mesoporous TiO_2 scaffold”, *Acs Applied Materials & Interfaces*, 2017, ISSN: 1944-8244. DOI: [10.1021/acsami.7b05718](https://doi.org/10.1021/acsami.7b05718).
- [38] B. Conings, L. Baeten, T. Jacobs, R. Dera, J. D’Haen, J. Manca, and H.-G. Boyen, “An easy-to-fabricate low-temperature TiO_2 electron collection layer for high efficiency planar heterojunction perovskite solar cells”, *APL Materials*, vol. 2, no. 8, p. 081505, 2014, ISSN: 2166532X. DOI: [10.1063/1.4890245](https://doi.org/10.1063/1.4890245).

- [39] K. Wojciechowski, M. Saliba, T. Leijtens, A. Abate, and H. J. Snaith, “Sub-150 °C processed meso-superstructured perovskite solar cells with enhanced efficiency”, *Energy Environ. Sci.*, vol. 7, no. 3, pp. 1142–1147, 2014, ISSN: 1754-5692. DOI: [10.1039/C3EE43707H](https://doi.org/10.1039/C3EE43707H).
- [40] J. T.-W. Wang, J. M. Ball, E. M. Barea, A. Abate, J. A. Alexander-Webber, J. Huang, M. Saliba, I. Mora-Sero, J. Bisquert, H. J. Snaith, and R. J. Nicholas, “Low-temperature processed electron collection layers of graphene/tio2 nanocomposites in thin film perovskite solar cells”, *Nano letters*, vol. 14, no. 2, pp. 724–730, 2014, ISSN: 1530-6992. DOI: [10.1021/nl403997a](https://doi.org/10.1021/nl403997a).
- [41] J. Werner, C.-H. Weng, A. Walter, L. Fesquet, J. P. Seif, S. de Wolf, B. Niesen, and C. Ballif, “Efficient monolithic perovskite/silicon tandem solar cell with cell area 1 cm²”, *The Journal of Physical Chemistry Letters*, vol. 7, no. 1, pp. 161–166, 2016, ISSN: 1948-7185. DOI: [10.1021/acs.jpcllett.5b02686](https://doi.org/10.1021/acs.jpcllett.5b02686).
- [42] F. Fu, T. Feurer, T. Jager, E. Avancini, B. Bissig, S. Yoon, S. Buecheler, and A. N. Tiwari, “Low-temperature-processed efficient semi-transparent planar perovskite solar cells for bifacial and tandem applications”, *Nature communications*, vol. 6, p. 8932, 2015. DOI: [10.1038/ncomms9932](https://doi.org/10.1038/ncomms9932).
- [43] K. A. Bush, A. F. Palmstrom, Z. J. Yu, M. Boccard, R. Cheacharoen, J. P. Mailoa, D. P. McMeekin, R. L. Z. Hoyer, C. D. Bailie, T. Leijtens, I. M. Peters, M. C. Minichetti, N. Rolston, R. Prasanna, S. Sofia, D. Harwood, W. Ma, F. Moghadam, H. J. Snaith, T. Buonassisi, Z. C. Holman, S. F. Bent, and M. D. McGehee, “23.6%-efficient monolithic perovskite/silicon tandem solar cells with improved stability”, *Nature Energy*, vol. 2, p. 17009, 2017. DOI: [10.1038/nenergy.2017.9](https://doi.org/10.1038/nenergy.2017.9).
- [44] T. T. Chen and D. M. Hawang, “Grating fabrication by interference of laser beams”, *Chinese Journal of Physics*, vol. 15, no. 1, 1977, ISSN: 0577-9073.
- [45] L.-M. Chen, Z. Xu, Z. Hong, and Y. Yang, “Interface investigation and engineering – achieving high performance polymer photovoltaic devices”, *Journal of Materials Chemistry*, vol. 20, no. 13, p. 2575, 2010, ISSN: 0959-9428. DOI: [10.1039/b925382c](https://doi.org/10.1039/b925382c).
- [46] P. Würfel and U. Würfel, *Physics of Solar Cells: From Basic Principles to Advanced Concepts*, 3. Auflage, ser. MyiLibrary. Weinheim: WILEY-VCH, 2016, ISBN: 978-3-527-41311-9.
- [47] N. Serpone, “Is the band gap of pristine TiO₂ narrowed by anion- and cation-doping of titanium dioxide in second-generation photocatalysts?”, *The Journal of Physical Chemistry B*, vol. 110, no. 48, pp. 24 287–24 293, 2006. DOI: [10.1021/jp065659r](https://doi.org/10.1021/jp065659r). [Online]. Available: <https://doi.org/10.1021/jp065659r>.

- [48] J. Kim, G. Kim, Y. Choi, J. Lee, S. Heum Park, and K. Lee, “Light-soaking issue in polymer solar cells: Photoinduced energy level alignment at the sol-gel processed metal oxide and indium tin oxide interface”, *Journal of applied physics*, vol. 111, no. 11, p. 114511, 2012. DOI: [10.1063/1.4728173](https://doi.org/10.1063/1.4728173).
- [49] F. Zhang, Y. Zheng, Y. Cao, C. Chen, Y. Zhan, X. Lin, Q. Zheng, K. Wei, and J. Zhu, “Ordered mesoporous ag–TiO₂–KIT-6 heterostructure: Synthesis, characterization and photocatalysis”, *Journal of Materials Chemistry*, vol. 19, no. 18, p. 2771, 2009. DOI: [10.1039/b818495j](https://doi.org/10.1039/b818495j). [Online]. Available: <https://doi.org/10.1039/b818495j>.
- [50] Y. Park, V. Choong, Y. Gao, B. R. Hsieh, and C. W. Tang, “Work function of indium tin oxide transparent conductor measured by photoelectron spectroscopy”, *Applied Physics Letters*, vol. 68, no. 19, pp. 2699–2701, 1996, ISSN: 0003-6951. DOI: [10.1063/1.116313](https://doi.org/10.1063/1.116313).
- [51] O. A. Abdulrazzaq, V. Saini, S. Bourdo, E. Dervishi, and A. S. Biris, “Organic solar cells: A review of materials, limitations, and possibilities for improvement”, *Particulate Science and Technology*, vol. 31, no. 5, pp. 427–442, 2013. DOI: [10.1080/02726351.2013.769470](https://doi.org/10.1080/02726351.2013.769470). [Online]. Available: <https://doi.org/10.1080/02726351.2013.769470>.
- [52] V. Shrotriya, G. Li, Y. Yao, C.-W. Chu, and Y. Yang, “Transition metal oxides as the buffer layer for polymer photovoltaic cells”, *Applied Physics Letters*, vol. 88, no. 7, p. 073508, 2006. DOI: [10.1063/1.2174093](https://doi.org/10.1063/1.2174093). [Online]. Available: <https://doi.org/10.1063/1.2174093>.
- [53] F.-C. Chen, J.-L. Wu, S. S. Yang, K.-H. Hsieh, and W.-C. Chen, “Cesium carbonate as a functional interlayer for polymer photovoltaic devices”, *Journal of Applied Physics*, vol. 103, no. 10, p. 103721, 2008. DOI: [10.1063/1.2937202](https://doi.org/10.1063/1.2937202). [Online]. Available: <https://doi.org/10.1063/1.2937202>.
- [54] W. Dai, X. Wang, P. Liu, Y. Xu, G. Li, and X. Fu, “Effects of electron transfer between tio₂ films and conducting substrates on the photocatalytic oxidation of organic pollutants”, *The journal of physical chemistry. B*, vol. 110, no. 27, pp. 13470–13476, 2006, ISSN: 1520-6106. DOI: [10.1021/jp061483h](https://doi.org/10.1021/jp061483h).
- [55] T. Kääriäinen, D. Cameron, and M.-L. Kääriäinen, *Atomic layer deposition: Operation and practical applications*, New ed. Hoboken, N.J. and Chichester: Wiley and John Wiley [distributor], 2012, ISBN: 978-1-118-06277-7.
- [56] R. W. Johnson, A. Hultqvist, and S. F. Bent, “A brief review of atomic layer deposition: From fundamentals to applications”, *Materials Today*, vol. 17, no. 5, pp. 236–246, 2014. DOI: [10.1016/j.mattod.2014.04.026](https://doi.org/10.1016/j.mattod.2014.04.026).

- [57] H. B. Profijt, S. E. Potts, van de Sanden, M. C. M., and Kessels, W. M. M., “Plasma-assisted atomic layer deposition: Basics, opportunities, and challenges”, *Journal of Vacuum Science & Technology A*, vol. 29, p. 050 801, 2011, ISSN: 0734-2101. DOI: [10.1116/1.3609974](https://doi.org/10.1116/1.3609974).
- [58] A. Rahtu and M. Ritala, “Reaction mechanism studies on titanium isopropoxide–water atomic layer deposition process”, *Chemical Vapor Deposition*, vol. 8, no. 1, p. 21, 2002, ISSN: 09481907. DOI: [10.1002/1521-3862\(20020116\)8:1<textless>21::AID-CVDE21<textgreater>3.0.CO;2-0](https://doi.org/10.1002/1521-3862(20020116)8:1<textless>21::AID-CVDE21<textgreater>3.0.CO;2-0).
- [59] Q. Xie, J. Musschoot, D. Deduytsche, R. L. van Meirhaeghe, C. Detavernier, S. van den Berghe, Y.-L. Jiang, G.-P. Ru, B.-Z. Li, and X.-P. Qu, “Growth kinetics and crystallization behavior of tio₂ films prepared by plasma enhanced atomic layer deposition”, *Journal of The Electrochemical Society*, vol. 155, no. 9, H688, 2008, ISSN: 0013-4651. DOI: [10.1149/1.2955724](https://doi.org/10.1149/1.2955724).
- [60] C. Hofmann, “Enhancing upconversion performance with a bragg structure”, Master Thesis, Albert-Ludwigs-Universität Freiburg im Breisgau, Freiburg, 2014.
- [61] J. Gutmann, “Photonic luminescent solar concentrators - how photonic crystals affect the emission and guiding of light”, Dissertation, Freiburg, Albert-Ludwigs Universität Freiburg im Breisgau, Freiburg, 2014.
- [62] H. Fujiwara, *Spectroscopic Ellipsometry: Principles and Applications*. Wiley, 2007, ISBN: 9780470016084. [Online]. Available: <https://books.google.de/books?id=qFFdNQEACAAJ>.
- [63] T. Siefke, S. Kroker, K. Pfeiffer, O. Puffky, K. Dietrich, D. Franta, I. Ohlídal, A. Szeghalmi, E.-B. Kley, and A. Tünnermann, “Materials pushing the application limits of wire grid polarizers further into the deep ultraviolet spectral range”, *Advanced Optical Materials*, vol. 4, no. 11, pp. 1780–1786, 2016, ISSN: 2195-1071. DOI: [10.1002/adom.201600250](https://doi.org/10.1002/adom.201600250).
- [64] M. A. Green, “Self-consistent optical parameters of intrinsic silicon at 300 k including temperature coefficients”, *Solar Energy Materials & Solar Cells*, vol. 92, no. 11, pp. 1305–1310, 2008.
- [65] N. W. Ashcroft and N. D. Mermin, *Solid state physics*, Repr. South Melbourne [u.a.]: Brooks/Cole Thomson Learning, 2012, ISBN: 978-0030839931.
- [66] W. H. Bragg and W. L. Bragg, “The reflection of x-rays by crystals”, *Proceedings of the Royal Society A: Mathematical, Physical and Engineering Sciences*, vol. 88, no. 605, pp. 428–438, 1913, ISSN: 1364-5021. DOI: [10.1098/rspa.1913.0040](https://doi.org/10.1098/rspa.1913.0040).
- [67] B. E. Warren, “X-ray diffraction methods”, *Journal of applied physics*, vol. 12, no. 5, pp. 375–384, 1941. DOI: [10.1063/1.1712915](https://doi.org/10.1063/1.1712915).

- [68] Marisa Selinger, “Lock-in thermography and thermal modelling of interdigitated back-contact silicon solar cells”, Master’s thesis, Albert-Ludwigs-Universität, Freiburg im Breisgau, 2014.
- [69] O. Breitenstein, W. Warta, and M. Langenkamp, *Lock-in Thermography*. Berlin, Heidelberg: Springer Berlin Heidelberg, 2010, vol. 10, ISBN: 978-3-642-02416-0. DOI: [10.1007/978-3-642-02417-7](https://doi.org/10.1007/978-3-642-02417-7).
- [70] J. Bachmann, C. Buerhop-Lutz, C. Deibel, I. Riedel, H. Hoppe, C. J. Brabec, and V. Dyakonov, “Organic solar cells characterized by dark lock-in thermography”, *Solar Energy Materials and Solar Cells*, vol. 94, no. 4, pp. 642–647, 2010, ISSN: 09270248. DOI: [10.1016/j.solmat.2009.11.006](https://doi.org/10.1016/j.solmat.2009.11.006).
- [71] T. Fellmeth, F. Clement, and D. Biro, “Analytical modeling of industrial-related silicon solar cells”, *IEEE Journal of Photovoltaics*, vol. 4, no. 1, pp. 504–513, 2014. DOI: [10.1109/jphotov.2013.2281105](https://doi.org/10.1109/jphotov.2013.2281105). [Online]. Available: <https://doi.org/10.1109/jphotov.2013.2281105>.
- [72] M. Yang, Z. Pei-Jian, L. Zi-Yu, L. Zhao-Liang, P. Xin-Yu, L. Xue-Jin, Z. Hong-Wu, and C. Dong-Min, “Enhanced resistance switching stability of transparent ito/tio₂/ito sandwiches”, *Chinese Physics B*, vol. 19, no. 3, p. 037304, 2010, ISSN: 1674-1056. DOI: [10.1088/1674-1056/19/3/037304](https://doi.org/10.1088/1674-1056/19/3/037304).
- [73] Y. Lin, *Resistive switching in TiO₂ thin films*, ser. Schriften des Forschungszentrums Jülich : [...], Reihe Information. Jülich: Forschungszentrum, Zentralbibliothek, 2010, vol. Vol. 17, ISBN: 978-3-89336-707-8.
- [74] C. Nauenheim, *Integration of resistive switching devices in crossbar structures*, ser. Schriften des Forschungszentrums Jülich : Reihe Information. Jülich: Forschungszentrum, Zentralbibliothek, 2010, vol. 10, ISBN: 978-3-89336-636-1.
- [75] A. Yildiz, S. Lisesivdin, M. Kasap, and D. Mardare, “Electrical properties of TiO₂ thin films”, *Journal of Non-Crystalline Solids*, vol. 354, no. 45-46, pp. 4944–4947, 2008. DOI: [10.1016/j.jnoncrysol.2008.07.009](https://doi.org/10.1016/j.jnoncrysol.2008.07.009). [Online]. Available: <https://doi.org/10.1016/j.jnoncrysol.2008.07.009>.
- [76] B. J. Choi, D. S. Jeong, S. K. Kim, C. Rohde, S. Choi, J. H. Oh, H. J. Kim, C. S. Hwang, K. Szot, R. Waser, B. Reichenberg, and S. Tiedke, “Resistive switching mechanism of TiO₂ thin films grown by atomic-layer deposition”, *Journal of Applied Physics*, vol. 98, no. 3, p. 033715, 2005. DOI: [10.1063/1.2001146](https://doi.org/10.1063/1.2001146). [Online]. Available: <https://doi.org/10.1063/1.2001146>.
- [77] H. Tang, K. Prasad, R. Sanjinès, P. E. Schmid, and F. Lévy, “Electrical and optical properties of TiO₂anatase thin films”, *Journal of Applied Physics*, vol. 75, no. 4, pp. 2042–2047, 1994. DOI: [10.1063/1.356306](https://doi.org/10.1063/1.356306). [Online]. Available: <https://doi.org/10.1063/1.356306>.

- [78] I. Senain, N. Nayan, and H. Saim, “Structural and electrical properties of tio2 thin film derived from sol-gel method using titanium (iv) butoxide”, *International Journal of Integrated Engineering*, vol. 3, no. 4, pp. 1–35, 2010.
- [79] M. S. P. Sarah, M. Z. Musa, M. N. Asiah, and M. Rusop, “Electrical conductivity characteristics of TiO2 thin film”, in *2010 International Conference on Electronic Devices, Systems and Applications*, IEEE, 2010. DOI: [10.1109/icedsa.2010.5503040](https://doi.org/10.1109/icedsa.2010.5503040). [Online]. Available: <https://doi.org/10.1109/icedsa.2010.5503040>.
- [80] K. Thamaphat, P. Limsuwan, and B. Ngotawornchai, “Phase characterization of tio2 powder by xrd and tem”, *Kasetsart J. (Nat. Sci.)*, vol. 42, no. 5, pp. 357–361, 2008.
- [81] J. Werner, L. Barraud, A. Walter, M. Bräuninger, F. Sahli, D. Sacchetto, N. Tétreault, B. Paviet-Salomon, S.-J. Moon, C. Allebé, M. Despeisse, S. Nicolay, S. de Wolf, B. Niesen, and C. Ballif, “Efficient near-infrared-transparent perovskite solar cells enabling direct comparison of 4-terminal and monolithic perovskite/silicon tandem cells”, *ACS Energy Letters*, vol. 1, no. 2, pp. 474–480, 2016, ISSN: 2380-8195. DOI: [10.1021/acsenergylett.6b00254](https://doi.org/10.1021/acsenergylett.6b00254).
- [82] J.-P. Correa-Baena, M. Anaya, G. Lozano, W. Tress, K. Domanski, M. Saliba, T. Matsui, T. J. Jacobsson, M. E. Calvo, A. Abate, M. Gratzel, H. Miguez, and A. Hagfeldt, “Unbroken perovskite: Interplay of morphology, electro-optical properties, and ionic movement”, *Advanced Materials*, vol. 28, no. 25, pp. 5031–5037, 2016, ISSN: 0935-9648. DOI: [10.1002/adma.201600624](https://doi.org/10.1002/adma.201600624).
- [83] F. Hao, C. C. Stoumpos, D. H. Cao, Chang, Robert P. H., and M. G. Kanatzidis, “Lead-free solid-state organic-inorganic halide perovskite solar cells”, *Nature Photonics*, vol. 8, no. 6, pp. 489–494, 2014, ISSN: 1749-4885. DOI: [10.1038/nphoton.2014.82](https://doi.org/10.1038/nphoton.2014.82).
- [84] J. H. Kim, P.-W. Liang, S. T. Williams, N. Cho, C.-C. Chueh, M. S. Glaz, D. S. Ginger, and A. K.-Y. Jen, “High-performance and environmentally stable planar heterojunction perovskite solar cells based on a solution-processed copper-doped nickel oxide hole-transporting layer”, *Advanced materials (Deerfield Beach, Fla.)*, vol. 27, no. 4, pp. 695–701, 2015, ISSN: 1521-4095. DOI: [10.1002/adma.201404189](https://doi.org/10.1002/adma.201404189).
- [85] J.-W. Lee, D.-H. Kim, H.-S. Kim, S.-W. Seo, S. M. Cho, and N.-G. Park, “Formamidinium and cesium hybridization for photo- and moisture-stable perovskite solar cell”, *Advanced Energy Materials*, vol. 5, no. 20, p. 1501310, 2015, ISSN: 1614-6840. DOI: [10.1002/aenm.201501310](https://doi.org/10.1002/aenm.201501310).
- [86] J. Liu, Y. Wu, C. Qin, X. Yang, T. Yasuda, A. Islam, K. Zhang, W. Peng, W. Chen, and L. Han, “A dopant-free hole-transporting material for efficient and stable perovskite solar cells”, *Energy & Environmental Science*, vol. 7, no. 9, p. 2963, 2014, ISSN: 1754-5692. DOI: [10.1039/C4EE01589D](https://doi.org/10.1039/C4EE01589D).

- [87] N. K. Elumalai and A. Uddin, “Hysteresis in organic-inorganic hybrid perovskite solar cells”, *Solar Energy Materials & Solar Cells*, vol. 157, pp. 476–509, 2016. DOI: [10.1016/j.solmat.2016.06.025](https://doi.org/10.1016/j.solmat.2016.06.025).
- [88] F. Giordano, A. Abate, J. P. Correa Baena, M. Saliba, T. Matsui, S. H. Im, S. M. Zakeeruddin, M. K. Nazeeruddin, A. Hagfeldt, and M. Graetzel, “Enhanced electronic properties in mesoporous tio2 via lithium doping for high-efficiency perovskite solar cells”, *Nature communications*, vol. 7, p. 10379, 2016. DOI: [10.1038/ncomms10379](https://doi.org/10.1038/ncomms10379).
- [89] L. Kegelmann, C. M. Wolff, C. Awino, F. Lang, E. L. Unger, L. Korte, T. Dittrich, D. Neher, B. Rech, and S. Albrecht, “It takes two to tango—double-layer selective contacts in perovskite solar cells for improved device performance and reduced hysteresis”, *ACS Applied Materials & Interfaces*, vol. 9, no. 20, pp. 17245–17255, 2017. DOI: [10.1021/acsami.7b00900](https://doi.org/10.1021/acsami.7b00900). [Online]. Available: <https://doi.org/10.1021/acsami.7b00900>.